Local effective volume changes in fused silica induced by femtoscecond laser irradiation

Citation for published version (APA):
Champion, A. (2015). *Local effective volume changes in fused silica induced by femtoscecond laser irradiation.* [Phd Thesis 1 (Research TU/e / Graduation TU/e), Mechanical Engineering]. Technische Universiteit Eindhoven.

Document status and date:
Published: 26/01/2015

Document Version:
Publisher's PDF, also known as Version of Record (includes final page, issue and volume numbers)

Please check the document version of this publication:

• A submitted manuscript is the version of the article upon submission and before peer-review. There can be important differences between the submitted version and the official published version of record. People interested in the research are advised to contact the author for the final version of the publication, or visit the DOI to the publisher's website.
• The final author version and the galley proof are versions of the publication after peer review.
• The final published version features the final layout of the paper including the volume, issue and page numbers.

[Link to publication](#)

Local effective volume changes in fused silica induced by femtosecond laser irradiation

PROEFSCHRIFT

ter verkrijging van de graad van doctor aan
de Technische Universiteit Eindhoven, op
gezag van de rector magnificus, prof.dr.ir. C.J.
van Duijn, voor een commissie aangewezen
door het college voor Promoties in het
openbaar te verdedigen op maandag 26
januari 2015 om 16.00 uur

door

Audrey Champion

geboren te Dijon, France

Dit proefschrift is goedgekeurd door de promotoren en de samenstelling van de promotiecommissie is als volgt:

Voorzitter:	prof.dr. L.P.H. de Goey
1^e promotor:	prof.dr.ir. J.M.J. den Toonder
Copromotor:	dr. Y.J. Bellouard
Leden:	prof.dr. P.G. Kazansky (University of Southampton)
	prof.dr. G. de With
	prof.dr. D. Iannuzzi (Vrije Universiteit Amsterdam)
	dr.ir. R.H.J. Peerlings
Adviseur:	dr. J. Solis (Instituto de Óptica, CSIC)

Local effective volume changes in fused silica induced by femtosecond laser irradiation

Audrey Champion

Contents

Summary

Local effective volume changes in fused silica induced by femtosecond laser irradiation

The context of this work is a novel micro-manufacturing process that uses non-ablative femtosecond laser pulses combined with chemical etching for fabricating three-dimensional micro-parts and integrated optical components in fused silica (the glassy phase of silicon dioxide - SiO_2). This process is finding an increasing number of use, not only in integrated optics but also in applications as diverse as optomechanics and optofluidics.

So far, the selection of appropriate laser parameters has been essentially done by trial-and-error approaches which does not allow for an efficient and optimal use of the micro-manufacturing process. This limitation originates mainly from a lack of understanding of the relation between laser exposure parameters and local etching rate enhancement mechanisms. Noticeably, the role of the stress in the etching process has been so far widely ignored.

This thesis aims at fulfilling this gap of knowledge by specifically investigating localized density variations consecutives to the laser exposure. These density variations are de facto essential for linking stress and laser-induced nanostructures as well as for gaining more insights about the reported anisotropy of laser modified zones.

To achieve this goal, we have developed two characterization methods respectively based on cantilever deflections and stress-induced birefringence measurements to effectively quantify volume changes in laser-affected zones, the level of stress surrounding laser-affected zones as well as the role of laser-light polarization.

In addition, to identify the specific role of the stress in the etching process and this, - independently of possible photo-chemical effects induced by the laser exposure, we have developed a femtosecond laser-machined micro-mechanism that allows us to precisely load a pristine volume of silica to high, homogeneous and well defined stress levels. By observing the local etching rate enhancement in the stressed zones, the relation between stress and etching rate can be effectively quantified independently of laser parameters.

Specifically, using these three experimental techniques, we have been able: first, to observe a transition between localized densification and volume expansion according to laser exposure parameters, second, to identify the effective contribution of stress in the etching enhancement mechanism, and finally, to demonstrate and quantify the importance of polarization on stress distribution.

From a theoretical point of view, the outcome of these experiments allow us to propose a mechanism to explain the origin of the etching rate enhancement, and to show why and how this localized enhancement effects may depend preferentially on certain laser exposure parameters.

From a technology development perspective, the results of this thesis provide a tool for optimizing the micromachining of fused silica with respect to the optimal dosage of laser energy deposited in the material to achieve a given micro-machined patterns aspect ratio and conformity. It also provides guidelines for preventing the occurrence of cracks in integrated optical devices.

Chapter I. Introduction: Context and thesis objectives

The context of this work is a novel micro-manufacturing technique that uses low-energy femtosecond laser pulses combined with chemical etching for processing fused silica (the glassy phase of silicon dioxide - SiO_2). Specifically, this thesis investigates the structural changes observed after the laser irradiation and their consequences for the process efficiency. In this chapter, we will first introduce femto- and pico-second lasers and the current scientific understanding of the interaction of these lasers with dielectric materials. In the second part, the structure and properties of silica glass will be summarized, restricting ourselves to what is essential for discussing our experimental results and phenomenological interpretations. A laser process combining ultrashort laser pulses exposure and etching steps is then introduced, together with a brief summary of the relevant laser parameters that control it. Finally, the last part of this chapter positions our work with respect to the questions that remain unanswered concerning this novel three-dimensional micro-manufacturing process and introduces the outline of the thesis.

1.   A short introduction to femtosecond and picosecond lasers

Femtosecond lasers were developed around 1980. They provide pulses from a few femtoseconds (1 fs=10^{-15} s) to several hundreds of femtoseconds. So far, these pulses have been mainly used in research to investigate ultra-short time phenomena but they are recently being gradually applied in manufacturing. Ultrashort pulses confine the laser energy in a short time duration and if focused, within a small volume. Consequently high peak power is reached locally, in the order of 100 GW/mm^2 for the process we will be dealing with in this work. This high peak power density opens the possibility to ionize any transparent material, thanks to non-linear absorption effects that will be described later on. For this reason, femtosecond lasers are also potentially interesting for machining transparent materials, although they are not yet widely used in industry due to the recent discovery of this process.

In this thesis, we focus our attention to the field of laser micro-machining. There, the femtosecond laser beam is focused at the surface or within the volume of a solid. By scanning the beam over the specimen or moving the specimen under the beam, the solids can be machined. Two types of interactions are found: the material can be either ablated or simply modified.

The ablation process consists of removing the material within the focused area. Ultrashort pulses, (i.e. lasting less than a few tens of picoseconds), are well adapted to engrave or to cut structures with dimensions of micrometers in solids, due to the achievable high precision. The low or inexistent thermal diffusion allows reaching smoother features than for ablation that takes place with longer pulses (> 100 ps). As an illustration, Fig. 1 [1] shows the difference, in terms of micromachining quality, between nanosecond and femtosecond lasers. With a few nanoseconds (ns), micromachining is less precise.

Ablation with ultrashort pulses is performed with so-called femtosecond and picosecond lasers that are based on different optical designs. Femtosecond lasers provide lower average power than picosecond lasers and are usually more delicate to use as they are more prone to instabilities. Although the machining quality is potentially higher, the ablation process efficiency is diminished compared to picosecond laser machining. For industrial applications, to date, this still presents an important disadvantage, in addition to the higher cost of femtosecond lasers. That is the main reason why, until now, femtosecond lasers are used only for special applications where high precision is crucial and balanced with the economical disadvantages. Note that with the progress made in laser technology, the average power of femtosecond lasers is rapidly increasing in industrial-grade lasers.

With nanosecond laser   **With femtosecond laser**
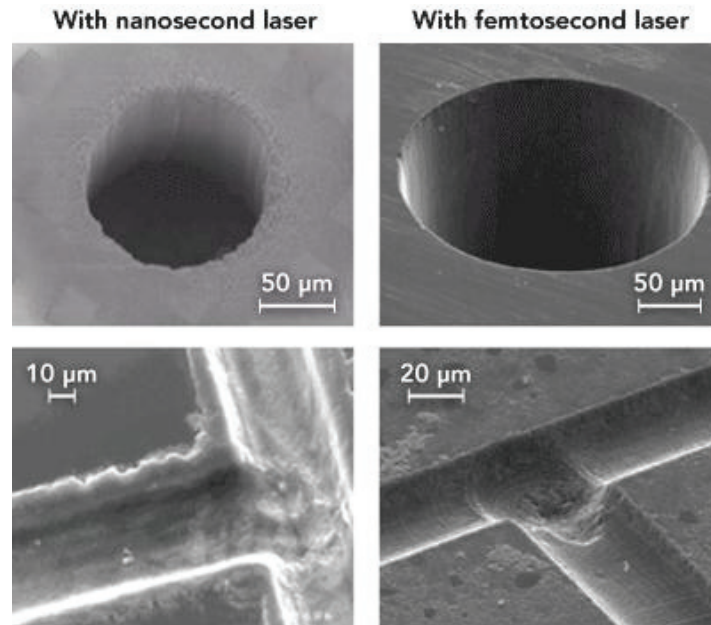
Fig. 1. Comparison between features ablated in glass with nanosecond and femtosecond laser pulses, respectively [1].
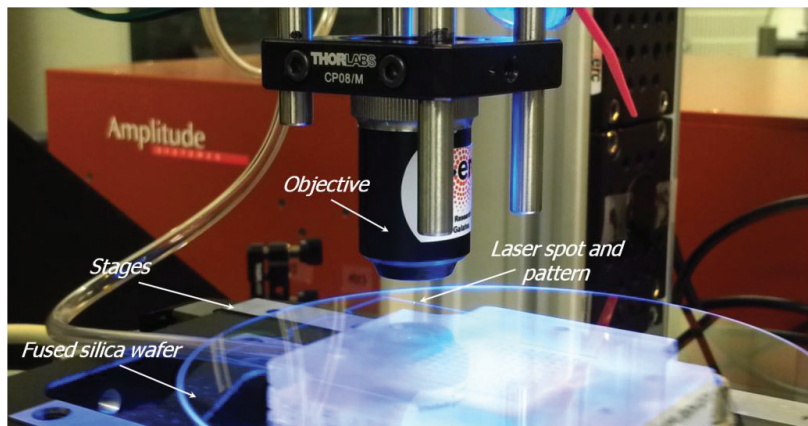
Fig. 2. A typical set-up for micromachining in a fused silica wafer. The sample is moved in the plane under an objective mounted on a vertical moving stage so that the laser spot can describe three-dimensional trajectories within the material. At energies below the ablation threshold, the material is not removed but structural modifications can be induced. In some dielectrics, one can observe optical property changes such as refractive index increases as well as modifications of the material response to specific chemicals. The latter can materialize itself in a locally increased etching rate.

In Fig. 2, a picture of one of our laser platforms (femtosecond laser providing 150 fs pulse duration) during micro-machining illustrates the writing process principle. A fused silica specimen is mounted on stages moving in a plane perpendicular to a microscope objective. This microscope objective is itself attached to a vertical stage allowing focusing the laser beam within the material.

In the following sections, the fundamental mechanisms at work in the interaction between the laser and the solid will be explained.

2.   Physics of femtosecond laser-matter interaction with dielectrics

a.   *Mechanisms occurring during ultrafast interaction*

Ultrashort pulse durations are within a few fs to a few ps. Such pulses can be emitted from lasers with various wavelengths, from the UV (Excimers) to the short-IR (for instance, Ti:Sapphire, 800 nm, Yb, 1030 nm) and mid-IR (1.5 µm) ranges. When tightly focused in a dielectric material, the absorption of photons becomes nonlinear: above a material-dependent laser peak power threshold, the material, normally transparent at the laser wavelength, becomes absorbent. Let us consider the case of fused silica as an illustration. The pseudo band gap of fused silica is 9 eV and therefore, for a single photon to ionize the material, it must be sufficiently energetic. This condition is satisfied for photons of short wavelengths, i.e. in the UV range and below 200 nm. With the exception of excimer lasers that are difficult to operate, sources of short wavelength photons are difficult to find. On the other hand, when the density of incoming photons at a given time is sufficiently high – like in the case of tightly focused ultrashort pulses, non-linear absorption processes like the so-called 'multi-photon' can take place. To initiate this non-linear absorption process in silica, a threshold intensity of I of about 10^{13} W/cm^2 must be reached.

More generally, the photon number (m) needed for initiating non-linear absorption in a given material of band gap E_g is determined by the smallest integer m that satisfies the following relation:

$$mh\nu > E_g \qquad\qquad (1.1)$$

with h, the Planck constant and ν the laser frequency equal to c/λ (c is the light speed and λ is the wavelength of the laser). As an illustration of the equation above, in the case of Ytterbium laser sources – the lasers we operated in the experiments reported in this thesis – eight photons are required.

According to the pulse duration different laser-matter interaction mechanisms occur. Fig. 3 illustrates the typical time scale for physical processes taking place during and after a laser impact in a material. For a pulse duration in the order of the picosecond or less, thermal effects such as thermal diffusion do not take place during the interaction (In Fig. 3 the yellow area represents the interaction time interval for femtosecond lasers which are used in this thesis).

Classical interactions, such as thermal diffusion and re-solidification are typically found in laser-matter interaction with longer pulses, from a few 100 ps. The ultrashort pulse interaction is therefore unique in many aspects.
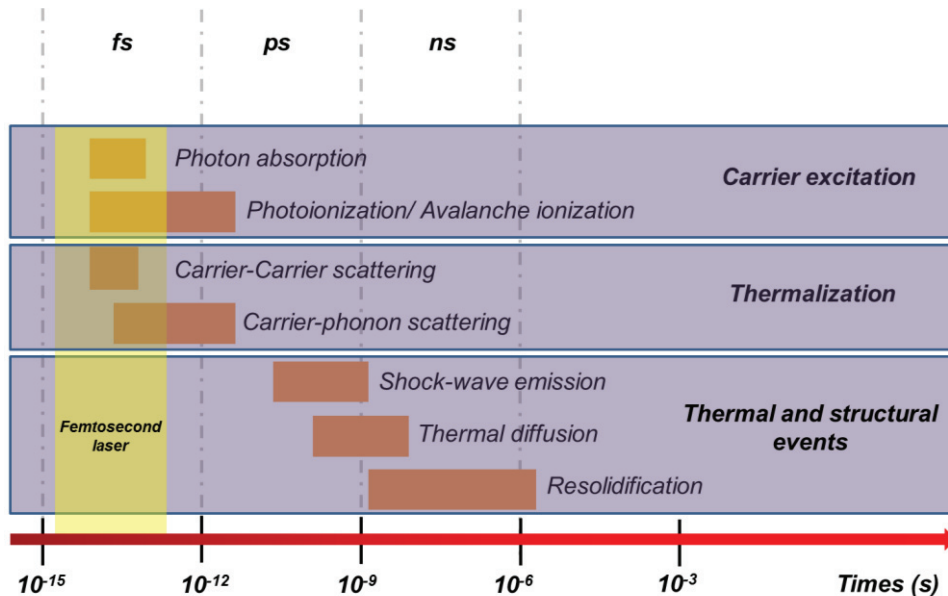
Fig. 3. Time scale of physical interaction mechanisms, adapted from [2] involved when a laser interacts with a solid. The area in yellow represents the typical duration of femtosecond laser pulses. With such ultrashort pulse duration, only non-linear mechanisms such as multiphoton absorption, photoionization and avalanche ionization take place while the pulse is impacting the material. At longer time scales, thermal and structural events appear like shock-waves, thermal diffusion, and resolidification.

For ultrashort pulses, although the laser-matter interaction is not fully understood, the interaction mechanisms are commonly described as follows: the first step consists of carrier excitation, being the transfer of electromagnetic energy (laser light) to electronic excitation (plasma formation). In a second step, electron-lattice interaction leads to the recombination of the particle in the plasma to the matrix of the dielectric and therefore, to permanent modifications in the material.

Two classes of nonlinear carrier excitation mechanism play a role in the absorption, namely photoionization and avalanche ionization.

b. *Production of seed electrons: photoionization and tunneling effects*

During nonlinear photoionization, a direct excitation of electrons occurs. Depending on the laser intensity and frequency, three regimes of photoionization are observed

[3]: multiphoton, tunneling ionization and an intermediate regime where both multiphoton and tunneling ionization take place.

In the tunneling regime, the Coulomb potential well that describes the bound state of electrons is suppressed due to the extremely strong electromagnetic laser field, so that the electrons can tunnel through the lower barrier and become free. The tunneling effect is dominant in a strong laser field and at low pulsation ω of the laser light.

In contrast, multiphoton absorption occurs for higher pulsation and weaker laser field. The transition between the two regimes is defined through the following criterion, derived by Keldysh [3]

$$\gamma = \frac{\omega}{e}\left[\frac{mcn\varepsilon_0 E_{\mathrm{g}}}{I}\right]^{\frac{1}{2}} \tag{1.2}$$

In this expression, $\omega = 2\pi c/\lambda$ is the laser pulsation, I the laser intensity at the focus point, m is the reduced mass of an electron, e is the charge of an electron, n is the refractive index of the material, ε_0 is the permittivity of free space, c is the speed of light and E_{g} is the pseudo band gap of the material.

According to this criterion, when γ is smaller than 1.5, the tunneling regime prevails. Above this value, multiphoton absorption is observed. Around the value of 1.5, an intermediate regime is observed which consists of a combination of both, tunneling and multiphoton absorption. The three regimes are illustrated in Fig. 4.

In the cases considered in this thesis, since the pseudo band gap of fused silica is about 9 eV and since our lasers provide pulses at 1030 nm with typically less than 300 nJ per pulse, γ is approximately equal to two. From Keldys criterion, multi-photon absorption is therefore the dominant phenomenon to seed electrons from the valence band to the conduction band.

Three ionization regimes :

Tunneling γ<1.5   *Intermediate γ=1.5*   *Multi-photon
ionization γ>1.5*
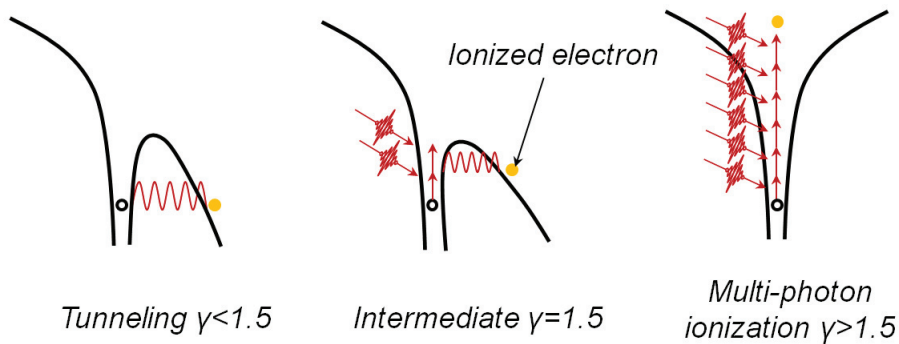
Fig. 4. Three types of non-linear absorption mechanisms with their corresponding Keldysh parameters. This figure is adapted from [4]. Left: Tunneling effect ($\gamma < 1.5$) occurring under strong laser field. The electric field of the laser decreases the potential energy of electrons so that they are ionized without photon absorption and through tunneling effect. Right: Photoionization ($\gamma > 1.5$) where the potential energy of the electron remains high enough to prevent tunneling. In this case, several photons need to be absorbed to ionize electrons. Center: the intermediate regime when $\gamma \approx 1.5$ and when both photoionization and tunneling effects occur.

c.   *Further electron production: Avalanche ionization*

The seed-electrons from the multiphoton processes (so-called free carriers), present in the conduction bands gradually gain energy by absorbing incoming photons from the laser light. We call this process free carrier absorption. The electrons may gain sufficiently high energy through free absorption to collide with other electrons still present in the valence band. In this case, free electrons relax to lower energy (but still in the conduction band) by transferring a part of their energy to an electron in the valence band to satisfy energy conservation. The principle is illustrated in Fig. 5. As long as the laser field is present, electrons from the conduction band can further collide with the ones in the valence band causing the overall electron density in the plasma to increase.

After these excitation processes, various energy dissipation mechanisms such as carrier-carrier and carrier-phonon scattering occur. Carrier-carrier scattering is the recombination of the electrons in the glass matrix. Defects such as color center or non-bridging oxygen hole centers are created and create dangling bonds in the material matrix. As a result the electron energy levels in these defects are not equal to the electron energy level in the bulk. Free electrons can recombine with these atoms in transferring their energy.
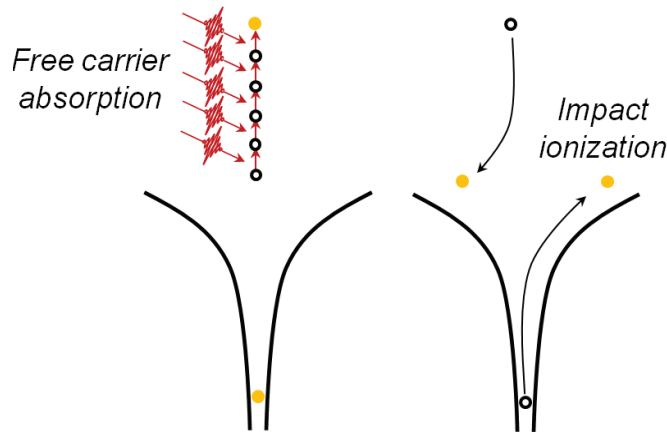
Fig. 5.   The two steps leading to avalanche ionization adapted from [4]. Left: Free carrier absorption; when electrons are in the conduction band (after absorbing several photons through multiphoton processes), they gain further energy by absorbing incoming photons from the laser. Right: Impact ionization; excited electrons in the conduction band having gained sufficient energy from free absorption process eventually collide with electrons in the valence band that in turn, become free. The process may continue until no more photons from the laser source are seeded to the plasma. This is called avalanche ionization since this is a cascading event.

Carrier-phonon scattering refers to free electrons which transfer part of their energy to the glass matrix via phonon. A phonon is a collective excitation of electrons in the lattice representing vibration on the atomic scale within the lattice. Electrons can transfer their energy (momentum) to these pseudo particles and relax themselves. Both mechanisms lead to different electronic distribution around atoms and change the properties of the material by introducing permanent defects in the lattice.

In addition to the phenomena described above, two undesired effects in the focused volume may appear at higher laser power, namely self-focusing and heat accumulation.

d. *Self-focusing*

When a material is exposed to an intense laser pulse, non-linear optical processes occur so that the refractive index increases with the intensity of the light. The Gaussian distribution of the laser intensity, gives rise to an intensity concentration in the center of the beam as it travels in the medium. As the refractive index in this area increases with the laser intensity, the material locally behaves like a focusing lens. The intensity of the self-focused region keeps increasing as the light propagates in the material until defocusing or material damage occurs. Two main

types of self-focusing may occur, namely Kerr-effect focusing and plasma self-focusing.

Kerr-effect induced self-focusing is an increase of the refractive index when the material is exposed to an intense electromagnetic radiation. The refractive index is expressed with equation (1.3):

$$n = n_0 + n_2 I \quad with \quad \begin{cases} I = \dfrac{1}{2}\varepsilon_0 c n_0 E^2 \\ n_0 = \sqrt{1 + \chi^{(1)}} \\ n_2 = \dfrac{3\chi^{(3)}}{4\varepsilon_0 c n_0^2} \end{cases} \tag{1.3}$$

where c is the speed of the light and ε_0 is the electric permittivity. n_0 is the refractive index of the medium and can be expressed with the linear electric susceptibility of the medium $\chi^{(1)}$, n_2 is the non-linear refractive index due to the Kerr-effect expressed with the nonlinear electric susceptibility $\chi^{(3)}$ of the medium and I is the intensity in the focused volume expressed according to the electric field of the light E. n_2 is positive in fused silica so that the refractive index becomes larger when the intensity is higher. This leads to a focusing density profile in the center of the beam and, as a result, the beam collapses on itself. To avoid this phenomenon, the power in the beam needs to be smaller than the critical power expressed by equation (1.4) [5].

$$P_{cr} = \alpha \frac{\lambda^2}{4\pi n_0 n_2} \tag{1.4}$$

where, λ is the wavelength of the laser and α is a constant calculated from the initial distribution of the beam (1.8962 for a Gaussian distribution). In our case, the critical power for self-focusing is never reached. Indeed the refractive index n_0 for fused silica is about 1.453 and $n_2 = 2.4.10^{-20}$ m^2/W. The wavelength of our laser is 1030 nm. The critical power concentrated in the focus area ($\approx 2.5 \times 10^{-12}$ m^2) is then 1.8×10^{18} W/m^2. Since the maximum energy per pulse used in our experiment is 300 nJ, the pulse duration of the laser is always above 150 fs (the shortest pulse duration used in this work), it leads to a peak power of at most, 8×10^{17} W/m^2.

Plasma self-focusing occurs due to ponderomotive and relativistic effects. The ponderomotive effect is a non-linear force present in the inhomogeneous electromagnetic field of a plasma that concentrates the electrons in the area where the intensity is highest. Therefore, the density of the plasma increases and a focusing effect occurs.

Relativistic focusing is created by the increase of the mass of the electrons accelerated in the field. Being the dominant phenomenon, the reference threshold

for plasma self-focusing is the relativistic critical power expressed with equation (1.5) [6,7]:

$$P_{cr} = \alpha \frac{m_e^2 c^5 \omega^2}{e^2 \omega_p^2} = 17 \left(\frac{\omega}{\omega_p} \right)^2 GW \qquad (1.5)$$

In this equation m_e is the electron mass, c the speed of light, ω the radiation angular frequency, e the electron charge and ω_p the plasma frequency.

In under-dense plasma, we have $\omega_p < \omega$. Therefore P_{cr} is always higher than 17 GW. If we concentrate this power in our focused area, it is equal to 6.8×10^{21} W/m². As seen before, with our laser, we are never in these conditions. To summarize, in what follows, we assume that self-focusing is never taking place for the experimental conditions we are considering.

e. *Cumulative regime*

Material absorbs the laser light and only after a certain relaxation time, part of the energy converted into heat will diffuse out of the focal area. If the time between incoming pulses is shorter than the heat-diffusion time, the temperature keeps on increasing. Fig. 6 shows the principle.
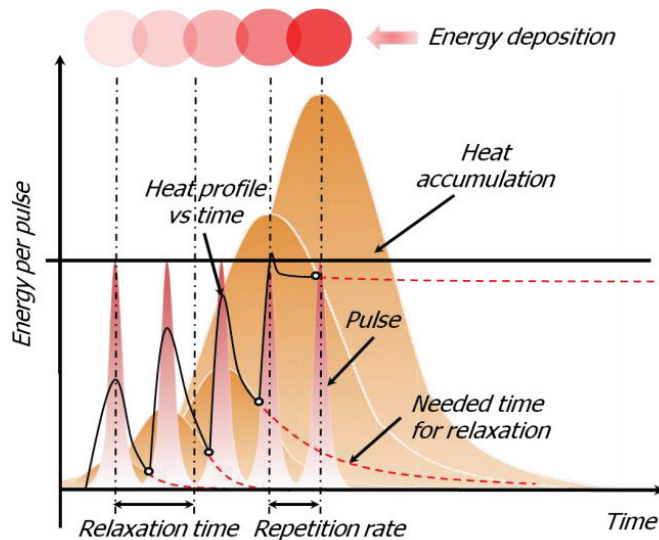
Fig. 6.   Energy accumulation when the repetition rate of the laser is higher than the inverse of the relaxation time of the material. The relaxation time is the time needed to reach a thermal equilibrium. In the cumulative regime, heat keeps on accumulating (in brown) when pulses (in pink) interact with the solid.

The typical relaxation time for glass is about 1 µs. In the experiments presented in this thesis, the maximum repetition rate used is 800 kHz. Therefore, the smallest time separating two pulses is 1.25 µs. That means that we are always in the non-cumulative regime.

The interaction mechanisms described above lead to different types of structural modifications of the solid, according to the laser parameters and the type of materials. In the next section, we will focus on fused silica.

3.   **Femtosecond lasers applied to fused silica**

a.   *Structure and properties of fused silica*

Fused silica (SiO_2) is an amorphous material consisting of SiO_4 tetrahedra linked to each other to form rings of statistically varying sizes (see Fig. 7). Different types of fused silica exist [8]. Natural silica glasses have a high level of impurity (content of metal oxide) whereas synthetic silica glasses include almost no metal oxide impurities. In this thesis, we use synthetic silica glass. The main advantage of using pure fused silica is to avoid cluster formation of metals present in the glass after laser exposure.

Fused silica is a dielectric material and therefore cannot conduct electrical current since it does not have electrical charges that can move. Notwithstanding, fused silica does have electrical characteristics. For instance, the atoms can form electrostatic dipoles that can interact with electric fields. Fused silica densifies when its fictive temperature increases [8,9]. When fused silica is under stress, the bond angle deforms which modifies the electron distribution of Si-O-Si bonds so that the chemical reactivity is increased [10].

Fused silica is chemically stable, i.e. it does not react with most chemicals with the exception of water, hydrofluoric acid and potassium hydroxide. It has a high glass transition temperature (T_g) and therefore, fused silica is suitable for laboratory equipment and tools that function at high temperatures. Its transparency in the visible wavelength range – in particular in the UV, makes this material suitable for high-end optical components and optical fibers. Finally, fused silica is used as insulator in electronics applications. Indeed, all dielectric materials behave as insulator because they can hardly conduct a current. However, unlike "pure insulators" (e.g. wood), they can be polarized under an electric field. In other words, they do not conduct electrical current but can interact with an electric field.

Mechanical properties	Young's modulus	Poisson's ratio	Shear modulus
	72.1 GPa	0.179	30.6 GPa
	Modulus of Rupture	Density	
	52.4 MPa	(at 25°C): 2.201 g/cm^3	
Optical properties	**Refractive index**	**Transmission range**	
	1.4589 (589 nm)	0.18-2.2 µm	
Thermal properties	**Thermal conductivity**	**Heat capacity**	**Thermal diffusivity**
	1.38 W/m.K	0.770 J/g K	0.0075 cm^2/s
	Coefficient of the thermal expansion		
	0.57 ppm/K at 0-200°C		
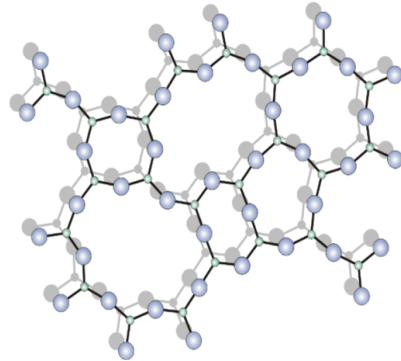
Fig. 7. Left: Typical mechanical, optical and thermal properties of fused silica (Valley design corp. website.). Right: Matrix of amorphous fused silica consisting of SiO$_4$ tetrahedra linked to each other to form rings of statistically varying sizes.

b. *Silica structurally modified by femtosecond laser processing*

When exposing fused silica to femtosecond laser beams, three types of structural modifications, (commonly labeled "Type I, II and III") have been reported as a function of energy per pulse and pulse duration (see Fig. 8 [11]).

The first regime (type I), where homogeneous modifications are observed in the laser-affected zone (LAZ), leads to an increase of refractive index $\Delta n \approx 5.10^{-3}$ [12] and an increase of etching rate [13]. This positive index variation, observed in regime I, makes waveguide fabrication possible. Experimental evidence suggest that localized densifications are responsible for type I structures [14,15]. For instance, Raman observation [15,16], suggests that possible densification phenomena observed after exposure may be due to a decrease of the Si-O-Si bond angles, although Raman spectroscopy does not provide quantitative information. Other techniques like nano-indentation have shown evidence of a densification regime [14]. If densification indeed occurs, we expect volume changes in the laser-affected zone and as a result, stress should be present in and around the structures. Indeed, shear stress is observed in the homogeneous regime [17]. Stress is observed in waveguides as well [18].
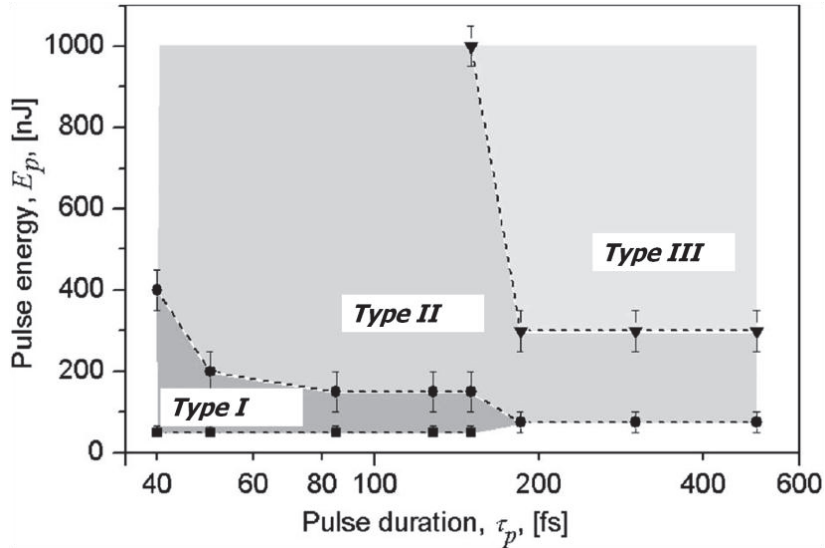
Fig. 8. Graph showing the three achievable regimes of structural modification of fused silica when exposed to a femstosecond laser, as a function of laser parameters (adapted from [11]). At low pulse duration (below 200 fs) and low pulse energy (below 200 to 400 nJ), homogeneous modifications are induced during exposure (Type I). At higher pulse energy and higher pulse duration, nanogratings form in the transparent material (Type II). If the pulse duration is higher than 200 fs and the energy per pulse is larger than about 300 nJ, micro-explosions inducing shock-waves and voids form, leading to an ablation regime (Type III).

The intermediate regime (type II), where self-organized patterns consisting of "nanogratings" are found [19,20,21], presents interesting optical properties such as form-birefringence [22] giving the possibility to create novel photonics devices such as polarization converters [23]. Although their structures seem to be radically different than for type I modifications, interestingly, nanogratings also lead to a local increase of etching rate that is strongly dependent on the laser light polarization [24]. We will further discuss some of the proposed mechanisms for the nanogratings formation below in more detail.

In Fig. 9, scanning thermal microscopy (SThM) images in both regimes (I and II) are shown. We clearly see the homogeneity in the first regime and the nanogratings formation in the second regime.
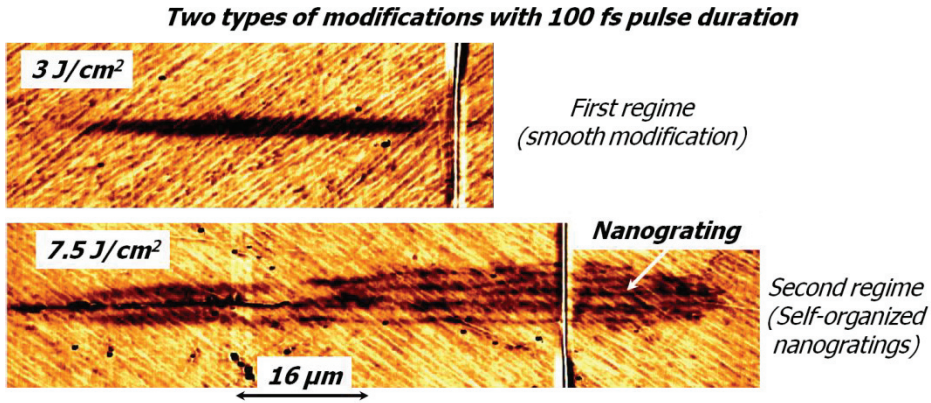
Fig. 9. Scanning Thermal Microscopy (SThM) images of a transverse cut showing morphologies of laser-affected zones [15]. The top image shows homogeneous structures, whereas in the bottom image, laser-affected zone nanoplanes are clearly visible.

Finally, in the Type III regime, self-organized structures (nanogratings) collapse and become disorganized. At higher energy and for higher energy confinement, (at high numerical aperture), micro-explosion [25] and ablation process starts.

From a material science point-of-view, the nature of structural changes remains elusive. Shimotsuma et al. [19] indicated that nanogratings contain oxygen-depleted zones. To explain the enhanced etching mechanism in the nanogratings regime, a model based on oriented nanocracks was also proposed [26]. In this model, nanogratings are interpreted as a set of oriented cracks, oriented perpendicularly to the polarization of the laser. However, recent SEM observations [27], showing the presence of a porous structure inside the lower-index zone of the nanogratings, contradict this interpretation. In addition, Rajesh et al. have shown [28] that, in the nanogratings regime, the etching rate first reaches a maximum for a given amount of deposited energy and then decays for a higher amount of deposited energy. This observation cannot be explained with a model where an accelerated etching rate is driven by the presence of oriented cracks. Indeed, according to this nanocracks model, the etching rate should keep on increasing (or at least not diminish) with the increasing amount of deposited energy (i.e. the number of nanocracks should increase with the energy deposited). Therefore, another type of physical mechanism is responsible for the accelerated etching rate.

c. *Nanogratings formation*

The formation of nanogratings is not fully understood. Two main models are proposed as tentative explanations of nanogratings formation.

The Kazansky-model [19] is based on the occurrence of interference of the laser field with the electric field of the bulk electron plasma wave. Multi-photon ionization (see Fig. 4) produces a high density of free electrons when the laser interacts with glass. A plasma forms and absorbs the laser light by one photon absorption through the mechanism of inverse bremsstrahlung heating. This absorption mechanism is dominant when the laser interacts with a dense plasma. The bulk electron plasma wave is excited by the absorption of the laser light in the electron plasma. These bulk density plasma waves are longitudinal and their electric field is parallel to the propagation direction. Only the electron wave propagating in the plane of the incident laser light polarization can interfere with the incident light. Inhomogeneity induced by electrons moving in the plane of light polarization create initial coupling. A periodic structure produced by the interference of incident light and bulk electrons increases the coupling. As a result, the plasma electron wave creates periodic modulation of the electron plasma concentration and therefore of the structural changes in the material. If the plasma wave has a positive gain coefficient (i.e. the medium transfers part of its energy to the emitted electromagnetic radiation), the periodic structure oriented perpendicularly to the light propagation, exponentially grows and becomes frozen into the material. The electron waves responsible for the nanogratings formation are generated only in the direction defined by the conservation of longitudinal component of momentum (Cherenkov mechanism of non-linear wave generation [29]). The nanogratings period is defined by this momentum condition as follows:

$$K_{gr} = \frac{2\pi}{\Lambda} = \sqrt{k_{pl}^2 - k_{ph}^2} \qquad (1.6)$$

with k_{pl} the wave vector of the plasma and k_{ph} the vector wave of the incident light. The dispersion relation for the electron plasma wave from the Langmuir wave is given by:

$$\omega_{pl}^2 = \omega_p^2 + \frac{3}{2} v_e^2 k_{pl}^2$$

$$\omega_p = \sqrt{\frac{N_e e^2}{\varepsilon_0 m_e}} \qquad v_e = \sqrt{\frac{k_B T_e}{m_e}} \qquad (1.7)$$

where ω_p is the plasma frequency, N_e the electron density, m_e the electron mass and e the electron charge, v_e the thermal speed of the electrons, T_e the electron temperature and K_B Boltzmann's constant. Energy conservation gives $\omega_p = \omega$ and the period of nanogratings is expressed by:

$$\Lambda = \frac{2\pi}{\frac{1}{T_e}\left(\frac{m_e \omega^2}{3 k_B} - \frac{N_e e^2}{3 \varepsilon_0 k_B} - k_{ph}^2\right)} \qquad (1.8)$$

With this model, the nanogratings period increases with the electron concentration and with the temperature.

The other model that attempts to explain nanogratings formation is the nanoplasmonic model [20,21] proposed by P. Corkum's team in Ottawa, which is based on the enhancement of the electric field due to defects, like color centers, inherently present in the material. Inhomogeneity of the plasma is created through localized ionization. The ionization needs to be localized in nanometer dimensions to create nanoplasmas in the material. When nonlinear ionization occurs in the solid, all photons are absorbed in the focused area because of the high atomic density. The number of atoms is well higher than the photons of the laser light in the focused area. Indeed, the atomic density in fused silica is 10^{20} atoms/mm^2 and there are 10^{15} atoms in our focused area (since the area is about equal to 10^{-6} mm^2). With a laser wavelength of λ = 1030 nm, the energy per photon is $E = hc/\lambda$ = 1.9299x10^{-19} J with h the Planck constant. If we consider 300 nJ per pulse, 10^{13} photons in the focused area are provided. Assuming that 8 photons for ionization are needed, we have about 10^{12} photons available per unit area. Therefore, there are about 1000 times more atoms than photons. Nonlinear ionization has the effect of slightly cutting the pulse in space and time so that the intensity becomes flat at the top of the profile in the focused area. This intensity profile allows the possibility of the initiation of the nanoplasmas everywhere in the focal volume and allows limiting the focused power below the critical power for self-focusing.

In our case, since we work with a dielectric material, multiphoton ionization can start locally in a single laser pulse because of the thermal noise or at local defects like color centers or impurities. Electrons or holes are trapped in the point defects and their ionization potential is reduced so that they can be ionized easier than other electrons in the atoms. These seed electrons can trigger the avalanche ionization. These defects make the plasma randomly nonuniform. Local changes in the material after the first pulse influence the interaction of the subsequent pulses. This is called the memory effect and has been demonstrated in transparent materials. Each pulse decreases the ionization threshold. It reaches saturation over thousands of shots and the material is no longer able to change. This threshold decrease could be due to bond breaking, structural and chemical reorganization. This localized ionization at the defects sites in the material leads to the production of nanoplasmas.

As they grow, they can become quasi-metallic and influence the laser light propagation. The laser light couples with plasmons (collective oscillation of the electrons in nanoplasmas) to form surface Plasmon-polariton. In this case, the nanoplasmas self-organize in the field of the laser light. In this model, the nanograting period is independent on energy per pulse and scanning speed. This is in contradiction with the Kazansky model.

These models are incomplete, for instance the Kazansky model, where interferences are present from the first pulse, cannot explain why nanogratings are

not present for single pulse. In Corkum's model it is not clear how self-organization takes place since defects around which nanoplasma form are randomly distributed.

   d.   *Combined laser exposure with etching*

Femtosecond lasers exposure with non-ablative pulses can be used to machine transparent materials like fused silica. Owing from the non-linearity of the process (as described earlier), it is a three-dimensional direct writing method in glass, and an alternative to lithography. The machining principle is depicted in Fig. 10. The glass sample is placed on moving stages that can describe three-dimensional trajectories. In a first step, the laser light is focused anywhere in the transparent material, inducing various modifications like the ones described earlier. In a second step, an etchant is used (in our case hydrofluoric acid - HF or potassium hydroxide - KOH), to dissolve the laser-exposed zones accessible to the acid, and the written-patterns are actually dissolved.
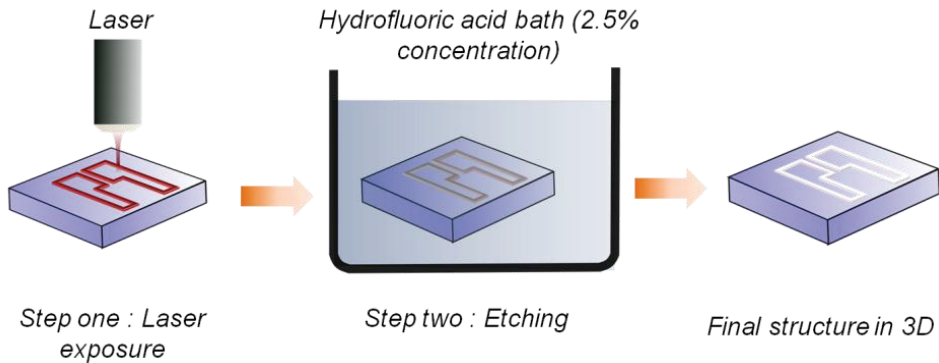
Fig. 10. Illustration of the femtosecond laser micro-fabrication process. Left: the laser beam is focused in fused silica and 3D structures are written in the sample placed on moving stages. Middle: Etching step consisting of dissolving the laser-exposed patterns. Right: Final structure after etching (white lines represent the removed material).

   The volume-to–be-etched needs to be accessible to the etchant so that the chemical can dissolve it. If the structure is written in the bulk of the material, additional lines from the surface or edges to the structure have to be written so that the etchant can reach the structures. Hydrofluoric acid is a natural etchant for amorphous SiO_2. The dissolution mechanism of SiO_2 in HF is described by the following simplified chemical reaction [30]:

$$SiO_2 + 6HF \rightarrow H_2SiF_6 + 2H_2O \qquad (1.9)$$
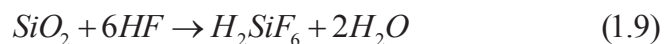
   The typical etching-rate of pristine silica is in the order of one micrometer per hour (for an HF concentration of 2.5 %). The laser exposure locally accelerates

the etching rate by a factor varying from 2 to 95, depending on the laser parameters and in particular, the energy deposition that we will define later on. To estimate the final shape of a given contour and for an accurate dimensioning, it is therefore important to take into account the effect of the 'natural' etching of SiO_2. Fig. 11 schematically describes this effect for a channel with a rectangular cross-section. Assuming that the etching rate is uniform in all directions in the non-exposed volume, we expect that the size of the channel near the edge (top of the Fig. 11), will be larger than the size of the channel in the bulk (bottom) since the channel near the edges will be etched during a longer time. It is important to modulate the etching rate according to the laser parameters and especially according to the energy deposition to obtain the desired final shape.
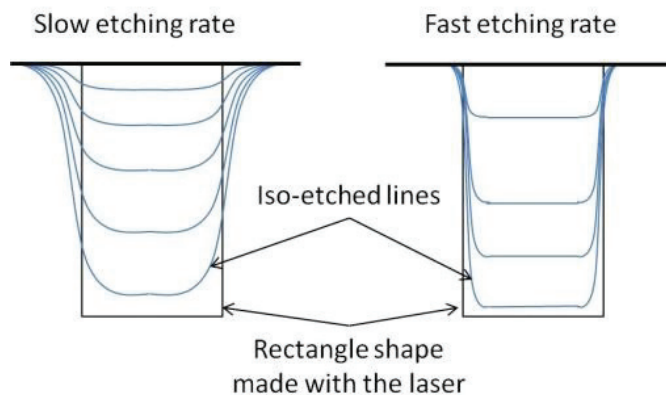
Fig. 11. Illustration of the influence of the etching rate on the final etched shape. The desired pattern is a channel, represented here by a continuous black line. For the sake of discussion, here, we assume that the laser-pattern exactly matches the desired pattern. Left: Evolution of the etching front for a slow etching rate enhancement in the laser exposed pattern. The top of the channel will be larger than the bottom. Right: Case of a fast etching rate enhancement in the laser-affected zone. A higher fidelity between the laser-exposed pattern and the desired one is achieved. Aspect ratios are therefore governed by the etching-rate enhancement factor introduced in the laser-affected zones.

e.   *Laser parameters influencing the processing*

- **Energy per pulse**

Since the interaction is non-linear, the energy per pulse defines the size of the interaction zones in the focused area as seen in Fig. 12. The size of the spot follows a logarithmic trend as the energy per pulse increases. A model to calculate the spot size is explained in chapter II.
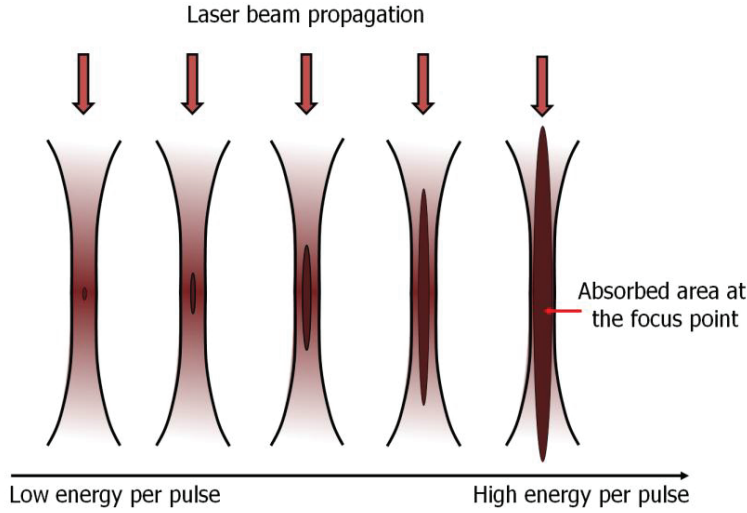
Fig. 12. Evolution of the laser absorbed area according to the energy per pulse.

- *Energy deposition*

The energy deposition (also called net fluence) represents the amount of energy deposited per unit surface by the laser in the solid. Note that this is not the actual absorbed energy, which will always be less than the energy deposited. It is nevertheless convenient to speak about 'energy deposition' when comparing data since the absorbed energy cannot be easily measured dynamically and includes different absorption mechanisms difficult to decouple one from another.

The energy deposited depends on the energy per pulse and on the laser scanning speed (see Fig. 13). To evaluate the energy deposition, we use a formula from [28].

The number of pulses in a surface corresponding to the beam diameter is:

$$M = \frac{W_{\text{laz}} f}{v} \qquad (1.10)$$

where W_{laz} is the laser-affected area, f the repetition rate and v the writing speed. If we assume that the ratio $v/f << W_{\text{laz}}$, in other words, that the spatial pulse–to-pulse distance is much smaller than the spot size, we can neglect the effect of the circular geometry on the energy deposited distribution and assume that it is homogenous across the line width. The energy deposition is approximated by:

$$E_{\text{d}} = \frac{4 E_{\text{p}} f}{\pi W_{\text{laz}} v} \qquad (1.11)$$

where, E_p is the energy per pulse. The size of the affected area W_{laz} depends on the numerical aperture of the focusing objective, on the pulse duration and on the absorption threshold of the material.
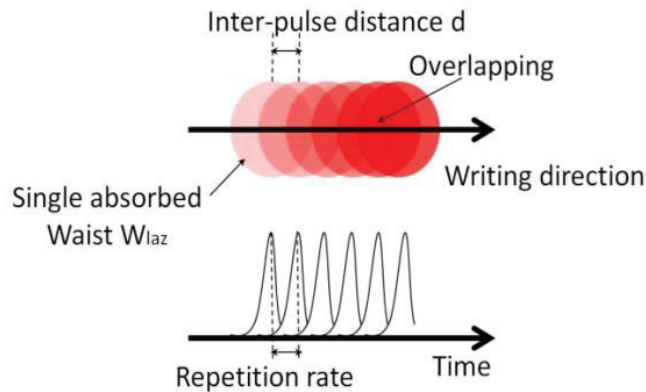
Fig. 13. Schematic illustrating the concept of energy deposition, as influenced by the laser process parameters [28]. Repetition rate – the rate at which pulses are emitted, writing speed and energy per pulse are the main parameters that can be tuned to control the energy deposition. Repetition rate and speed define the distance d between pulses. Energy per pulse defines the size of the laser-affected zone.

This parameter is also important for understanding nanogratings formation since in [31] the width of the nanogratings depends on the scanning speed. In addition, as reported in [32,33], the period of nanogratings is constant when the spatial distance between pulses is up to tens of nanometers. For higher spatial distances between pulses, (for instance at higher writing speed), the nanogratings period increases. Other works show that the etching rate varies in the second regime according to energy deposition [28].

- *Numerical aperture of the objective (NA)*

The numerical aperture of the objective defines the size of the spot, and therefore, it determines the focused peak power. The larger NA is, the higher the peak power will be.

- *Polarization of the laser with respect to the writing direction*

Propagating light can be described by an electromagnetic wave, i.e the solution of Maxwell equations in free space and that can be spatially described by a triad of orthogonal vectors as can be seen in Fig. 14. The k-vector that defines the propagation direction, the electric and the magnetic fields are represented by vectors that are oriented perpendicular to each other. The polarization defines the electrical vector angle with respect to unit vectors attached to a coordinate frame

in a plane perpendicular to the propagation direction of the light. Different types of polarization state exist. For random polarization - as for instance for light emitted from the sun, the electric field is oriented randomly as the light propagates. For rectilinear polarization, the electric field keeps the same angle while propagating. For circular polarization, the electric field turns around the optical axis as the light propagates.
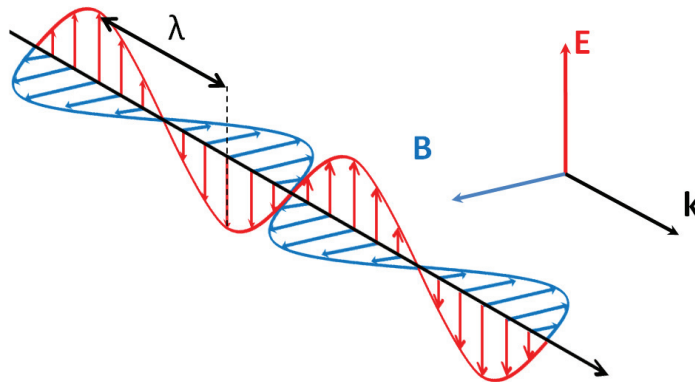
Fig. 14. Electromagnetic wave representation with a triad of orthogonal vector. **E** is the electric field, **B** is the magnetic field and **k** is the vector representing the direction of the propagation. Different polarizations exist according the electric field direction as the wave propagates. For instance in this figure, the electric field keeps the same direction as it propagates, and the polarization is called linear.

The etching rate depends on the laser polarization [24]. Therefore, this parameter is crucial to achieve complex micromachining. In addition, nanogratings are oriented perpendicular to the electric field [19] and therefore, can be oriented according to the writing direction by modifying the beam polarization state.

f. *Application examples*

Waveguides can be fabricated using femtosecond laser fabrication. There, the material is slightly modified by the laser causing a local increase of refractive index. An example is shown in [12]. These waveguides can be applied in integrated optics. In Fig. 15 some examples are shown.
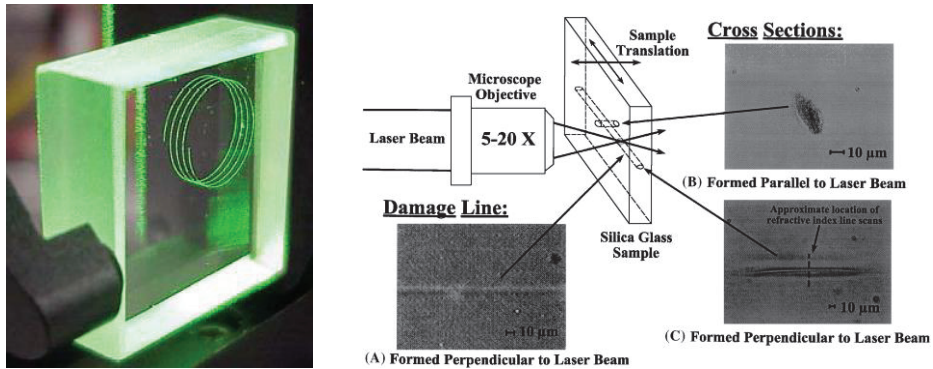
Fig. 15. Left: Helicoidal waveguides made by Translume Inc. Right: waveguides inscribed in fused silica [12].

The fabrication of other optical components such as micro-lenses or wave plates [34] was also demonstrated.

Another example of applications are micro-fluidic channels fabricated using the two-step process combining laser exposure and etching. Microfluidic devices can be used in lab-on chip devices for medical diagnostics [35] or for detection of species in liquids, e.g. algae species in water [36]. In Fig. 16, a SEM image is shown of two channels made using multi-pass laser lines in fused silica, followed by chemical etching [37].
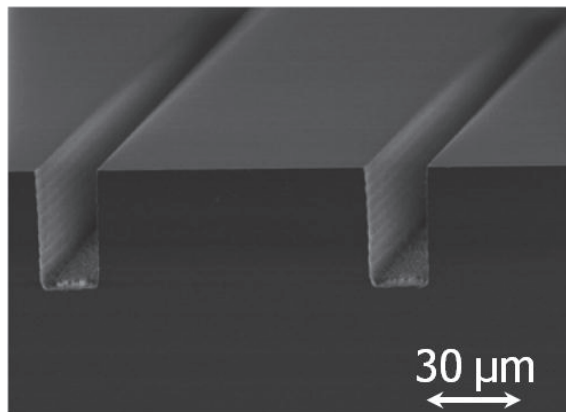
Fig. 16. Scanning electron microscopy (SEM) picture of microfluidic channels in fused silica [37]. Several lines written in a row were used to achieve large channels. The channels are 30 micrometers wide and 60 micrometers deep.

A more complex example in [38] shows the combination between written waveguides and a micro-mechanical system to form an optical sensor in a monolithic substrate (see Fig. 17). This sensor measures displacement along the x

axis. If a force is applied on the sensor tip, a displacement along x axis occurs. The flexures attached to the stationary frame at one side and attached to the mobile part at the other side guide the mobile part. Several waveguides with different refractive indexes (integrated linear encoder) are written in the mobile part and two waveguides facing each other are inscribed in the stationary frame so that when the mobile part is moving along x axis, the cross-section of the embedded waveguides and the cross-section of the waveguides in the frame match. In this case the light is guided and can be detected. Each different waveguide correspond to a position.
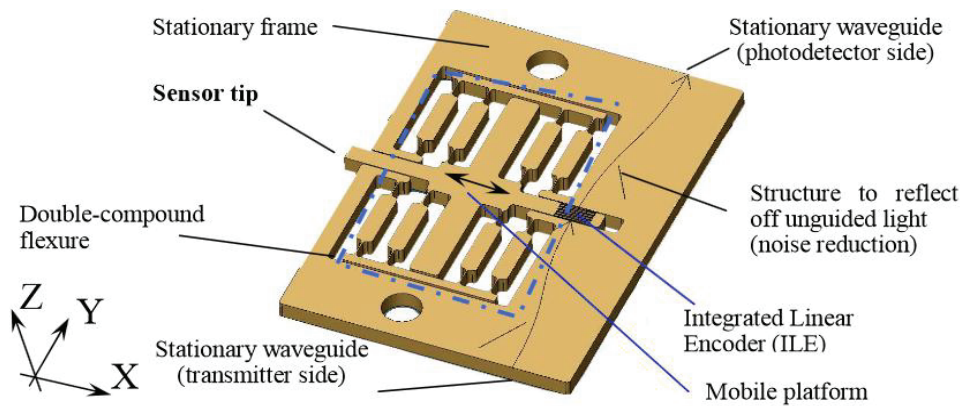
Fig. 17. Computer assisted drawing of the full sensor [38].

By combining the different approaches mentioned above, it is possible to create optofluidics (combining micro-channels and waveguides) or optomechanical (combining optical and mechanical structures) systems, using a monolithic, two-step fabrication approach. This underlines the large potential for applications in the microsystems domain for femtosecond laser machining with non-ablative pulses.

4.   Thesis objectives

When femtosecond laser interacts with fused silica in the non-ablative regime, refractive index variations are observed in either continuously modified zones or in self-organized patterns forming in the laser-affected zones. These index variations can be either positive or negative, but suggest that a volume variation is locally taking place. These volume variations, that are likely to be present, would lead to the generation of stress in and around the laser-affected zones. Evidences of the presence of stress after laser exposure are provided by the observations of cracks that may form in laser-affected zones as can be seen for instance in Fig. 18.
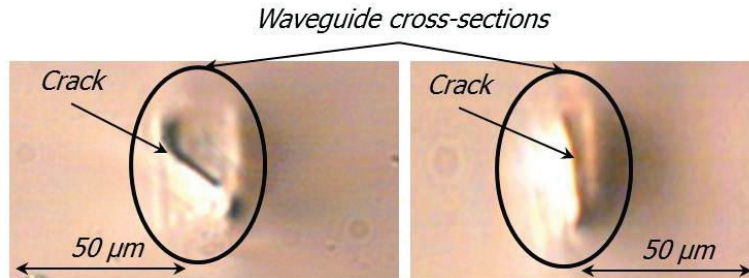
Fig. 18. Optical images of waveguides made by Translume Inc. of the cross-sections of waveguides made of several lines spaced by 0.5 µm (left) and 0.25 µm (right) Cracks are forming due to build up of stress in the patterns.

So far, there is no analysis of the origin and quantification of volume variations resulting from laser-exposure. This information is, however, *essential* for multiple reasons:

1/ It can help us to understand better the nature of structural modifications in laser-affected zones.

2/ It could provide an alternative method to measure relative refractive index increase.

3/ The formation of cracks could be explained and predicted.

4/ Possible relations between etching rate enhancement and stress could be unraveled. While it is known that stress effectively increases etching rate in bulk glass [9] it is unclear if the etching-rate enhancement observed after laser exposure is only a photo-induced effect or simply driven by higher stress concentration or may be, a combination of both effects.

5/ Finally, for improving the process in terms of accuracy of the final fabricated shapes, predictability of the formation of cracks and for optimizing the laser parameters, the accurate knowledge of volume variations – and consequently, of stress generated by laser exposed patterns – is a necessary step.

The main objectives of our thesis are therefore:

> **First, to quantify the amount of volume changes (and consequently, the level of stress introduced during femtosecond laser exposure) and second, to understand the relation between these volume changes with the observed etching-enhancement mechanisms.**

5.   Outline of the thesis

Following this first introductory chapter, the second chapter proposes an experimental method to quantify volume variations around laser-affected zones

according various exposure parameters. The volume variations measurement will provide us indirect measurement of the stress state and amplitude. This experimental technique is based on micro-mechanics and more specifically, cantilever beam deflection.

The third chapter introduces another method to determine the stress around laser-affected zones. This second method is based on stress-induced birefringence measurements. Complementary to the experimental method presented in chapter II, this second approach provides direct and rapid insights on the importance of laser beam polarization on stress distribution.

In the fourth chapter, the influence of the mechanically induced stress in fused silica on the etching rate is investigated under compressive and tensile stress. The objective is to decouple stress from laser-affected zones and therefore to be able to evaluate the stress-contribution to the etching rate enhancement phenomena.

The fifth chapter, written in collaboration with Dr Costantino Corbari in Prof Peter Kazansky's group at the University of Southampton, investigates the influence of pulse duration, comparing picosecond and femtosecond laser micromachining. The objective is to investigate the influence of the pulse duration on the machining quality, in particular in the regime of a few picoseconds where the laser-matter interaction dynamics (excitons dynamics in particular) shows a transition ([39]). The second objective is technological. Picosecond lasers offer cutting-edge advantages over femtosecond laser in terms of cost, simplicity and average power available. However, it is unclear if such lasers are able to provide the same process ability than femtosecond lasers. In this chapter, we propose a critical comparison between the two types of lasers.

In the last chapter, we conclude by summarizing the novel insights into micromachining of fused silica by femtosecond laser fabrication obtained in this thesis, and propose some recommendations for further research.

6.   References

1. L. Lucas and J. Zhang, "Femtosecond laser micromachining: A back-to-basics primer," Appl. Energetics (2012), Industrial laser solution.
2. R. R. Gattass and E. Mazur, "Femtosecond laser micromachining in transparent materials," Nat. Photon **2**, 219–225 (2008).
3. h. L. V. Keldys, 1964 Zh. Eksp. Teor. Fiz. **47** 1945 (Engl. Transl.) Sov. Phys. –JETP **20** 1307 (1965).
4. C. B. Schaffer, A. Brodeur, and E. Mazur, "Laser-induced breakdown and damage in bulk transparent materials induced by tightly focused femtosecond laser pulses," Meas. Sci. Technol. **12**, 1784 (2001).
5. G. Fibich and A. L. Gaeta, "Critical power for self-focusing in bulk media and in hollow waveguides", Opt. Lett. **25**, 335 (2000).
6. G. A. Mourou, et al. "Optics in the relativistic regime", Rev. Mod. Phys. **78**, 309 (2006).

7. G. Sun et al. "Self-focusing of short intense pulses in plasmas", Phys. Fluids **30**, 526 (1987).

8. R. Brückner, "Metastable equilibrium density of hydroxyl-free synthetic vitreous silica," J. Non-Cryst. Solids **5**, 281–285 (1971).

9. A. Agarwal and M. Tomozawa, "Correlation of silica glass properties with the infrared spectra," J. Non-Cryst. Solids **209**, 166–174 (1997).

10. T. A. Michalske and B. C. Bunker, "Slow fracture model based on strained silicate structures,"J. Appl. Phys. **56**, 2686–2693 (1984).

11. C. Hnatovsky, J. R. Taylor, P. P. Rajeev, E. Simova, V. R. Bhardwaj, D. M. Rayner, and P. B. Corkum, "Pulse duration dependence of femtosecond-laser-fabricated nanogratings in fused silica," Appl. Phys. Lett. **87**, 14104-14106 (2005).

12. K. M. Davis, K. Miura, N. Sugimoto, and K. Hirao, "Writing waveguides in glass with a femtosecond laser," Opt. Lett. **21** (21), 1729–1731 (1996).

13. A. Marcinkevičius, S. Juodkazis, M. Watanabe, M. Miwa, S. Matsuo, H. Misawa, and J. Nishii, "Femtosecond laser-assisted three-dimensional microfabrication in silica," Opt. Lett. **26** (5), 277–279 (2001).

14. Y. Bellouard, T. Colomb, C. Depeursinge, M. Dugan, A. A. Said, and P. Bado, "Nanoindentation and birefringence measurements on fused silica specimen exposed to low-energy femtosecond pulses, " Opt. Express **14** (18), 8360–8366 (2006), doi:10.1364/OE.14.008360.

15. Y. Bellouard, E. Barthel, A. A. Said, M. Dugan, and P. Bado, "Scanning thermal microscopy and Raman analysis of bulk fused silica exposed to low-energy femtosecond laser pulses, " Opt. Express **16** (24), 19520–19534 (2008), doi:10.1364/OE.16.019520.

16. J. W. Chan, T. Huser, S. Risbud, and D. M. Krol, "Structural changes in fused silica after exposure to focused femtosecond laser pulses," Opt. Lett. **26**, 1726–1728 (2001).

17. B. Poumellec, M. Lancry, J.-C. Poulin, and S. Ani-Joseph, "Non reciprocal writing and chirality in femtosecond laser irradiated silica," Opt. Express **16**, 18354–18361 (2008).

18. L. A. Fernandes, J. R. Grenier, P. R. Herman, J. S. Aitchison, and P. V. S. Marques, "Stress induced birefringence tuning in femtosecond laser fabricated waveguides in fused silica," Opt. Express **20**, 24103–24114 (2012).

19. Y. Shimotsuma, P. G. Kazansky, J. R. Qiu, and K. Hirao, "Self-organized nanogratings in glass irradiated by ultrashort light pulses," Phys. Rev. Lett. **91** (24), 247405 (2003).

20. V. R. Bhardwaj, E. Simova, P. P. Rajeev, C. Hnatovsky, R. S. Taylor, D. M. Rayner, and P. B. Corkum, "Optically produced arrays of planar nanostructures inside fused silica, " Phys. Rev. Lett. **96** (5), 057404 (2006).

21. P. P. Rajeev, M. Gertsvolf, C. Hnatovsky, E. Simova, R. S. Taylor, P. B. Corkum, D. M. Rayner, and V. R. Bhardwaj, "Transient nanoplasmonics inside dielectrics," J. Phys. B: Atomic, Molecular and Optical Physics **40**, S273–S282 (2007).

22. E. Bricchi, B. G. Klappauf, and P. G. Kazansky, "Form birefringence and negative index change created by femtosecond direct writing in transparent materials," Opt. Lett. **29** (1), 119–121 (2004).

23. M. Beresna, M. Gecevičius, P. G. Kazansky, and T. Gertus, "Radially polarized optical vortex converter created by femtosecond laser nanostructuring of glass," Appl. Phys. Lett. **98**, 201101–201101–3 (2011).

24. C. Hnatovsky, R. S. Taylor, E. Simova, V. R. Bhardwaj, D. M. Rayner, and P. B. Corkum, "Polarization-selective etching in femtosecond laser-assisted microfluidic channel fabrication in fused silica," Opt. Lett. **30** (14), 1867–1869 (2005).

25. E. N. Glezer and E. Mazur, "Ultrafast-laser driven micro-explosions in transparent materials," Appl. Phys. Lett. **71** (7), 882–884 (1997).

26. R. Taylor, C. Hnatovsky, and E. Simova, "Applications of femtosecond laser induced self-organized planar nanocracks inside fused silica glass," Laser Photonics Rev. **2** (1-2), 26–46 (2008).

27. J. Canning, M. Lancry, K. Cook, A. Weickman, F. Brisset, and B. Poumellec, "Anatomy of a femtosecond laser processed silica waveguide [Invited]," Opt. Mater. Express **1**, 998 (2011).

28. S. Rajesh and Y. Bellouard, "Towards fast femtosecond laser micromachining of fused silica: The effect of deposited energy," Opt. Express **18** (20), 21490–21497 (2010), doi:10.1364/OE.18.021490.

29. D. H. Auston, K. P. Cheung, J. A. Valdmanis, and D. A. Kleinman, "Cherenkov Radiation from Femtosecond Optical Pulses in Electro-Optic Media," Phys. Rev. Lett. **53**, 1555–1558 (1984).

30. G. A. C. M. Spierings, "Wet chemical etching of silicate glasses in hydrofluoric acid based solutions," J. Mater. Sci. **28**, 6261–6273 (1993).

31. F. Liang, R. Vallée, and S. L. Chin, "Mechanism of nanograting formation on the surface of fused silica," Opt. Express **20**, 4389–4396 (2012).

32. Q. Sun, F. Liang, R. Vallée, and S. L. Chin, "Nanograting formation on the surface of silica glass by scanning focused femtosecond laser pulses," Opt. Lett. **33**, 2713–2715 (2008).

33. R. Wagner, J. Gottmann, A. Horn, and E. W. Kreutz, "Subwavelength ripple formation induced by tightly focused femtosecond laser radiation," Appl. Surf. Sci. **252**, 8576–8579 (2006).

34. E. Bricchi, J. D. Mills, P. G. Kazansky, B. G. Klappauf, and J. J. Baumberg, "Birefringent Fresnel zone plates in silica fabricated by femtosecond laser machining," Opt Lett **27**, 2200–2202 (2002).

35. P. Yager, T. Edwards, E. Fu, K. Helton, K. Nelson, M. R. Tam and B. H. Weig "Microfluidic diagnostic technologies for global public health," Nature **442**, 412-418 (2006).

36. A. Schaap, T.Rohrlack, and Y. Bellouard "Lab on a chip technologies for algae detection" J. Biophotonics 5, 661–672 (2012).

37. Y. Bellouard, A. Said, M. Dugan, and P. Bado, "Fabrication of high-aspect ratio, micro-fluidic channels and tunnels using femtosecond laser pulses and chemical etching," Opt. Express **12**, 2120–2129 (2004).

38. Y. Bellouard, A. Said, and P. Bado, "Integrating optics and micro-mechanics in a single substrate: a step toward monolithic integration in fused silica," Opt. Express **13**, 6635–6644 (2005).

39. B. C. Stuart, M. D. Feit, S. Herman, A. M. Rubenchik, B. W. Shore, and M. D. Perry, "Nanosecond-to-femtosecond laser-induced breakdown in dielectrics," Phys. Rev. B Condens. Matter **53**(4), 1749–1761 (1996).

Chapter II. Volume variation in fused silica exposed to femtosecond laser irradiation

In this chapter, we propose a method to quantify localized volume variations induced by lasers as a function of laser exposure parameters. This method further allows the quantification of stress levels and provides some indications on the stress-state itself. We use this technique that we complement with scanning electron microscope (SEM) and Raman observations to demonstrate a stress-state inversion that may occur in certain laser exposure conditions.

Part of this chapter has been reported in: A. Champion and Y. Bellouard, "Direct volume variation measurements in fused silica specimens exposed to femtosecond laser," Opt. Mater. Express **2**, 789-798 (2012).

1. Introduction

In this chapter, we introduce a new experimental technique for investigating and quantifying localized volume variations resulting from femtosecond laser exposure in the non-ablative regime. The main challenge is to find a method that can provide an accurate measurement of volume variation occurring in material (volumes of a few micrometers cubed) and that can be easily implemented, so that multiple laser-exposure parameters can be applied. Note that the methodology proposed here could be used in a variety of situations involving structural changes introduced by laser exposure.

2.   Working principle

Our method is based on micro-cantilever deflection. The working principle is outlined in Fig. 19. A transparent cantilever is exposed locally to a laser beam, but only close to its anchoring point and only on the upper part (but just below the surface, so that the surface remains continuous and unaffected). In the cantilever portion exposed to the laser beam, the modified zone and the unaffected layers form a bimorph composite structure (see Fig. 19).
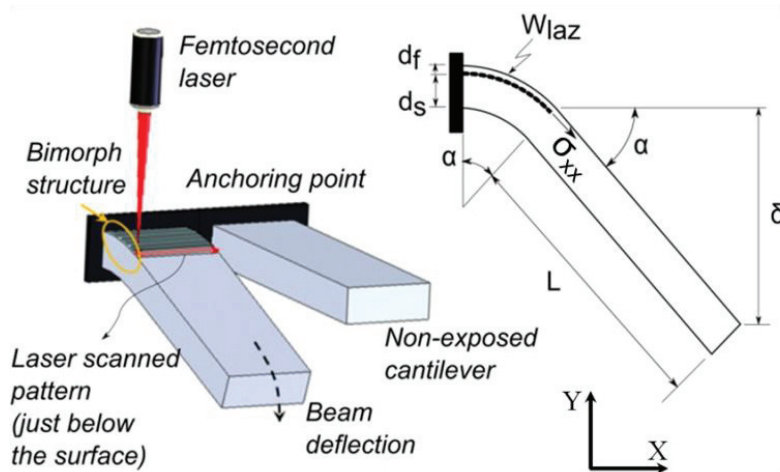
Fig. 19. Left: Working principle for measuring volume changes using cantilever deflection. The laser exposure takes place only near the anchoring point of the cantilever and only in its upper-half thickness and forms a bimorph composite structure that induces local bending of the cantilever. The deflection, measured at the tip of the cantilever, is effectively amplified by the length of the cantilever. Right: Schematic of the cantilever cross-section and definition of the geometrical parameters used in the analysis.

If a volume expansion or reduction occurs in the laser-affected zone, the bimorph element will bend down or up, respectively. In this thesis, after laser exposure and when the material is in equilibrium, stress is defined positive when a volume expansion took place and the material at the boundary between laser affected and pristine zones is locally under compression. Likewise, stress is defined negative when densification occurred and conversely, the material at the boundary between laser affected and pristine zones is locally under tension.

The bimorph-zone forms a hinge. Any resulting displacement is amplified by the cantilever arm. Note that because of the geometrical amplification, the volume that needs to be laser-irradiated can in principle be minimized to as little as a single scanned line. The deflection amplification provides a simple and yet efficient method for increasing the measurement range and achieving a high resolution.

Based on the measured deflection, the localized volume expansion in the laser-affected zone is extracted. To do so, we use two mechanical models. The first one considers the laser-affected zone as a continuously and homogeneously modified layer on a bulk-unmodified substrate. Effectively, this is similar to a bimorph structure made of two different materials. We use the Stoney equation [1] to calculate the stress in the laser-affected portion of the cantilever and then, to estimate the volume variation. Here, we assume that the boundaries between the two layers are to a first approximation well-defined. Stoney's equation enables us to calculate the stress in the upper layer as a function of the radius of curvature of the bimorph and is expressed by

$$\sigma_{xx} = \frac{E_s d_s^2}{6R\left(1-v^2\right)d_f} \tag{2.1}$$

Where E_s is the young modulus of the 'substrate' (here the bulk unmodified fused silica), d_s the substrate thickness, d_f the thickness of the laser-affected layer, v the Poisson ratio of the unmodified zone and R the radius of curvature (of the bimorph zone). We assume that R is measured along the neutral axis of the cantilever beam. R is calculated from the deflection measurement (see Fig. 19, right for the geometrical parameters). Note that the angle α is small therefore we can make approximation.

$$\left.\begin{array}{c} R = \dfrac{s}{\alpha} = \dfrac{w_{laz}}{\alpha} \\[2mm] \delta = L\sin\alpha \end{array}\right\} R = \dfrac{w_{laz} L}{\delta} \tag{2.2}$$

In a bent cantilever beam of bending radius R, the strain along the cantilever thickness is given by:

$$\varepsilon(y) = \frac{y}{R} \tag{2.3}$$

Where, y is the position within the thickness beam relatively to its neutral axis (i.e. where the stress is zero).

In our case, since the thickness of the laser-affected layer is orders of magnitude smaller than the thickness of the unaffected layer, we have $d_s >> d_f$. The maximum strain in the laser-affected layer can therefore be approximated by:

$$\varepsilon_{max} = \frac{d_s}{2R} \tag{2.4}$$

Using equations (2.1), (2.2), (2.3) and (2.4), from the deflection of the cantilever, with this simple continuous model, we calculate the average strain and stress in the laser-affected zone.

$$\varepsilon(\delta) = \left(\frac{d_s}{2w_{laz}}\right)\frac{\delta}{L} \quad , \quad \sigma_{xx}(\delta) = \left[\frac{E_s d_s^2}{6w_{laz}\left(1-v^2\right)d_f}\right]\frac{\delta}{L} \tag{2.5}$$

To test the influence of the sequential nature of laser scanning (laser-affected zones forming the layer, are typically formed by juxtaposing multiple adjacent laser-affected zones), one can use a second model based on finite-element modeling (FEM). This model considers a plane-strain hypothesis with elliptical cross-section representative of the laser-affected zones whether they contain nanogratings or not (Fig. 20).
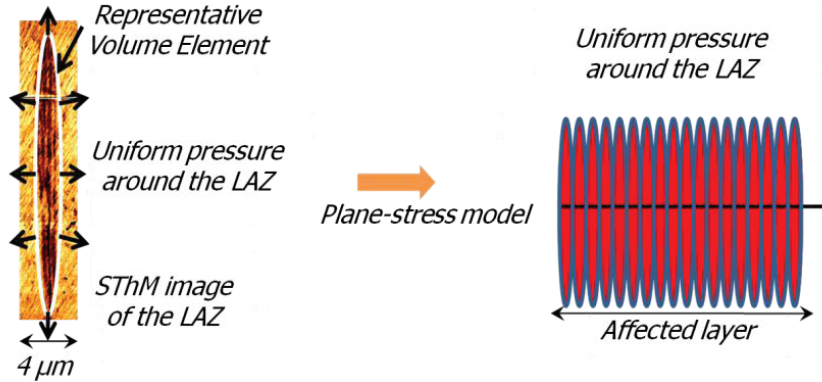
Fig. 20. Left: AFM-SThM image of a single laser affected zone [2] representing the Representative Volume Element. Right: portion of the affected layer made of adjacent laser affected zones.

The FEM model is implemented in a commercial software package (COMSOL). A rectangle representing the fused silica cantilever on which we add the affected layer made of loaded ellipses forming a row is used the simulate the stress and deformation in the layer. We used adaptive meshing to locally increase the density of elements near the laser-affected-zones. To simplify, we assume

that, whether there are nanogratings structures or not, from a micromechanical and volume variation point-of-view, laser-affected zones can be represented by a homogeneously modified elliptical zone that defines a representative volume element (RVE) (see Fig. 20). This choice is supported by scanning thermal microscopy measurements of laser-affected zones created under similar conditions [2]. Note that this model could be further refined by adopting a multi-scale modeling approach. In this model, the representative volume elements are loaded with a uniform stress distribution applied normal to their contours (left Fig. 20). The stress sign is chosen according to the measured deflection (δ), and can be either positive or negative depending on the case. The finite element model is used to derive a stress versus deflections relation which is then used to extrapolate the corresponding stress for any measured deflection.

Since the laser-affected zone size varies with the energy per pulse, we use a model following a similar hypothesis as described in [3] to estimate the affected layer thickness in the bimorph material (described above) according to the intensity threshold at which the laser beam starts to be absorbed and the energy per pulse.

To do so, we consider a Gaussian beam propagating along the optical axis z represented in Fig. 21. Its complex electric field propagating along z, expressed in V/m, can be described with the following equation:

$$E(r,z) = E_0 \frac{W_0}{W(z)} \exp\left[\frac{-r^2}{W^2(z)}\right] \exp\left[-ikz - ik\frac{r^2}{2R(z)} + i\varsigma(z)\right]$$

$$R(z) = z\left[1 + \left(\frac{z_0}{z}\right)^2\right] \tag{2.6}$$

where, r is an axis perpendicular to the optical axis z. $W(z)$ is the beam waist defined at $(1/e)^2$, k is the wave number and equal to $2\pi/\lambda$ and expressed in Rad/m, E_0 is the amplitude of the electric field, in the center of the beam where we defined the origin, i.e. $E_0 = E(0,0)$. W_0 is the waist for $z=0$. R is the radius of the curvature of the wave front envelope (Gaussian beam propagation), $z_0 = \pi W_0^2/\lambda$ is the so-called Rayleigh distance representing the depth of field and finally, $\varsigma(z)$ is the Gouy phase expressed by arctan(z/z_0). This phase occurs when the Gaussian beam propagates passing through its focal point. It is an additional phase shift of π.

The average intensity (or radiance) expressed in W/m^2 is defined as follows, from eq. (2.7):

$$I(r,z) = \frac{|E(r,z)|^2}{2\eta} = I_0\left[\frac{W_0}{W(z)}\right]^2 \exp\left[\frac{-2r^2}{W^2(z)}\right] \tag{2.7}$$

where η is the impedance in free space. It is the ratio between electric field magnitude and magnetic field magnitude when the electromagnetic wave

propagates in free space. I_0 is the intensity of the electric field. The peak intensity I along z according to the power (that we effectively measured in experiments) is expressed by eq. (2.8):

$$I = \frac{2P_0}{\pi W^2(z)} \tag{2.8}$$

The absorption of ultra-short pulses by fused silica is non-linear due to the high bandgap of the material (see chapter I). In the model [3], it is assumed that a certain intensity threshold I_r needs to be reached before full absorption occurs. The laser-affected zone where this condition is met, is shown in Fig. 21.
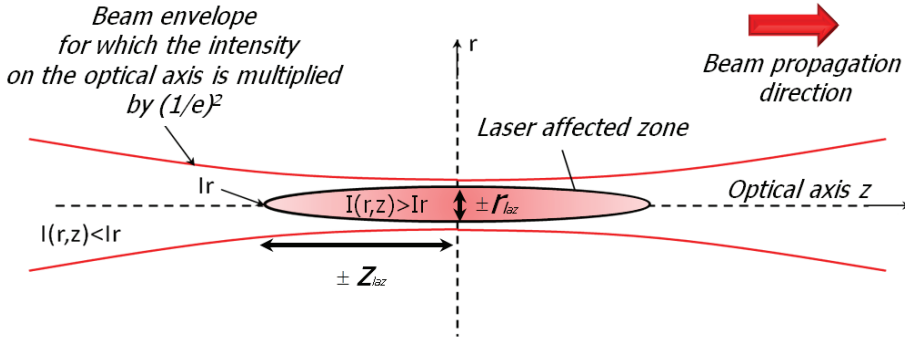
Fig. 21. Laser-affected zone as a function of a threshold intensity I_r.

Assuming that I_r is the intensity threshold above which the laser beam is fully absorbed by fused silica, from the Gaussian propagation equation and Eq. (2.7), the width of the beam is expressed according to z as follows (for $r = 0$).

$$W(z, r=0) = \sqrt{\frac{W^2 I_0}{I_r}} = W_0 \sqrt{1 + \left(\frac{z}{z_0}\right)^2} \tag{2.9}$$

where $z_0 = \pi W_0^2/\lambda$. The condition for the beam to be absorbed along z axis is extracted from eq. (2.9) as a function of threshold intensity I_r and the measured intensity I_0 of the beam in eq. (2.10):

$$z_{\text{LAZ}} = \pm \frac{\pi n W_0^2}{\lambda} \sqrt{\frac{I_0}{I_r} - 1} \quad with \quad I_0 \geq I_r \tag{2.10}$$

This expression defines the boundaries along the z-axis of the laser-affected zone domain.

Likewise, using eq. (2.7) and (2.9), we express the boundary of the modified zones at $z=0$ that we call r_{LAZ}. At $z = 0$, $W(z) = W_0$ and therefore, r_{LAZ} is expressed according to I_r and I_0 by the eq. (2.11):

$$r_{LAZ} = \pm\sqrt{\frac{W_0^2}{2}\ln\left(\frac{I_0}{I_r}\right)} \quad with \quad I_0 \geq I_r \qquad (2.11)$$

These two boundaries of the laser-affected domains give us the thickness of the affected layer as well as the minimum required spacing between laser-written lines.

3.   Experiments in the pulse length regime where nanogratings are found

a. *Laser system*

We use a femtosecond laser oscillator (t-Pulse 500 from Amplitude Systèmes) emitting 380 fs-pulses at 1030 nm and at a chosen repetition rate of 860 kHz. The pulse energy is set to 220 nJ. The focusing optics consists of a microscope objective (OFR, LMH X20-1064) with a numerical aperture (NA) of 0.40. With these laser exposure specifications, we are in the nanogratings regime as confirmed by backscattered scanning electron microscope (SEM) observations. In reference [4], we demonstrated the influence of the amount of deposited energy on the etching rate. Here, we test increasing levels of deposited energy, ranging from 6 J/mm^2 to 150 J/mm^2, so that the results can be compared with this previous study performed in our group on the influence of deposited energy on etching rate.

b. *Cantilever preparation*

The cantilevers (shown in Fig. 22) are fabricated using the same laser as specified above and using the two-step process described in the previous chapter and thoroughly described in [5]. As processing parameters, we have used a scanning speed of 5 mm/s, a pulse energy of 220 nJ, a repetition rate of 860 kHz and an NA of 0.40. After chemical etching in low-concentration HF (2.5 %), the cantilevers are again exposed to the laser beam, but this time only in their upper-half thickness. The substrates used are 25 mm-squares with a thickness of 500 micrometers. The material is an OH-rich fused silica. The cantilever exposure is done by scanning adjacent lines (going back and forth and overlapping) with two-micrometers spacing over a width of 5 mm. The writing speed was varied in order to obtain the specified deposited energy. The writing was tested with two linear polarizations, namely parallel and perpendicular to the cantilever axis.
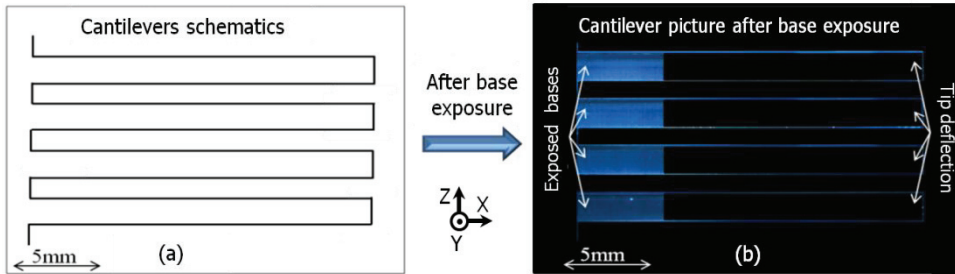
Fig. 22. (a) Schematics of the cantilevers before re-exposure. (b) Optical microscope image of laser-exposed cantilevers taken with a microscope operating in reflection-mode.

c. *Lines for etching comparison*

Using the same type of substrates, we made a series of lines below the surface with the same energy deposition and exposure conditions. This specimen is used to correlate the measured deflections with the etching rate. The experimental protocol to measure the etched length is described in [6]. The edge of the sample is polished to reveal the lines, so that the etchant can penetrate in the lines. The sample is immersed in an HF bath during 4 hours at 2.5 % concentration.

d. *Deflection measurement*

Fig. 23 shows the cantilever deflection as a function of the energy deposition. It is displayed for both polarizations (transverse/parallel to the writing direction). A confocal microscope (Sensofar - PLµ2300) was used to measure the deflection with an estimated error of +/- 0.1 µm.
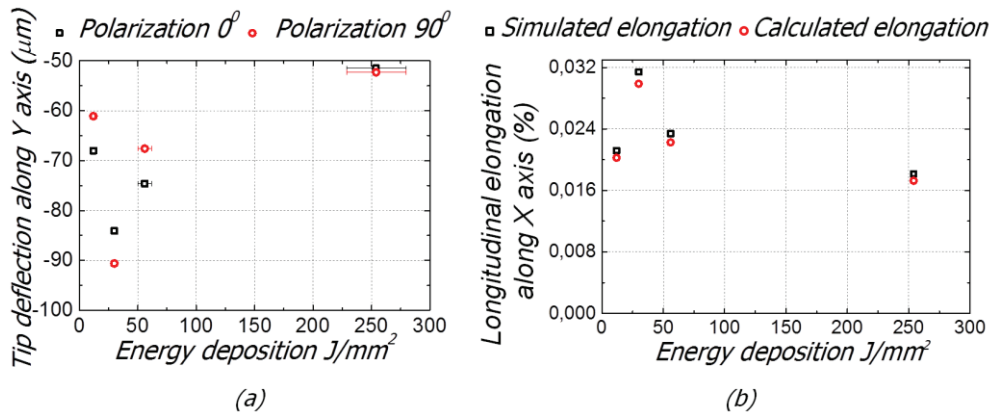
Fig. 23. Deflection measurements (a) and equivalent elongation (b) for different levels of energy depositions and for two different polarization states. The deflection measurement error is +/- 0.1 µm.

Thanks to the amplification mechanism, the data span from 50 to 90 μm. For this particular exposure condition (regime II), we observe a negative deflection along the Y-axis, indicating a net volume expansion after exposure. Furthermore, we note a possible weak-dependence with the polarization.

e. *Corresponding stress in the laser-affected zones*

Using Eq. (2.5) applied to the deflection measurements, we estimate the principal stress in the laser-affected zones (see Fig. 24) The data are also compared with the results from the FEM simulations.
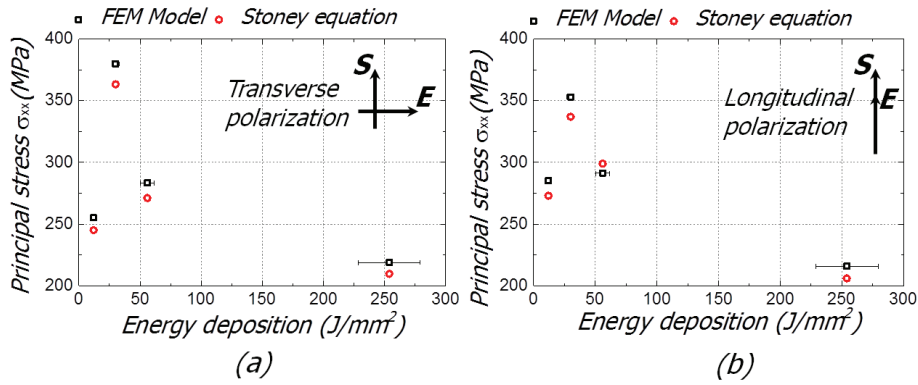
Fig. 24. Calculated stress using the continuous and discrete model for transverse (a) and longitudinal (b) polarization defined with respect to the writing direction (s).

For this particular experiment, the maximum elongation variation is estimated to be 0.03%. The FEM model predicts on average a 5 % higher stress than the continuous analytical model. This could be due to the stress concentration at the top and bottom of representative volume elements that could increase slightly the average stress whereas in the continuous model the stress is uniform everywhere.

f. *Effect of the energy deposition on the etching rate*

The etching rate dependence on the energy deposition after femtosecond laser exposure has been shown in a previous work [4] in our group. Here, we reproduce these experiments but with identical laser exposure conditions as those used for the cantilever experiments. The results are shown in Fig. 25.
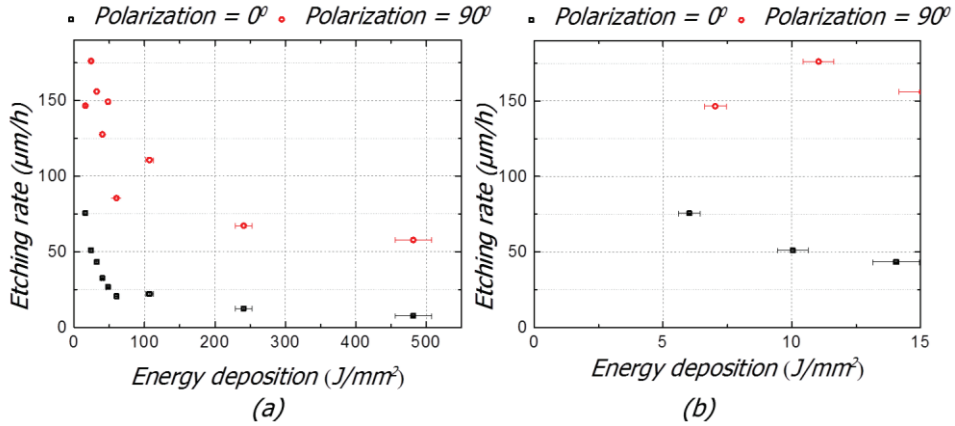
Fig. 25. Graph comparing both polarizations in terms of etching rate. Left: graph with every measurement (a). Right: Zoom of the first graph to see better the maximum etching rate (b). We measure the etched length with an optical microscope (10x objective). The error is estimated to be +/- 1µm.

The etched length grows steeply and reaches a maximum for energy deposition ranging between 10 and 20 J/mm^2 for both polarizations. For the perpendicular-to-the writing-direction polarization, the etching rate is about twice higher than for the parallel-to-the-writing-direction one which is consistent with previous observations [4].

The maximum cantilever deflections and the maximum etched lengths are found at about the same energy deposition level (i.e. between 10 and 30 J/mm^2), suggesting a strong correlation between the two phenomena, i.e. etching rate enhancement efficiency and stress build-up in the material.

g.   *Evolution of Raman spectra as a function of the deposited energy*

Fused silica consists of randomly arranged rings of various sizes and having SiO_4-tetrahedra as basic component. The oxygen atoms sit at the corners of each tetrahedron and are shared with two adjacent tetrahedra. The bond angle decreases under a compressive stress and increases under a tensile stress [7]. Bond angle variation can be observed using Raman spectroscopy that provides information related to structural changes in the glass caused by mechanical stress. For SiO_2, three fundamental vibrations bands located between 450 and 1200 cm^{-1} [8-9] are observed: asymmetric stretching (AS) from 1050 to 1100 cm^{-1}, symmetric stretching (SS) or bending mode from 790 to 810 cm^{-1} and symmetric oxygen stretching or bending-rock (R) from 440 to 470 cm^{-1}.

These modes are depicted in Fig. 26. These bands shift when the bond angle Si-O-Si changes: the band at 1050 shifts to a higher wave number and the two others bands shift to a lower wave number [9]. Two peaks at 490 and 604 cm^-

[1], called D_0 and D_2 respectively, are modified when the bond angle changes (mechanical densification shock wave [10]). Previous works [2,11,12] have reported that laser-induced modifications in fused silica produce visible changes in their Raman spectra. For instance, it was shown that the D_2 peak (at 605 cm^{-1}) increases in intensity. This change is interpreted [2,11,12] as a change of SiO_4 ring size toward smaller rings (n=3). The D_0 (located at 490 cm^{-1}) moves toward higher wave number for mechanically densified fused silica but also for femtosecond laser induced type I and II modifications [5].
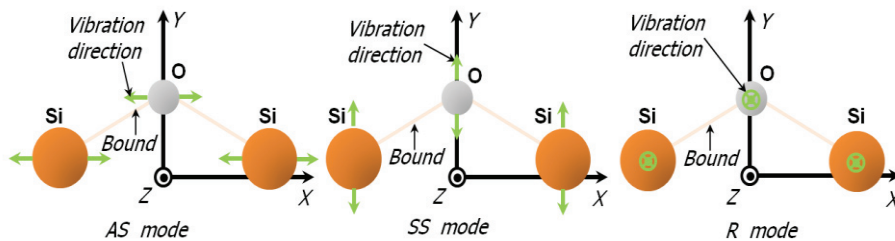
Fig. 26. Three vibration modes: Left. Asymmetric mode (wavenumber: from 1050 to 1100 cm^{-1}), atoms move along X axis. Right: Bending-Rock mode (wavenumber: from 440 to 470 cm^{-1}), atoms move along Y axis. Middle: Symmetric mode (wavenumber: from 790 to 810 cm^{-1}), atoms move along Z direction.

Note that in this 2D representation, the two additional S_i atoms are not visible. This is to simplify the figure. Raman spectra of the laser exposed areas for the same energy depositions used in the etching experiment discussed above, were measured. Characteristics Raman spectra are shown in Fig. 27. The reference spectrum is taken in the pristine zone of the silica. Measurements made without post-processing show a strong fluorescence background, due essentially to the color-centers (NBO) introduced by the laser that get excited with our Raman illumination conditions (632 nm-laser source). To remove the color-centers, the specimen is heated up to 150 °C for 10 hours. To make sure that the stress is not removed after heating, cantilevers are heated and their deflection measured after heating. The deflections remain at the same level. Therefore only color center responsible for scattering in the Raman spectrum are removed.
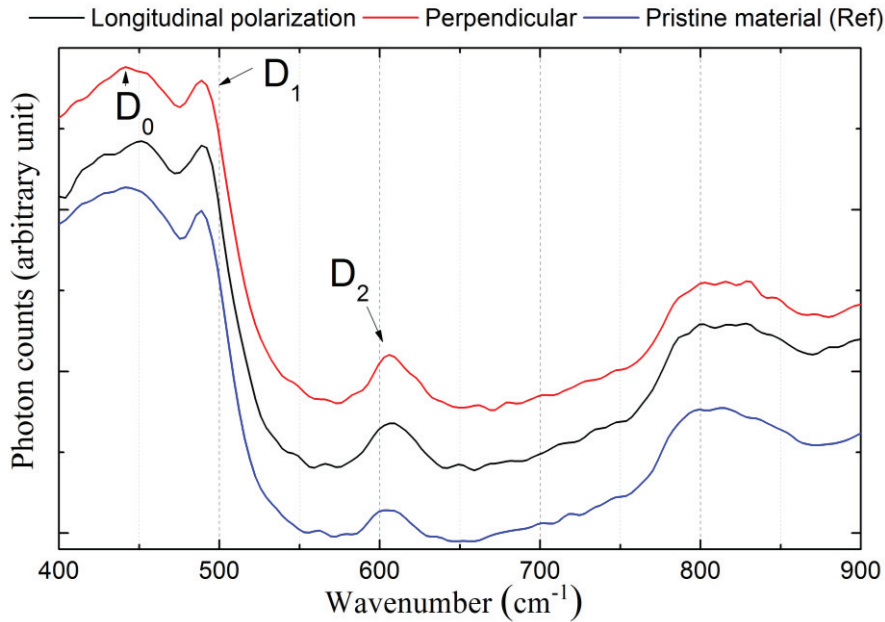
Fig. 27. Raman spectra for two polarizations (longitudinal and perpendicular to the writing direction) compared to a reference spectrum, measured in the pristine material. These curves are obtained after heating up the material at 150 °C to remove color-centers. The laser exposures for the longitudinal and perpendicular cases are: 10 J/mm^2 and 16 J/mm^2 respectively.

From each Raman spectrum taken at various levels of deposited energy and for the two polarization states, the D_2 peaks are extracted after normalization and compared. The results are shown in Fig. 28.

We observe a positive shift of the D_0-peak after exposure and an increase of the D_2-peak. These observations are consistent with our own observations made on mainly type I modifications, but also on nanogratings [2]. The bond angle decreases after laser exposure, indicating the possible presence of tensile stress in or around the LAZ, in the nanograting regime as well as the formation of lower-order rings. These Raman observations point towards a possible densification of the glass matrix. This is apparently contradicting the expansion phenomena observed for the cantilever. Note that the trend observed in Fig. 28 is the same for the etching length and for the cantilever deflection: a sharp increase followed by a gradual decay. This observation hints towards a rapid build-up of stress associated with structural modifications.
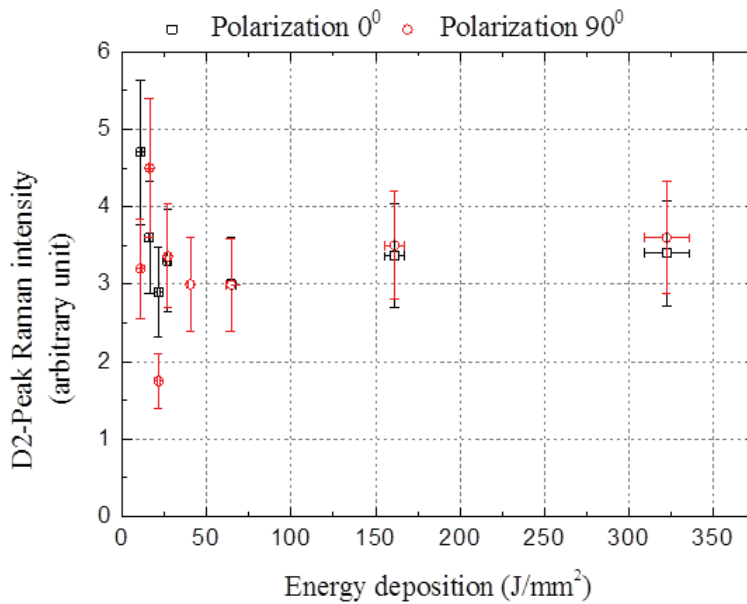
Fig. 28. D_2-peak variation as a function of the energy deposition level for both methods. After heating 10 h heating at 150 °C.

4.   Investigation of the transition regime between homogeneous and self-organized with shorter pulse duration

In the work of Hnatovsky et al. [13], the conditions of the existence of homogenously modified zones and nanogratings have been identified as a function of pulse energy and pulse duration (see Fig. 29). For low energies per pulse and short pulse duration (below 200 fs) homogeneous modifications occur (type I). At longer pulse and higher energies (but below the ablation threshold), self-organized nanogratings form. This regime is called Type II in Fig. 29.
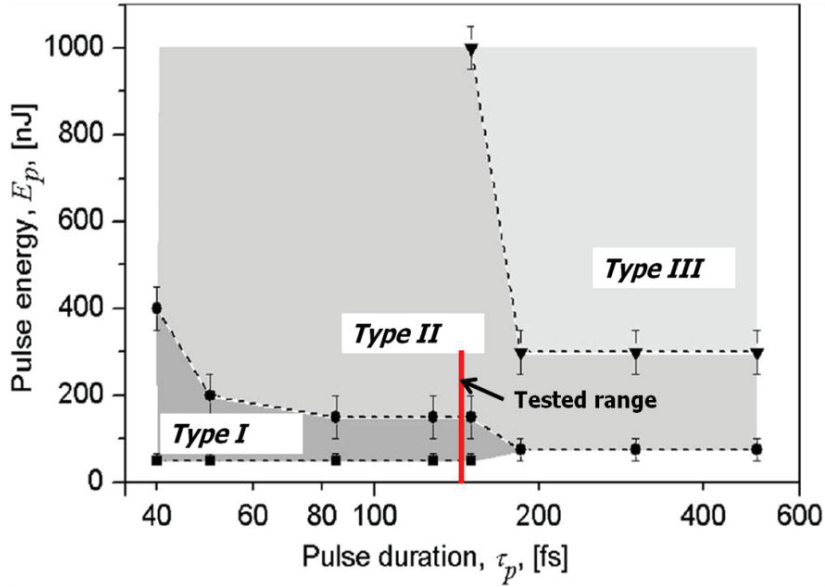
Fig. 29. Graph showing the three achievable regimes of structural modification of fused silica when exposed to a femtosecond laser (adapted from [13]), as a function of laser parameters. At low pulse duration (below 200 fs) and low pulse energy (below 200 to 400 nJ, depending on the pulse duration) smooth modifications are made after exposure (Type I). At higher pulse energy and higher pulse duration, nanogratings form in the transparent material (Type II). If the pulse duration is higher than 200 fs and the energy per pulse is higher than 300 nJ, disrupted nanogratings and ablation are observed (Type III).

Since we found a volume expansion of the laser-affected zone in the second regime, it is logical to use the cantilever method to quantify and identify the stress state in the first regime and in particular, to verify if it is consistent with a densification model as reported in [2,11,14]. Furthermore, it is particularly interesting to investigate the transition between regimes.

a.   *Energy per pulse effect*

As the energy per pulse seems to influence the regimes change according to [13] we use the cantilever method, to test a range of energy per pulse ranging from 150 to 300 nJ as shown Fig. 29 in red. The writing speed is set to 4.8 mm/s. The laser light polarization is chosen perpendicular to the writing direction to optimize the amplitude of the deflection (when nanogratings form) since we observe higher deflections when nanoplanes are oriented parallel to the writing direction (transverse polarization in Fig. 24). The measured deflections for each energy

depositions and the equivalent stress around the laser-affected zone calculated from Stoney's equation are shown in Fig. 30.
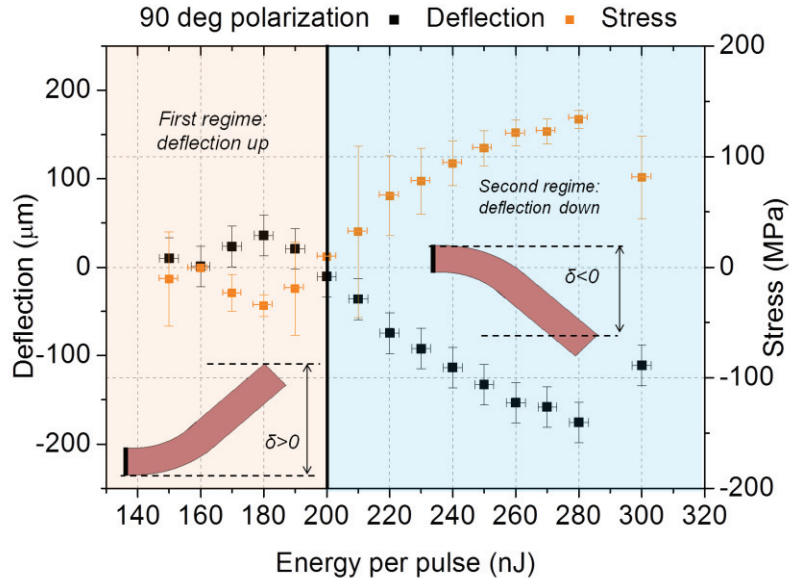
Fig. 30. Measured deflections and corresponding, calculated stress levels as a function of pulse energy.

A densification in the low-energy regime takes place whereas a volume expansion at higher pulse energies is observed. The transition between the two regimes seems to occur around 200 nJ which corresponds to about 6 J/mm² with our fixed speed and repetition rate (100 kHz). In the regime where upward deflections are measured, we observe a maximum average stress of about 36 MPa. As the energy per pulse is increased, the stress decreases until a stress state inversion is observed. In the second regime, we observe an increase of downward deflections until a maximum stress of 150 MPa corresponding to an energy deposition of 7 J/mm² is measured. As the energy is further increased, the stress decreases again suggesting the occurrence of cracking in the laser-affected zone.

In an attempt to correlate structural changes (from continuous to nanogratings) with the stress-state inversion, we have systematically investigated the morphology on cross-section of laser-affected zones. To do so, we have written lines in the bulk of fused silica at about 30 μm below the surface. The same fused silica substrates used for the cantilever experiments and the same laser exposures to load the cantilevers are used. The sample is polished to reveal the cross-section of the lines. The sample is etched during five minutes to reveal the morphology of the laser-affected zones. A thin gold layer (~ 50 nm) is

deposited on the sample as a preparation step for scanning electron microscope (SEM) observations.

The SEM pictures in Fig. 31 illustrate various morphologies of the transverse cut of the laser-affected zones. These images are all taken with the same magnification level for accurate comparison.
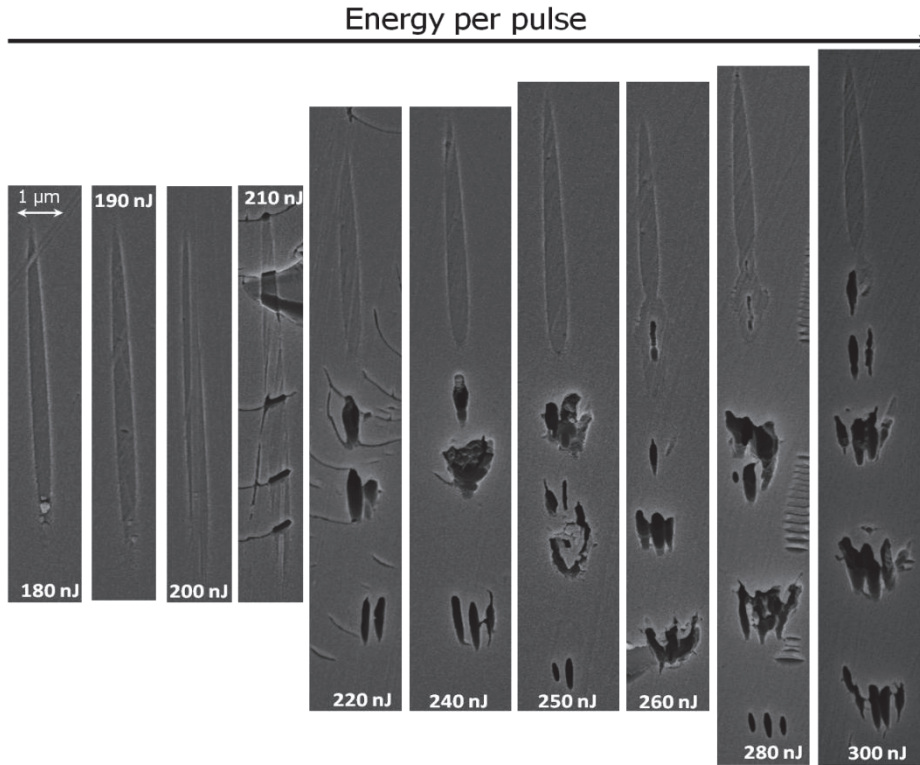
Fig. 31. SEM images showing the morphology on cross-section of laser-affected zones' for the transition between the first and second regime.

The transition between "homogeneous morphology" and some early stage of nanogratings formation seem to occur between 210 nJ and 220 nJ whereas in the graph Fig. 30, the stress-state inversion took place at 200 nJ, which would suggest that the expansion regime is not necessarily linked to the nanogratings formation.

b. *Energy deposition effect*

It is interesting to test the role of energy deposition in the first regime and in particular, to test whether a peak stress intensity exists like in the case of the nanogratings regime. To do so, we measure the stress for a fixed pulse energy

(here we chose 160 nJ, i.e. well-below 200 nJ to make sure we are in the first regime) and for six different writing speeds ranging from 1 mm/s to 12 mm/s.
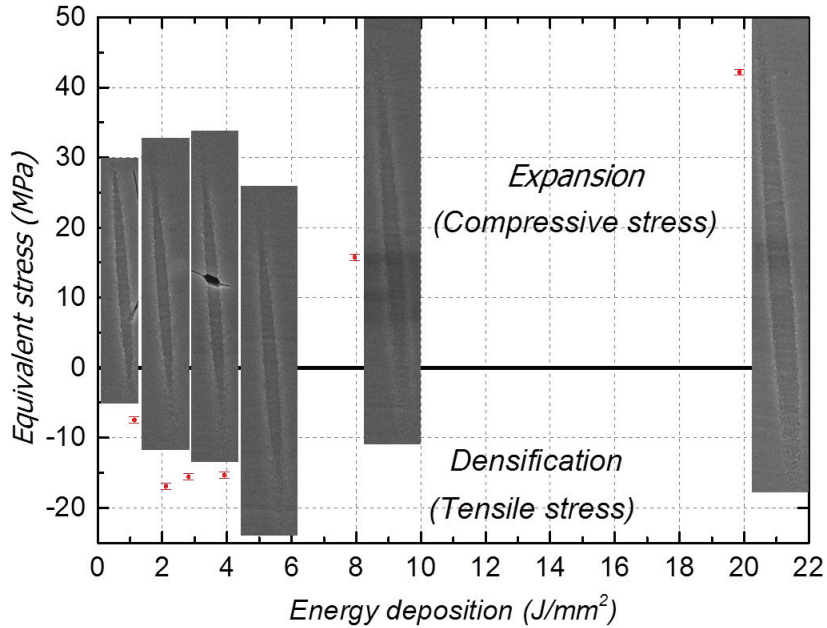
Fig. 32. Stress around laser-affected zones as a function of energy deposition. SEM images for each single line that show the morphology of the affected areas are placed next to each measurement.

In Fig. 32, the stress is plotted according to the energy deposition. We observe an increase of the tensile stress when the energy deposited increases. As the energy deposited is further increased, the stress reaches a maximum (up to 16 MPa) and starts to decrease and switches state between 4 and 8 J/mm^2 which is consistent with the energy per pulse effect experiment where we found the transition at about 6 J/mm^2. This maximum could be attributed to the fact that the material densifies at low energy deposition forming smaller rings in the Si-O-Si matrix. At some point the material cannot be densified anymore, which could explain the lowering of the stress in the material due to two competing phenomena: densification and nanopore formation.

The corresponding SEM images representing the transverse cut of lines, (obtained in the same way as for the experiment with the energy per pulse above), show a homogeneous morphology despite the occurrence of a stress state inversion. This means that the expansion regime is not necessarily related to nanogratings formation as noticed in the increasing energy-per-pulse experiment. Another phenomenon takes place before nanogratings formation. We suspect the presence of nanopore to be the cause of this phenomenon.

c. *Correlation with the etching rate of silica in the first regime.*

We measured the etching rate in writing lines in fused silica (as describe above in 3.f) at the same energy depositions used for the cantilevers experiment in the first regime. In Fig. 33 the etching rate is plotted according to the energy deposition for both polarizations.
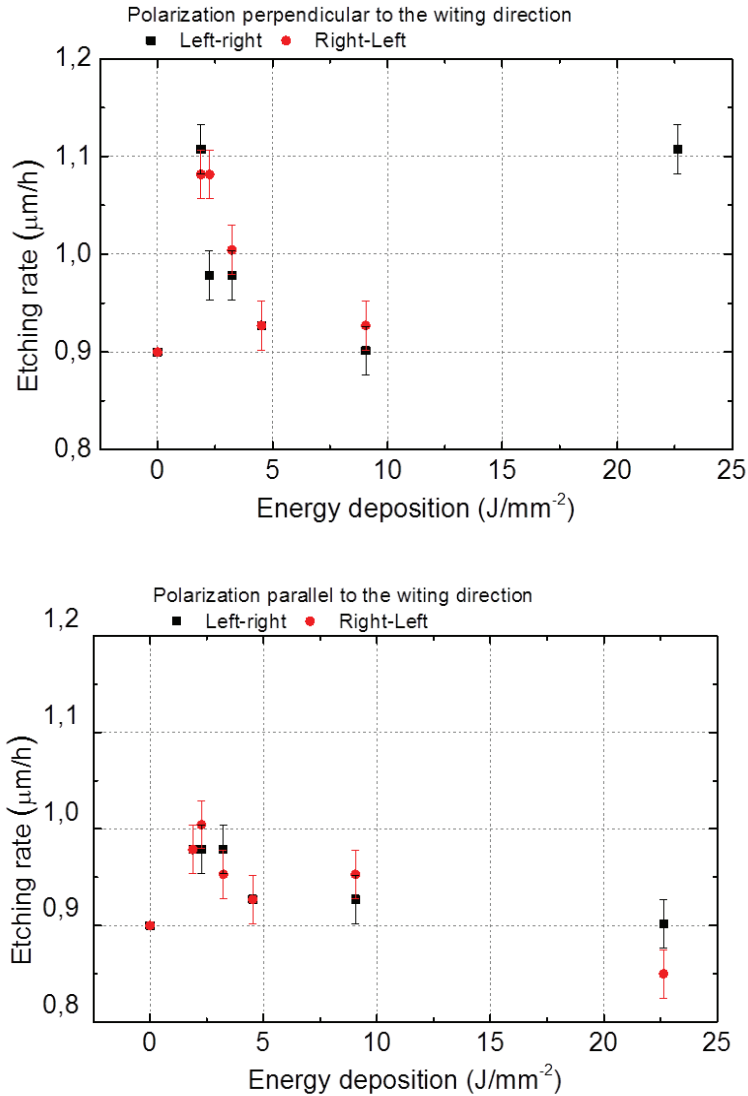
Fig. 33. Etching rate in the first regime: Top: Polarization perpendicular to the writing direction Bottom: polarization parallel to the writing direction. We clearly see that the polarization influences the etching rate in the homogeneous regime.

A maximum etching rate is found for the energy deposition at which the maximum tensile stress is found. The etching rate is lower than in the second regime and among of stress is not higher than 20 MPa. This is consistent with the hypothesis that the stress could enhance the etching rate.

The polarization also seems to play a role in the etching rate and in the stress in the first regime. This could be explained by the influence on the Fresnel coefficient absorptions which are polarization dependent.

5.   **Discussion and interpretation**

a.   *Laser exposure below 200 fs pulse duration*

Our cantilever method has confirmed that, for pulse duration below 200 fs, the material, at low pulse energy or low energy deposition, densifies. The transition between tensile stress and compressive stress occurs at about 6 J/mm^2 with a pulse duration equal to 150 fs. The maximum tensile stress corresponds to a deformation of 0.01%.The maximum tensile stress occurs at about 2 J/mm^2 and is correlated to the etching rate (like in the case of the second regime).

SEM observations, in both cases (energy deposition and energy per pulse effect), of the LAZ show that the expansion regime does not necessarily occur when nanogratings form.
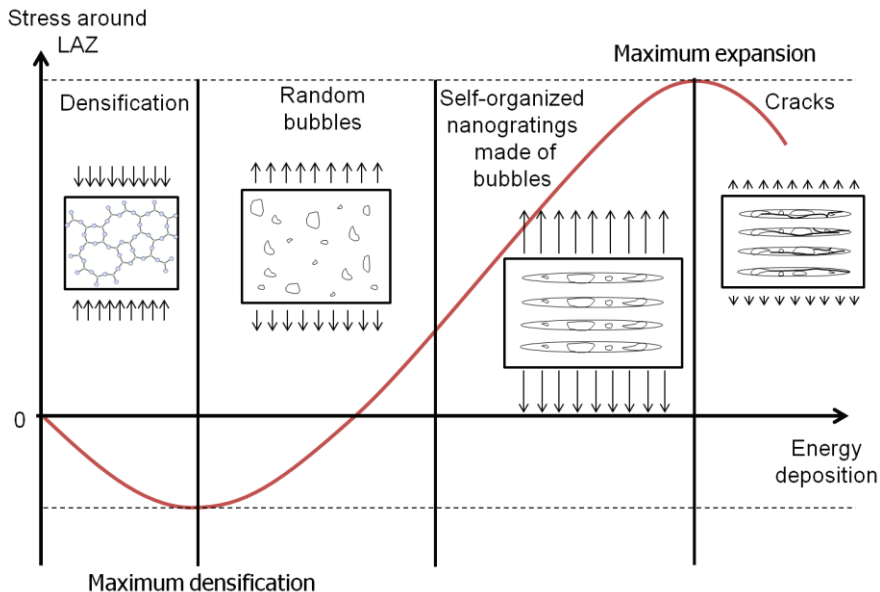
Fig. 34. Proposed scenario to explain the volume variation phenomena observed at shorter pulse duration (150 fs).

A scenario is proposed in Fig. 34. For shorter pulses or low energy per pulse, densification occurs due to the formation of smaller rings in the Si-O-Si matrix when bonds are broken. At a certain point the material cannot be modified anymore and porous material [6] starts to form, causing a net volume expansion that balances the densification. This mechanism would decrease the tensile stress surrounding the laser-affected zones, eventually leading to a stress-state inversion when the nanopores-driven volume expansion overcomes densification effects.

b.   *Laser exposure above 200 fs pulse duration*

At longer pulses (380 fs) where nanogratings are found, the laser-affected zone expands. The relative estimated deformation is 0.03 %. With pulse duration above 200 fs porosities in nanogratings can directly form due to the high plasma density. In a paper from J. Canning et al. [6], an explanation is proposed for silica oxide decomposition in nanoplanes: inhomogeneous multiphoton ionization leads to localized high plasma density and therefore a high ponderomotive force (due to large the intensity gradient). The large intensity creates local self-focusing (due to the Kerr optical effect) leading to inhomogeneous ionization in nanoplanes. In this case the strongest intensity gradient is radially oriented inward so that the ponderomotive force pushes electrons outside of the region of high intensity. As a result, a centrifugal electrostatic force extracts oxygen atoms from the network. Later created aggregate recombine in the form of bubbles.

c.   *Nanogratings morphology*

The cantilever experiments, Raman and form birefringence observations, contradict the model assuming that nanogratings are de facto cracks [15]. Cracks may be found when the stress concentration in the nanogratings is sufficiently high but do not form ab-initio [2]. The formation of a porous material made of nano-scale pores can account for the expansion we are observing in laser-exposed cantilevers. On the other hand, the Raman spectra suggest the presence of lower-ring numbers in the cantilevers laser-affected zones. Lower-ring numbers would induce a densification and therefore, an opposite effect to what we are observing in cantilevers.

A few pulses → Many pulses

Homogeneous
Laser
affected
zones

*Gradual formation
of a self-organized
porous structure
Stress builds-up
in the materail as
the material is pushed
away, possible
densification
in between pores.*

*Stress and number
of pores increases
further, higher
densification level
in between pores*

*Porous structure ruptures,
crack nucleation, formation
of random non-affine
open interfaces*

Fig. 35. Proposed scenario to explain the various phenomena at longer pulse duration (380 fs).

To reconcile the two observations, we propose the following scenario, outlined in Fig. 35. If we assume that the LAZ consists of porous material (in the nanogratings), every nano-scale bubble during their formation would induce the formation of compressively stressed zones surrounding them that, if high enough, can locally induce a mechanical densification. The stress is also responsible for bond angle variations in the SiO_2 matrix that explain a faster etching rate in the LAZ. The correlation between stress and etching rate was shown in [16]. This supports the similar trend we are observing between the cantilever bending and the etching rate. The two experimental curves have similar features and show a characteristic maximum for the same deposited energy levels.

We note that the etching rate also depends on the deposited energy. A maximum etching rate is observed for a given level, here about 20 J/mm^2. The presence of this maximum suggests that the stress gradually builds up as the material is repeatedly 'hammered' by the femtosecond laser. When this stress becomes too high, cracks nucleate randomly and stress relaxation is observed globally in the LAZ explaining the reduced etching rate as well as the lowering of the cantilever deflection. The cantilevers do not completely recover their deformation due to the formation of irreversible, non-affine open interfaces. The increased etching rate is also still observed because some irreversible densification took place in an earlier phase of the process, prior to the formation of cracks. The

presence of open pores may offer a path for the etchant to penetrate inside the material but overall, the etching mechanism is much less efficient than the densification-driven and stress-induced ones. This model is also compatible with the etching rate polarization anisotropy [4].

The laser exposure condition segregates densified zones in the narrow bands forming the nanogratings. If these zones are connected longitudinally, this will indeed favor the etching rate, while a parallel assembly of nanogratings will be less efficient. Our observations show that in both polarization cases, the formation of cracks slows down substantially the etching rate.

6.   Conclusion

In this chapter, we have demonstrated a method to quantitatively estimate the level of effective volume changes in laser-affected zones after femtosecond laser exposure. This method has been applied, for a range of pulse durations that lead to different type of structure modifications. In particular, we have shown that for nanogratings, observed with longer pulses, a volume expansion is taking place and that the energy deposition has an influence on the volume variation that can be correlated to both Raman spectra and etching rate. With shorter pulses, we observed a stress state inversion as well as a maximum tensile stress that can be correlated to a peak in the etching rate enhancement.

We observed that the pulse duration influences the possible regimes reachable. For longer pulses, the homogeneous regime was not reached. This is consistent with the work of Hnatovsky et al. [13], where the type of structural modifications depends on the pulse duration. For instance, they reported that the first regime cannot be reached with a pulse duration higher than 200 fs.

With shorter pulses, we observed that the expansion regime does not systematically correspond to the nanogratings formation. Indeed, SEM images of the laser-affected zones show homogeneous modifications after the state stress inversion whether the pulse energy or the energy deposited is increased.

We interpret volume expansions by the formation of a porous structure, both in nanogratings or in homogeneous modification. A maximum of stress is observed in both regimes as the energy deposition increases and is correlated with the maximum etching rate at the same energy depositions. This observation emphasizes the role of the stress in the etching rate and its importance for accurately controlling etched patterns according to the laser parameters.

This new stress measurement is efficient but not fast and requires a lot of cantilevers to be able to optimize the laser parameters. Furthermore, the nanograting orientations should change the stress distribution around lines. Therefore, it would be interesting to use another method to quantify rapidly the stress around the laser-affected zones, and to test the influence of the nanogratings orientation on the stress distribution around them [17].

In the next chapter, we propose a second method for quantifying the stress in and around the laser-affected zone and we test the influence of nanogratings orientation on the stress distribution around laser-written lines.

7.   References and Links

1. G. G. Stoney, "The Tension of metallic films deposited by electrolysis," Proc. R. Soc. London, Ser. A **82**, 172–175 (1909).
2. Y. Bellouard, E. Barthel, A. A. Said, M. Dugan, and P. Bado, "Scanning thermal microscopy and Raman analysis of bulk fused silica exposed to low energy femtosecond laser pulses," Opt. Express **16**, 19520-19534 (2008).
3. D. Rayner, A. Naumov, and P. Corkum, "Ultrashort pulse non-linear optical absorption in transparent media," Opt. Express **13**, 3208–3217 (2005).
4. S. Rajesh and Y. Bellouard, "Towards fast femtosecond laser micromachining of fused silica: The effect of deposited energy," Opt. Express **18** (20), 21490–21497 (2010), doi:10.1364/OE.18.021490.
5. Y. Bellouard, A. Said, M. Dugan, and P. Bado, "Fabrication of high-aspect ratio, micro-fluidic channels and tunnels using femtosecond laser pulses and chemical etching," Opt. Express **12**, 2120-2129 (2004).
6. J. Canning, M. Lancry, K. Cook, A. Weickman, F. Brisset, and B. Poumellec, "Anatomy of a femtosecond laser processed silica waveguide [Invited]," Opt. Mater. Express **1**, 998–1008 (2011).
7. H. Sugiura, and T. Yamadaya, "Raman-scattering in silica glass in the permanent densification region," J. Non-Cryst. Solids **144**, 151-158 (1992).
8. J. Bell, and P. Dean, "Atomic vibrations in vitreous silica," Discussion Faraday Soc. **50**, 55 (1970).
9. F.L.Galeener, "Band limits and the vibrational spectra of tetrahedral glasses," Phys. Rev. B **19**, 4292–4297 (1979).
10. M. Okuno, B. Reynard, Y. Shimada, Y. Syono, and C. Willaime, "A Raman spectroscopy study of shock-wave densification of vitreous silica," Phys. Chem Mineral **26,** 304-311 (1999).
11. J. W. Chan, T. Huser, S. Risbud, and D. M. Krol, "Structural changes in fused silica after exposure to focused femtosecond laser pulses," Opt. Lett. **26**, 1726–1728 (2001).
12. W. J. Reichman, D. M. Krol, L. Shah, F. Yoshino, A. Arai, S. M. Eaton, and P. R. Herman, "A spectroscopic comparison of femtosecond-laser-modified fused silica using kilohertz and megahertz laser systems," J. Appl. Phys. **99**, 123112 (2006).
13. C. Hnatovsky, J. R. Taylor, P. P. Rajeev, E. Simova, V. R. Bhardwaj, D. M. Rayner, and P. B. Corkum, "Pulse duration dependence of femtosecond-laser-fabricated nanogratings in fused silica," Appl. Phys. Lett. **87**, 14104-14106 (2005).
14. Y. Bellouard, T. Colomb, C. Depeursinge, M. Dugan, A. A. Said, and P. Bado, "Nanoindentation and birefringence measurements on fused silica specimen exposed to low-energy femtosecond pulses," Opt. Express **14** (18), 8360–8366 (2006), doi:10.1364/OE.14.008360.
15. R. Taylor, C. Hnatovsky, and E. Simova, "Applications of femtosecond laser induced self-organized planar nanocracks inside fused silica glass," Laser Photonics Rev. **2**, 26–46 (2008).

16. A. Agarwal, and M. Tomozawa, "Correlation of silica glass properties with the infrared spectra," J. Non-Cryst. Solids **209**, 166–174 (1997).
17. M. Beresna, M. Gecevičius, P. G. Kazansky, and T. Gertus, "Radially polarized optical vortex converter created by femtosecond laser nanostructuring of glass," Appl. Phys. Lett. **98**, 201101–201101–3 (2011).

Chapter III. Effect of nanogratings orientation on stress distribution

This chapter introduces a second experimental method to investigate the stress *around* laser-affected zones. The method is based on stress-induced birefringence measurements. Complementary to the experimental method presented in chapter II, this second approach provides direct and rapid insights on the importance of laser beam polarization on stress distribution. This method shows that the nanogratings orientation play a role on the stress distribution. Finally the morphology of the self-organized nanogratings is investigated according to the energy deposition.

This chapter has been reported in a different form in: A. Champion, M. Beresna, P. Kazansky, and Y. Bellouard, "Stress distribution around femtosecond laser affected zones: effect of nanogratings orientation," Opt Express **21**, 24942–24951 (2013).

1. Introduction

In the previous chapter, we have presented evidences of a net volume expansion when nanogratings are found in the laser-affected zones. This relative volume change induces, stress *around* laser-affected zones [1].

Furthermore, the polarization dependence on the optical retardance observed *inside* laser tracks depends also on stress and pulse front tilt [2]. Although stress is observed in the laser-affected zones, the stress around nanogratings is not investigated due to the small size of nanogratings.

From the micromachining point of view, since nanogratings are oriented perpendicular to the electric field of the laser light and considering their anisotropic structure, one can assume that the stress distribution around laser-written lines should also be polarization dependent. From a structural change point of view, the high stress (GPa order) in between nanogratings could lead to possible polymorphic-phase changes since the material is locally under high compressive stress.

In this chapter, we investigate a method for measuring the stress surrounding laser-affected zones and in between platelets that form the nanogratings, for various exposure conditions and polarization.

2. Hypothesis

Nanogratings consist of self-organized planar structures or lamellae. Based on recent observations from Canning et al. [3], we assume that nanogratings lamellae are made of porous material (see Fig. 36 left). This porous material could be the result of a localized glass matrix decomposition and the release of oxygen during the laser interaction [3]. This hypothesis is consistent with the observed volume expansion reported in [1].

From these experiments, a pressure (σ_θ) (Fig. 36 right) has been estimated as a function of the energy deposited in the material. A direct consequence of the lamellae-expansion hypothesis is that the stress surrounding laser-written lines should depend on the nanogratings orientation (i.e. the lamellae orientations with respect to the writing direction). In particular, this orientation dependence of stress observed at the microscale could be used to indirectly determine the stress surrounding individual lamellae at the nanoscale level.
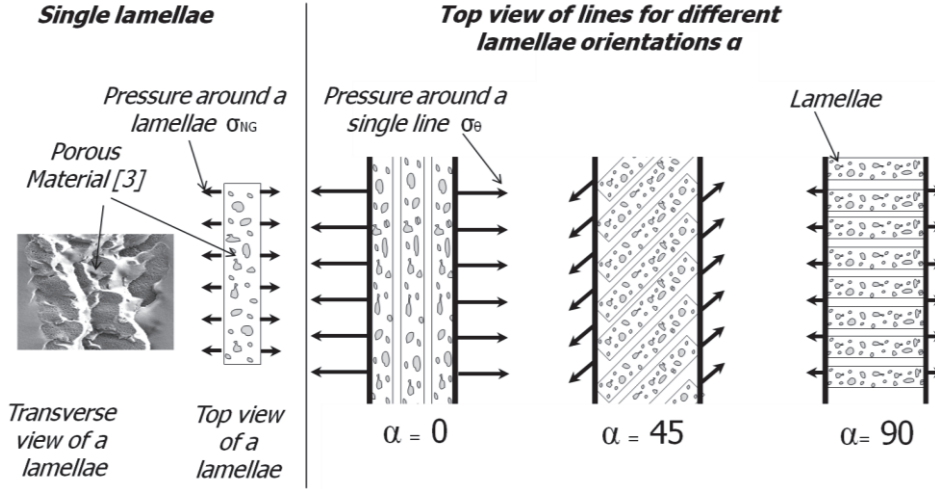
Fig. 36. Left: Transverse and top view of a single nanograting made of porous material [3] Right: Top view of three lines with different nanogratings orientation with respect to the writing direction and different σ_0. (α is the angle between the writing direction and nanogratings orientation).

3.   **Stress measurement in direct-write patterns**

a.   *Methodology*

Stress in a transparent material induces birefringence that in turn introduces retardance for the light passing through the specimen. This retardance can be measured and is directly related to the principal stress components according to Eq. (3.1):

$$\sigma_1 - \sigma_2 = \frac{R}{T(C_1 - C_2)} \tag{3.1}$$

where $C_1-C_2=C$ is the stress optic coefficient and is equal to 3.55×10^{-12} Pa^{-1} for fused silica at 546 nm. This coefficient is expressed by $C = (n^3/2) (\pi_{11} - \pi_{12})$ where π_{11} and π_{12} are the piezooptic constants for fused silica [4] and n is the refractive index. Since fused silica is isotropic, the tensor principal directions are considered collinear to the cylindrical coordinates. T is the thickness of the sample and R is the measured retardance.

High resolution retardance measurements in the immediate vicinity of a direct-written line are difficult to achieve due to the sharp intensity decay occurring over just a few micrometers [5]. To overcome this limitation, we enlarge the span of the stressed region using a dedicated laser-written pattern (shown in Fig. 37)

suggested in [6] that we use here for a different purpose than it was initially designed for. In this pattern, several lines, forming an edge, are written one on top of another along the z-axis, and through the entire thickness T of the specimen. Lines are spaced with a given z increment (here, ten microns to avoid overlapping). We consider the stress to be homogeneous in the z direction. These edges are radially and regularly distributed around a circle (Fig. 37 left). Later, we refer to this particular shape as the 'sun-pattern'.
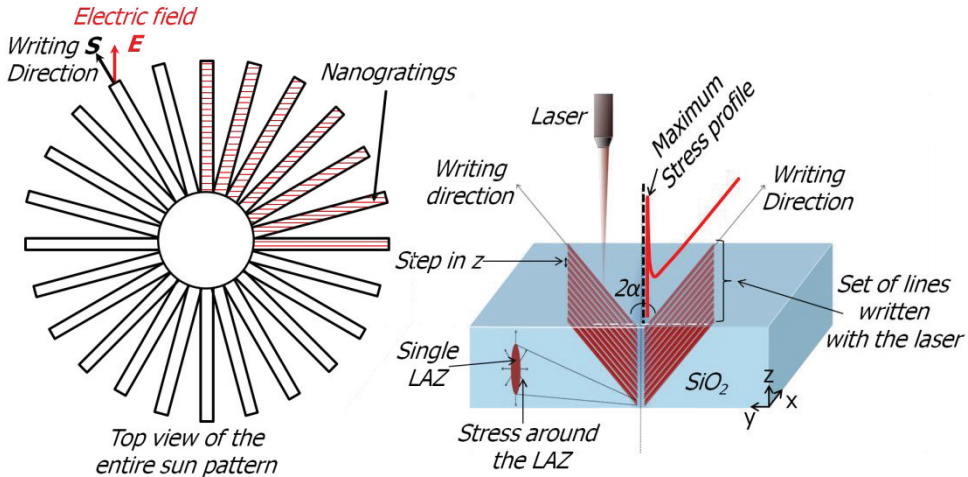
Fig. 37. Left: top view of the laser pattern used to investigate the dependence of the stress on nanogratings orientation, the 'sun-pattern'. The laser beam is linearly polarized and the polarization is kept the same for all writing directions. Right: close-up three-dimensional view of two segments of the laser-written pattern shown in the left figure. (LAZ) stands for laser-affected zones.

Nanogratings formed under linear polarization consist of a set of parallel planes with their normal vector collinear to the electrical field and perpendicular to the light propagation axis (k-vector). Consequently, in the case of the pattern above, if the polarization direction is set constant during the writing process (Fig. 37), each line of the radiating pattern will have a different nanogratings orientation with respect to the writing direction.

b. *Stress profile between lines: analytical model*

In the previous chapter, we have demonstrated that an expansion occurs in the laser-exposed areas causing stress around laser-affected zones. As a first order approximation in the case of the 'sun-pattern', this expansion can be described by a homogeneous load distribution applied on both sides of a wedge (illustrated in Fig. 38). The stress distribution in such case was derived analytically by C. J. Tranter [7] who considered a plane-strain problem. Here, we just recall the main

features of his model that we adapt to our particular case. In Tranter's model, the shear stress is assumed to be equal to zero.
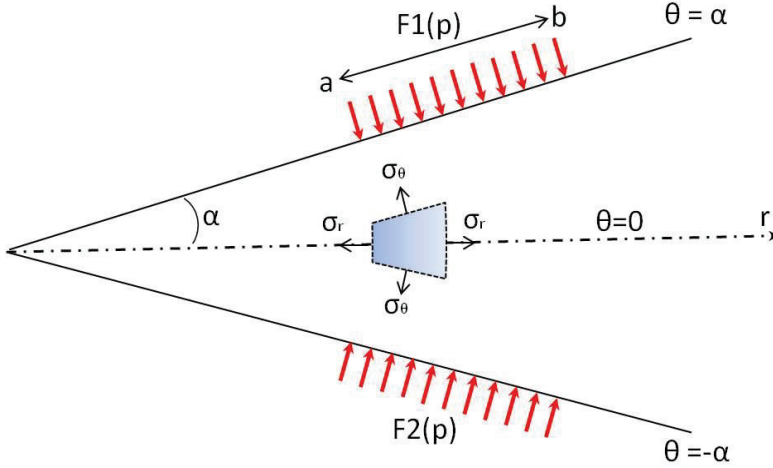
Fig. 38. Wedge model used for finding analytically the stress distribution in an angular section of the 'sun-pattern' of Fig. 37. To capture the stress resulting from the expansion of the laser-written lines, we consider a homogeneous force distribution (F1, F2) distributed along edges from a to b.

In Eqs. (3.2), the stresses, σ_θ and σ_r, are found using Mellin's inversion formula [7]:

$$\left.\begin{array}{l} \sigma_\theta = \dfrac{1}{2\pi i} \displaystyle\int_{c-i\infty}^{c+i\infty} p(p+1)\phi r^{-p-2} dp \\[4mm] \sigma_r = \dfrac{1}{2\pi i} \displaystyle\int_{c-i\infty}^{c+i\infty} \left[\dfrac{d^2\phi}{d\theta^2} - p\phi \right] r^{-p-2} dp \end{array}\right\} \tag{3.2}$$

where ϕ is the stress function, p a complex number, r, θ the cylindrical geometrical coordinates in Fig. 38. The edges are each subjected to an initial uniform pressure (F) from the section a-b of the profile. The principal stress difference in the cylindrical coordinate system is given by Eq. (3.3):

$$\sigma_\theta - \sigma_r = F(r) \left\{ \frac{2b}{r} \left[\frac{\sin(\alpha)\cos(\theta)}{2\alpha + \sin(2\alpha)} - \frac{1}{\pi} \int_0^\infty G(\xi) \sin\left\{ \xi \log\left(\frac{b}{r}\right) \right\} d\xi \right] \right.$$

$$\left. - \frac{2a}{r} \left[\frac{\sin(\alpha)\cos(\theta)}{2\alpha + \sin(2\alpha)} - \frac{1}{\pi} \int_0^\infty G(\xi) \sin\left\{ \xi \log\left(\frac{a}{r}\right) \right\} d\xi \right] \right\} \tag{3.3}$$

with:

$$G(\xi) = \frac{\sin(\alpha - \theta)\cosh(\alpha + \theta)\xi + \sin(\alpha + \theta)\cosh(\alpha - \theta)\xi}{\xi\sin(2\alpha) + \sinh(2\alpha\xi)} \qquad (3.4)$$

In our case, the angle between lines is set to $\theta = 2\alpha = 15°$. From [7] and integrating F over $r \in$ [a, b], the stress function ϕ is found. The integrals are solved between $\theta \in$]0, $\pi/2$[with the residue method for the real part of p, which is equal to -1.

The integral in Eq. (3.3) cannot be calculated analytically for $\theta \in$]0, $\pi/2$[. These two integrals, given below, are solved numerically for a particular angle:

$$\left. \begin{aligned} f_a(r,\theta,\alpha,a) &= \int_0^\infty G(\xi)\sin\left[\xi\log\left(\frac{a}{r}\right)\right]d\xi \\[2mm] f_b(r,\theta,\alpha,b) &= \int_0^\infty G(\xi)\sin\left[\xi\log\left(\frac{b}{r}\right)\right]d\xi \end{aligned} \right\} \qquad (3.5)$$

Finally, from Eqs (3.3)-(3.5) the difference of principal stress is expressed by Eq.(3 6):

$$F(r,\alpha) = \frac{\sigma_\theta - \sigma_r}{\kappa\left\{\dfrac{2b}{r}\left[\dfrac{\sin(\alpha)\cos(\theta)}{2\alpha + \sin(2\alpha)} - \dfrac{f_b}{\pi}\right] - \dfrac{2a}{r}\left[\dfrac{\sin(\alpha)\cos(\theta)}{2\alpha + \sin(2\alpha)} - \dfrac{f_a}{\pi}\right]\right\}} \qquad (3.6)$$

where, $f_a = f_b$ are numerical estimations of Eqs. (3.5) and are both equal to 0.78 for $\alpha = 15°$, a = 100 micrometers and b = 600 micrometers.

To take into account both the effect of the laser-written line width (which can be up to 2 micrometers depending on the exposure condition and which is therefore not negligible) and the 'bulk' nature of our pattern as opposed to a slice as in Tranter's model, we introduce a fitting factor, κ (here 14), that we estimated using finite element simulations.

c. *Stress profile between lines: finite element model (FEM)*

To test and refine the analytical method, we use a finite element model of the stress induced within the 'sun-pattern'. Here, we consider a plane-strain problem (i.e. the 'sun-pattern' is considered infinitely thick). Since the laser-affected zones expand [1], we apply a uniform pressure F (blue arrows in Fig. 39 left) around rectangles that are 2 µm-wide and 500 µm-long (i.e. the size of one laser-written line as measured with an optical microscope equipped with a 40x objective).
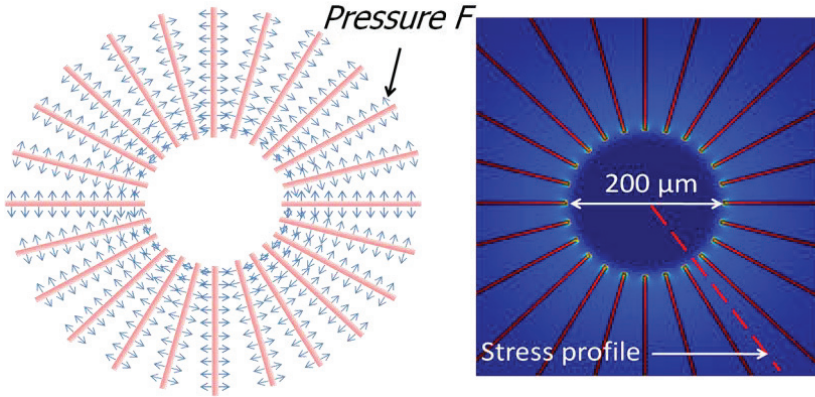
Fig. 39. Finite element simulation for the homogeneous case. (i.e without taking into account the nanogratings) Left: plane-strain problem definition and boundary conditions (pressures are indicated with blue arrows) and right, simulated stress for identical forces applied on each line. (Here, for the sake of clarity, the polarization state is assumed to be the same for each line.)

The initial pressure (F) is found by calibrating the finite element simulation so that the maximum stress measured between lines (and therefore the retardance, in Eq. (3.1) matches the experimentally measured ones (in paragraph 4.a). The relation between the maximum stress in between the lines and the initial pressure applied on the edges is linear.

In the following section, we will use both the analytical and the FEM model for finding the stress resulting from the expansion of the laser-written lines.

4. Experimental results

To write 'sun-patterns', fused silica substrates (Corning 7980 of UV grade, 2 x 2 cm square and 250 +/- 25 µm thick) are exposed to a femtosecond laser (fiber-amplifier from Amplitude Systèmes, Femtoprint model) emitting 275 nJ pulses at 1030 nm and at a repetition rate of 800 kHz. The pulse duration is 270 fs. The numerical aperture of the objective (OFR/Thorlabs 20X-1064 nm) used for focusing the laser beam is 0.4. The branches of the 'sun-pattern' are single lines stacked over the entire sample thickness (T = 250 µm). The energy deposition [8] is set by tuning the writing speed and the repetition rate. The retardance is measured with a commercial instrument (CRI-Polscope using a 10x objective).

a. *Stress measured around laser-affected zones*

We consider sun-pattern written with energy deposition level of 186 J/mm² (writing speed 1 mm/s). The polarization is kept constant. The measured stress (extracted

from the retardance data) is fitted with the FEM simulations by simply changing one parameter, the initial pressure F (in this case the pressure is the same around every line forming the sun), which defines the boundary condition. As seen in Fig. 40, the best fit is found for F = 65 +/- 5 MPa which gives a corresponding stress measured in the middle of two consecutive radiating lines with an accuracy of +/- 1 MPa. This accuracy matches the stress measurement error. The error in measuring the position of the written pattern (located at r = 110 μm +/- 1 μm), gives a maximum error of 0.8 MPa for the initial pressure. Fig. 40 right shows the measurement versus the analytical solution and the finite element simulation results. A reasonable match around the maximum is found for both the analytical and finite element models. While both models capture the stress decay with increasing r, the analytical solution is less accurate and overestimates the stress as r increases. The difference could be attributed to the geometry of the patterns. In the wedge case, the lines intersect, whereas for the measurement and simulation, the lines are distributed around a circle of 200 μm diameter. It nevertheless demonstrates that the profile birefringence effectively originates from the volume expansion of the laser-written lines and confirms our previous observations [1].
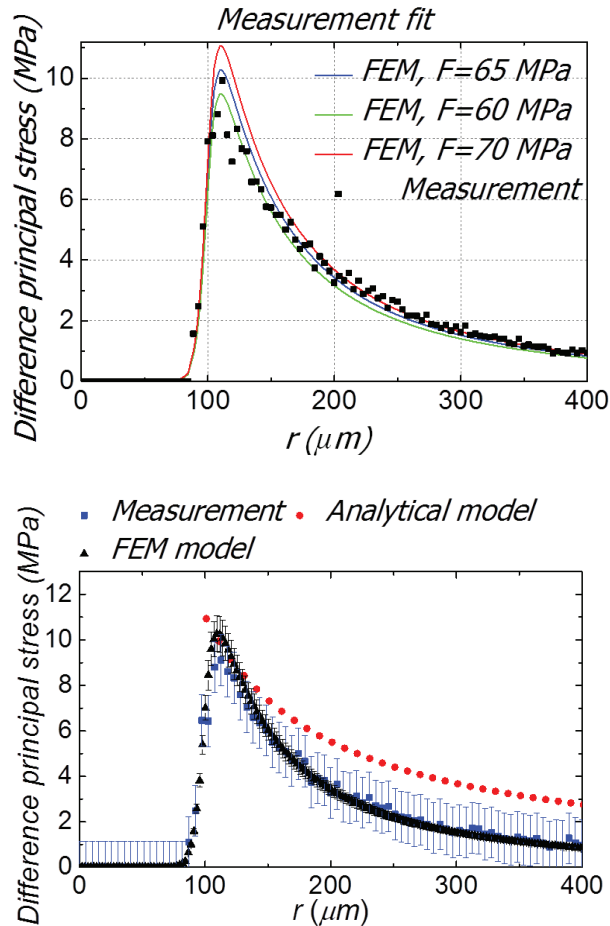
Fig. 40. Top: Measured principal stress difference profile between two laser written lines versus FEM simulations result to define a range of pressure, in which the maximum principal stress fits best – the value obtained is F=65 MPa. The measurement error bars are not shown on this graph for clarity but are shown on the bottom graph. Bottom: Comparison of analytical model, finite element model and measurement.

b. *Polarization effects on accumulated stress*

The 'sun-patterns' offer the opportunity to test the influence of the nanogratings orientation on the stress surrounding the laser-affected zones (Fig. 41). Nanogratings are oriented perpendicular to the electric field of the light [9,10]. Therefore, if the laser polarization is kept constant while writing the 'sun-pattern',

the nanogratings will gradually turn with respect to the writing direction for consecutive lines.
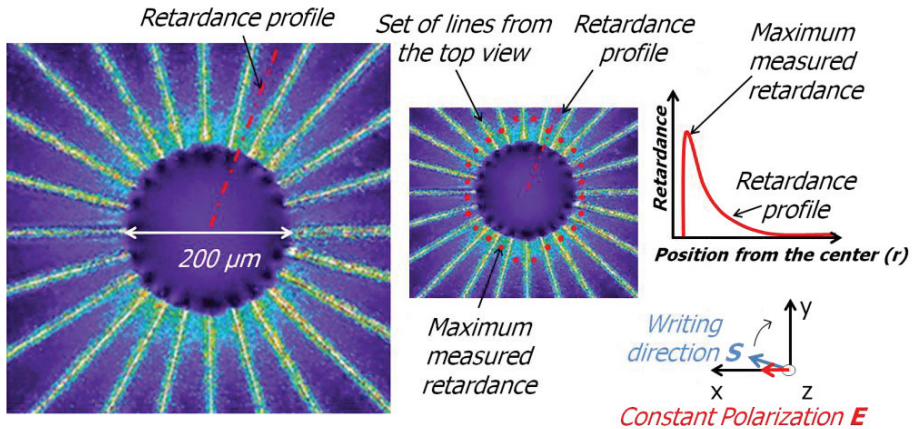
Fig. 41. Left: Effect of the polarization on the retardance distribution around the 'sun-pattern'. In this experiment, the polarization is kept unchanged while writing the lines at 1 mm/s. Right: the same image but this time with dots to help visualizing the maximum measured retardance as a function of the angle.

Fig. 41 clearly shows that the stress distribution amplitude depends on the nanogratings orientation. To model this orientation dependence, we use a multiscale approach (Fig. 42):

In a first step, called 'nanoscale model', we simulate the influence of nanogratings orientation along a single line, assuming that only the laser-affected part of the nanograting expands. The size and space are defined from SEM observation (from Fourier-transform of SEM images such as the one shown in Fig. 44, the nanogratings spatial period is estimated to be 275 nm +/- 5 nm, and the width of the nanogratings is 100 nm +/- 5 nm). Following our initial hypothesis, we assume that each lamella (red segment in Fig. 42) of nanogratings expands. As boundary condition, a homogeneous pressure, σ_{NG} is applied all over the lamellae (black arrows in Fig. 42 right). The shear, normal and transverse components of the stress tensor are simulated for every lamellae orientation. The resulting stress vector σ_R is used as input for the full-pattern simulation (step 2).

In a second step, called 'microscale model', we simulate the stress distribution between lines, for the full-pattern. In this description, lines are represented by a homogeneous rectangle of finite thickness. By calibrating the finite element model with the experimental observations reported in paragraph 3.a (for nanogratings oriented perpendicularly to the writing direction and speed at 1 mm/s), we found that the stress around a single lamella is 2 +/- 0.2 GPa. The complete simulation is performed between 0 deg and 90 deg with the angle

increasing in increments of 15 deg. Note that according to our study on the effect of deposited energy [1,8], the energy deposition considered here does not lead to the maximum etching rate. It is therefore foreseeable that the etching rate could be even higher in the optimal cases of energy deposition. Here, we focus on the role of nanogratings orientation on the stress distribution.

In Fig. 42 left, this methodology is described for three different line angles. The blue arrows represent σ_R. Applying this method to the full patterns gives the results shown in Fig. 42 right.

Step 1: *Nano-scale model (lamellas)*

Step 2: *Micro-scale model*

Full scale model (full pattern)

$\alpha = 0$

Line boundaries

$\alpha = 45$

$\alpha = 90$

Isostatic stress applied around each single lamellae (σ_{NG})

$\alpha = 90$

Equivalent stress around a single line $\boldsymbol{\sigma_R}$

$\alpha = 45$

$\alpha = 0$

(*s* is the writing direction, *E* is the direction of the electrostatic vector, *n* the normal to the laser affected zones and *k* the wave vector)
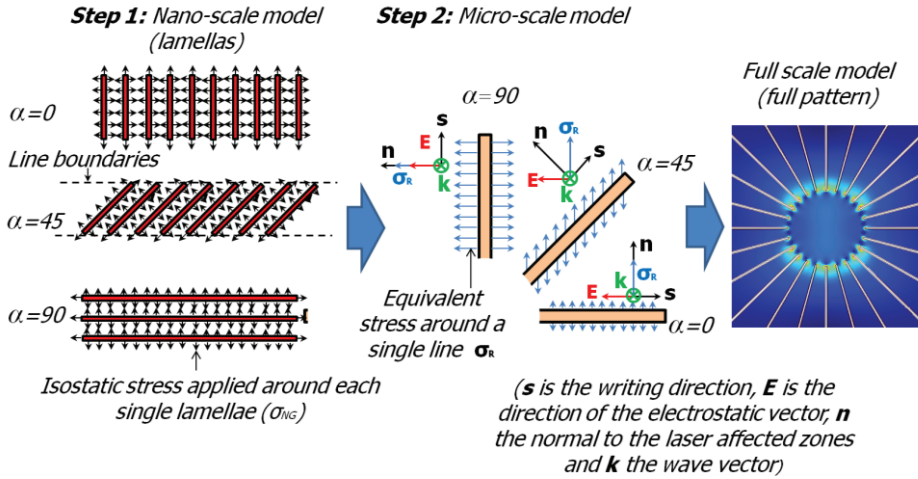
Fig. 42. Multi-scale approach for investigating the effect of nanogratings orientation on stress distribution. Step 1 – 'nanoscale description', a uniform pressure σ_{NG} (black arrows) is applied around a single lamellae (red segment) that constitutes the nanogratings for different lamellae orientation. Step 2 – 'microscale description', the resulting principal stress σ_R (blue arrows) is applied on the equivalent rectangles, representing the nanogratings. This technique is then applied to the full patterns as can be seen on Fig. 42 right.

Fig. 43 shows the measured maximum difference of principal stress (σ_m) (the difference between the first principal stress and the second principal stress from the stress tensor) depending on the line angles α, for a particular set of exposure conditions (writing speed of 1 mm/s and energy deposited of 186 +/- 2 J/mm^2). A periodic distribution of stress is observed for both measurement and simulations. We simulated the stress for different spaces between lamellae (250, 300, 350 nm) because the width of a single lamella, in reality, is not constant in the z direction (since it is elliptical). In this case the maximum width variation is +/- 50 nm (One lamella is about 100 nm in width). The graph shows that the width of the lamellae does not dramatically change the trend and amplitude of the stress in between lines. This result confirms the validity of our model and it

confirms that the nanogratings orientation influences the stress distribution. Since all other parameters were fixed, the observed variation is attributed to the nanogratings orientation.
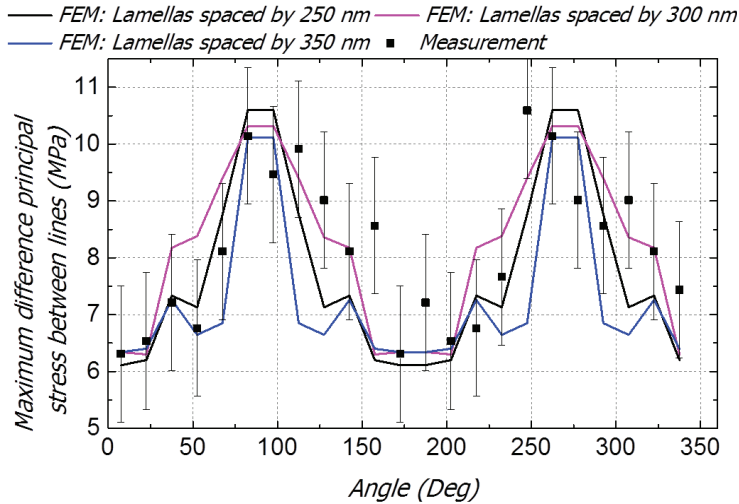
Fig. 43. Pink, blue and black lines represent the simulated retardance and black squares the measured one. The lines connecting simulation data-points are just added to help visualizing the distribution of data point. We clearly see two maxima and two minima according to the angle.

This result shows that the nanogratings orientation and therefore the laser polarization has a non-negligible influence in the stress induced in the material. The maximum simulated stress (σ_{m}), on the profile between lines can vary as much as 30 to 50% depending on the orientation. The corresponding refractive index change ($n_\perp$ - $n_{//}$) resulting from stress induced birefringence around laser-affected zones varies within the range of 2.1×10^{-5} to 3.5×10^{-5} for the experimental conditions of Fig. 42. This model further estimates that the stress around individual lamellae can be in the order of several GPa. Such a high stress may locally create the conditions for crack nucleation and the collapse of the nanogratings structure resulting in stress relaxation phenomena, as suggested in [6,8]. Note that the occurrence of cracks inside nanogratings lamellae, were observed experimentally in [11]. It may also induce localized densification as well as the formation of high pressure phases, possibly surrounding the pores forming inside lamellas and causing the localized volume expansion.

5.   Structural modifications and laser parameters

To further test this hypothesis of stress relaxation, we investigate the morphology of nanogratings for energy deposition levels ranging from 16 J/mm^2 to 240 J/mm^2

and for two polarizations, namely (nanogratings perpendicular to the trench and then parallel to the trench). The cantilever method described in [1], is used to identify the levels of stress and energy deposition at which relaxation occurs for both polarizations. Here, we examine the morphology of the lines for the chosen laser parameters (Fig. 44). In practice, several trenches at different energy depositions are written in a fused silica substrate. A solution of heated potassium hydroxide (KOH) (1 M concentration at 80 ^{0}C, 3 h) is used to reveal the nanogratings [12].
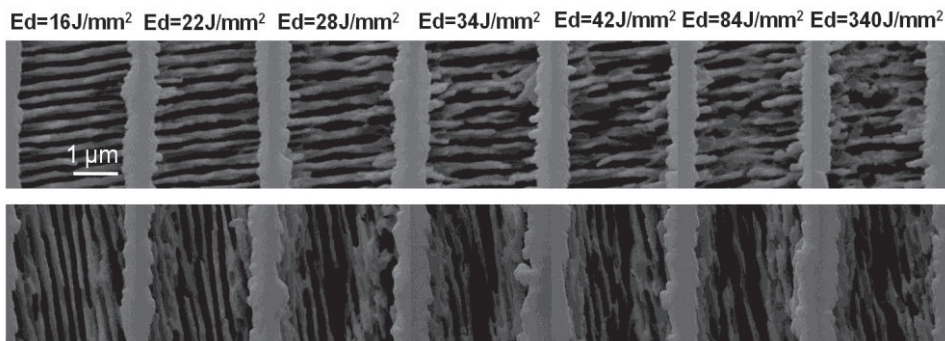
Fig. 44. Scanning Electron Microscope images of the nanogratings according to the energy deposition. The periodicity is about 275 +/- 5 nm and the size of the features is 100 +/- 5 nm.

The nanogratings' periodicity is about 275 nm (+/- 5 nm). Their sizes and period do not seem to change with the energy deposition level, but their morphology do. The nanogratings regularity starts to gradually degrade for higher energy deposition (between 22 J/mm^2 and 28 J/mm^2 for transverse to the writing direction polarization, and between 28 J/mm^2 and 34 J/mm^2 for the longitudinal to the writing direction polarization) and finally becomes disorganized as the deposited energy increases further.

This result supports a model where the stress gradually increases inside nanogratings lamellae, eventually causing their collapse and the degradation of the nanogratings homogeneity.

6.   Conclusion

Using a method based on retardance measurement, we have demonstrated that nanogratings orientation influences the stress distribution induced in the material. To explain this phenomenon, we introduce a multiscale model that considers the local expansion of individual lamellae that constitutes the nanogratings. As the deposited energy increases, pores are formed (possibly as a consequence of the decomposition of SiO_2 [3]) and cause the expansion of the lamellae volume which further results in localized stress generation and eventually the collapse of the

nanograting structures when the stress becomes too high. We have shown that indeed, such a collapsing of the nanogratings is observed as the energy deposited is increased. According to our model, the stress in between lamellae of nanogratings could reach a few GPa, which could lead to localized silica polymorphic-phase formation.

Here, the proposed method to quantify the stress around the laser-affected zone is faster than the cantilever method and simulations shown that the stress surrounding the nanogratings could reach GPa order.

It has been observed that the stress surrounding the laser-affected zone influences the etching rate [13]. In the second chapter, the correlation between cantilever experiment (stress with respect to the energy deposition) and etching rate as a function of the energy deposition as well, in both regimes suggest a dependence of the etching rate on the stress in the laser-affected zone as well. As a result, we propose in the next chapter to measure the etching rate of fused silica subjected to various stresses in order to verify previous hypothesis.

7.   References and Links

1. A. Champion and Y. Bellouard, "Direct volume variation measurements in fused silica specimens exposed to femtosecond laser," Opt. Mater. Express **2**, 789-798 (2012).
2. M. Gecevičius, M. Beresna, J. Zhang, W. Yang, H. Takebe, and P. G. Kazansky, "Extraordinary anisotropy of ultrafast laser writing in glass," Opt. Express **21**, 3959-3968 (2013).
3. J. Canning, M. Lancry, K. Cook, A. Weickman, F. Brisset, and B. Poumellec, "Anatomy of a femtosecond laser processed silica waveguide [Invited]," Opt. Mater. Express **1**, 998 (2011).
4. T. N. Vasudevan and R. S. Krishnan, "Dispersion of the stress-optic coefficient in glasses," J. Phys. D: Appl. Phys. **5**, 2283 (1972).
5. Y. Bellouard, T. Colomb, C. Depeursinge, M. Dugan, A. Said, and P. Bado, "Nanoindentation and birefringence measurements on fused silica specimen exposed to low-energy femtosecond pulses," Opt. Express **14**, 8360-8366 (2006).
6. C. Corbari, A. Champion, M. Gecevičius, M. Beresna, Y. Bellouard, and P. G. Kazansky, "Femtosecond versus picosecond laser machining of nano-gratings and micro-channels in silica glass," Opt. Express **21**, 3946-3958 (2013).
7. C. J. Tranter, "The use of the Mellin transform in finding the stress distribution in an infinite wedge," Q J Mechanics Appl. Math. **1**, 125–130 (1948).
8. S. Rajesh and Y. Bellouard, "Towards fast femtosecond laser micromachining of fused silica: The effect of deposited energy," Opt. Express **18**, 21490-21497 (2010).
9. Y. Shimotsuma, P. G. Kazansky, J. R. Qiu, and K. Hirao, "Self-organized nanogratings in glass irradiated by ultrashort light pulses," Phys Rev. Lett. **91**, 247705 (2003).
10. V. R. Bhardwaj, E. Simova, P. P. Rajeev, C. Hnatovsky, R. S. Taylor, D. M. Rayner, and P. B. Corkum, "Optically produced arrays of planar nanostructures inside fused silica", Phys. Rev. Lett. **96**, 057404-1(2006).

11. Y. Bellouard , E. Barthel, A. A. Said, M. Dugan, and P. Bado, "Scanning thermal microscopy and Raman analysis of bulk fused silica exposed to low energy femtosecond laser pulses," Opt. Express 16, 19520-19534 (2008).

12. S. Kiyama, S. Matsuo, S. Hashimoto, and Y. Morihira, "Examination of etching agent and etching mechanism on femotosecond laser microfabrication of channels inside vitreous silica substrates†," J. Phys. Chem. C **113**, 11560–11566 (2009).

13. A. Agarwal and M. Tomozawa, "Correlation of silica glass properties with the infrared spectra," J. Non-Cryst. Solids **209**, 166-174 (1997).

Chapter IV. On the relation between stress and hydrofluoric-acid etching rate in fused silica

In this chapter, the influence of the mechanically induced stress in fused silica on the etching rate is investigated under compressive and tensile stress. The objective is to be able to evaluate the pure stress contribution to the etching rate enhancement phenomena observed after laser exposure by decoupling stress from laser-affected zones that also contain photomodified materail. To do so, we have developped a mechanism allowing loading micro-beams in tensile and compressive stress up to 1 GPa. Two etching rate measurement methods are then proposed to quantify the pure stress contribution to etching rate enhancement.

1. Introduction

In the previous chapters, we have demonstrated that laser-induced modifications in fused silica substrates eventually lead to significant stress build-up in the material. This stress can be controlled, since it is strongly correlated to laser exposure parameters such as energy deposition, polarization or energy per pulse. Furthermore, as mentioned in chapter II, there seems to exist a correlation between etching rate and stress. This observation is based on the similitude of behavior between stress build-up and etching rate with the laser energy deposited: i.e. first, a sharp increase followed by a kind of exponential decay.

So far, the effect of laser-induced stress on etching rate has not been thoroughly investigated. In [1] an enhancement of the etching rate (cone formation at the entrance of a micro-channel) has been observed outside the laser-affected zone, but near the laser-exposed zones (where stress is non negligible). The existence of these cones can be attributed either to clipping of the laser beam when crossing the substrate edge and/or to the presence of stress. In [2] the distortion of a rectangular laser-written pattern at the edges was reported after etching. In this particular case the etchant seems to follow the iso-stress contours as shown in Fig. 45.
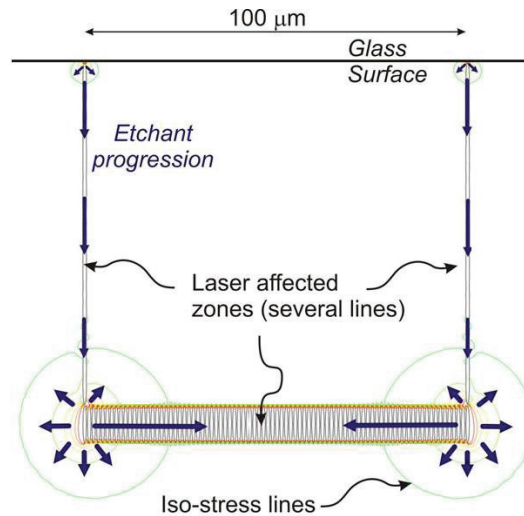
Fig. 45. Etchant progression in a square inscribed with femtosecond laser in fused silica. The blue arrows represent the etchant progression along the affected zones. At the corner the etchant direction follows higher stress concentration (green lines) from [2].

The influence of stress on the etching rate of a fused silica film thermally-grown on a silicon substrate has been reported in [3] but only small range of stress was investigated (up to 400 MPa) and in high Hydrofluoric acid (HF)

concentration, which are not typically used for micromachining, since low concentrations (2.5 to 5%) are suitable to avoid damaging the surface of the sample. Nevertheless, the work [3] clearly shows that stress has a direct effect on the etching rate.

In this chapter, we systematically investigate the role of stress on the etching rate in order to understand the cause of the etching rate enhancement observed after femtosecond laser exposure. The underlying question is to determine the role of the photochemical modifications induced in the material compared to the role of the stress induced by the volume expansion on the etching rate enhancement. It is clear that both effects – photochemical transformation and stress near laser-affected zones are spatially coupled. Therefore, to answer the question formulated above, we need to separate both effects. To do so, we propose a prefabricated device made in fused silica where stress up to 1 GPa can be applied. Compressive and tensile stresses are both investigated. This work is not only important for understanding the physical mechanism of the etching enhancement but also for optimizing the micromachining process.

2.   **Experimental setup**

a.   *Working principle of the device*

In this section we describe a device allowing loading uniformly glass beams under compressive and tensile stress, using the expansion induced by the laser exposure including a mechanism to measure displacement in the beams and then calculate the stress in the beams.

- *Compressive stress:*

The device consists of three parts, the loading part, the guidance part and the lever amplification mechanism part see Fig. 46:

The loading part is the beam 1. A part of this beam is expanded with the laser in making lines back and forth through the entire thickness of the beam and along itself, red area in the Fig. 46 top-left (This step is more detailed in the next section). Beams 1 and 2 are built-in in a stationary frame at one of their extremities and connected to each other so that when the beam 1 expends, a displacement occurs and compresses the connected beam 2.

A mechanical guidance is needed to obtain a uniform loading and to prevent the test beam to collapse. To do so, two thin beams are attached at each side of the moving part and attached at their others extremities to the fixed part as shown in Fig. 46 top-left. This allows a rectilinear movement of the moving part, albeit with a non-linear stiffness. However, the displacements are small and the guidance is essentially used in its quasi-linear range.

To estimate the stress in the beam, we measure the displacement induced by the stressors (area in red in Fig. 46) using a lever amplification mechanism

since the displacements are small (micrometer order) in the beam 1 and therefore difficult to measure. A transverse beam is attached to the moving part of the system (beam with stressor). This mechanism pivots around the intersection point of the oblique axis defining the orientation of two supporting beams that forms a hinge. As a pivot, it amplifies the displacement in the beam by converting the linear motion into an angular one. In Fig. 46 top, a 3D-rendering of the mechanisms for tensile and compressive stress generation are shown.

- *Tensile stress:*

The device consists of two parts, the loading part and the mechanism.

The loading part consists of 3 beams. All the beams are built-in in the frame. The expanded beams 1 and 2 with the laser red areas in Fig. 46 top-right (as in the compressive case), lead to a displacement of the beams 3 and 4 as shown in Fig. 46 top-right. Therefore the beam 4 is under tensile stress since it is built-in at his extremity to the stationary frame.

The lever amplification mechanism used for the tensile stress is the same as described above.
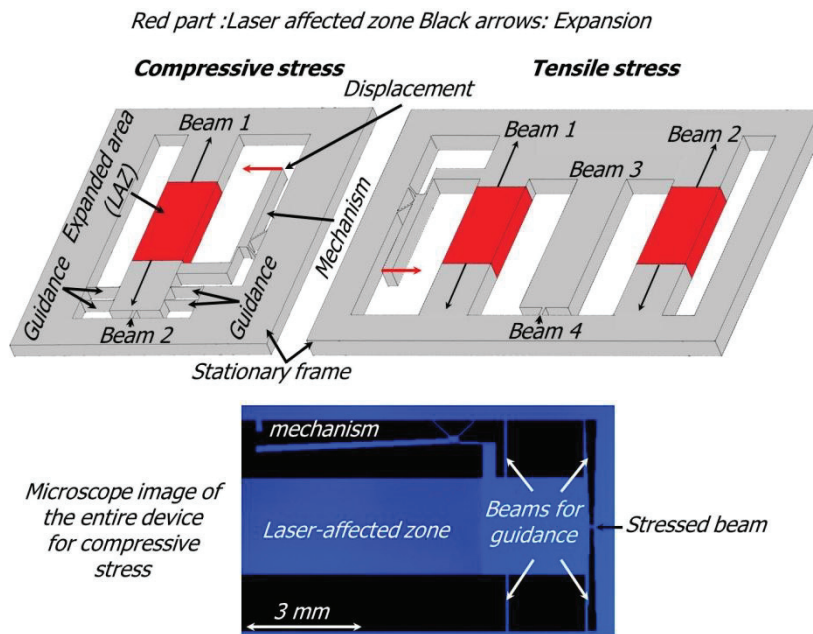
Fig. 46. Top: Schematics of the mechanism. Left: mechanism for generating compressive stress and right: mechanism for inducing tensile stress. Bottom: optical microscope image of the mechanism, beam and laser-affected zone.

Note that the 3D view does not show the real proportions of the device. Nevertheless we used this representation to better visualize the entire mechanism working principle. In the Fig. 46 bottom, optical image of the mechanism, the stressed beam and laser-affected zone are shown. This shows the real dimensions of the device.

b. *Device fabrication*

Using the laser described in chapter II, we fabricate the device to load the glass beams. The device is operated in four steps, depicted in Fig. 47.

1/ First, the entire device is inscribed with the laser, in a silica substrate 25 x 25 mm square and 500 µm thick.

2/ After exposure, the sample is immersed in Hydrofluoric acid at 2.5 % concentration during 12 h to reveal the structures.

3/ The upper part of the large beam is exposed to the laser again. A set of parallel lines is written, along a few mm and through the entire thickness of the sample (but not on the surface), to induce stress (see Fig. 47) based on the controlled laser volume expansion. To change the amount of stress in the small beam, we change the size of the laser-affected zone in the large beam by tuning the number of laser-written lines. (see Fig. 47)

4/ Finally, the sample is partially immersed in HF at 2.5 % concentration to preserve the stressors (made of laser-affected zones).
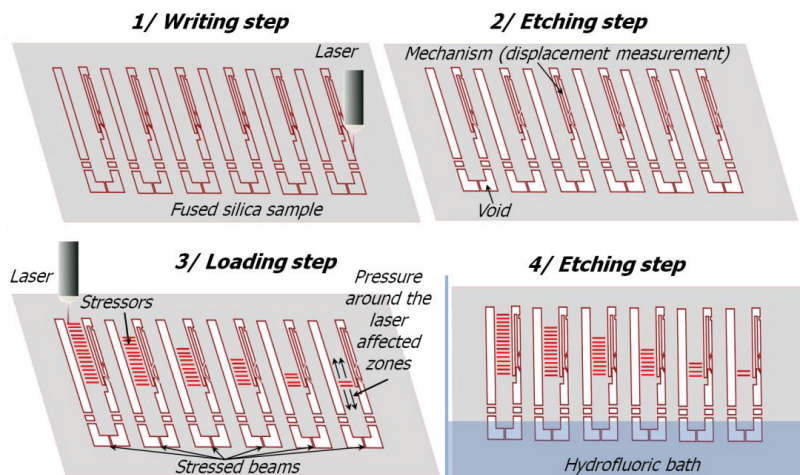
Fig. 47. Test specimen fabrication and loading principle. Step 1 laser exposure to fabricate the device, Step 2 etching process to reveal the structure. Step 3 loading process, several lines are written in the first beam to compress the second beam. Step 4 etching rate measurements according to the pressure in beams.

If the stress plays a role in the etching rate, we expect to observe topographical differences between stressed and non-stressed parts after etching.

   c. *Beam dimensioning problem statement.*

The basic concept is to use one beam that sees its volume expanding after being exposed to the laser beam to load another beam. In Fig. 48, a schematic shows two beams with different cross-sections connected one to another. The one with the largest cross-section is used to load the thinner second beam with a known stress level. The problem statement is to determine the maximum allowable stress level as a function of the number of laser-written planes to apply without inducing buckling of the test beam to be etched.
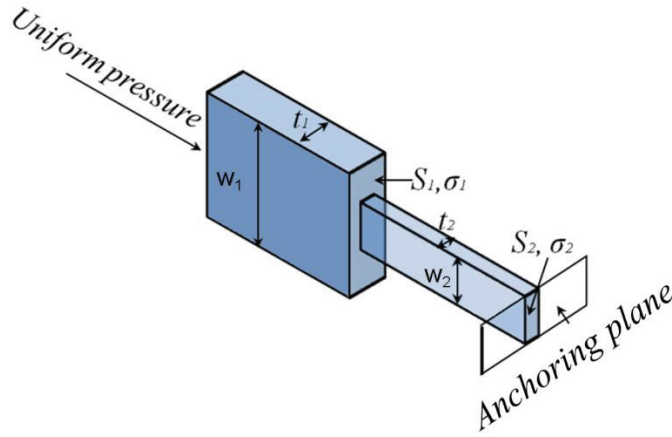
Fig. 48. Schematic of the beams. We need to dimension beam 1 and 2 to avoid buckling and optimize the applied stress.

The ratio of the stress applied to the beams is simply expressed according to the beam dimensions as follows:

$$\frac{\sigma_1}{\sigma_2} = \frac{S_2}{S_1} = \frac{w_2 t_2}{w_1 t_1} \tag{4.1}$$

where S_1, S_2, w_1, w_2 and t_1, t_2 are the cross-sections, the thicknesses and the widths, of beam 1 and 2, respectively. The stress buckling condition, σ_b, is expressed by:

$$\sigma_{2b} S_2 = F = \pi^2 E \frac{I}{L_k^2} \quad \text{with } I = \frac{w_2 t_2^3}{12} \tag{4.2}$$

where, I is the second moment of inertia and L_k the half-beam length. In our case, the out-of-plane thicknesses of the two beams are equal (since they are fabricated

in the same substrate). We further rewrite this expression in term of dimensionless ratios:

$$\sigma_{2b} = \frac{\pi^2 E}{12} \gamma^2 \qquad with \; \gamma = \frac{t_2}{L_k} \qquad\qquad (4.3)$$

$$\sigma_1 = \sigma_1^l = \frac{t_2}{t_1} \sigma_{2m} \;\; and \;\; \beta = \frac{t_2}{t_1} \qquad\qquad (4.4)$$

where σ_{2b} is the maximum allowed stress in beam 2 corresponding to the limit stress that would induce buckling of beam 1. These two simple equations allow us to fully define the two beam dimension requirements. Using the same laser condition as in [4] to create our stressors, the size of the exposed zone (the number of lines), is calculated from 0.03 % deformation so that it is never higher than the limit σ_1. As a first parameter selection, from these calculations, the width of beam 2, the maximum length of the first beam, and the width of the first beam are chosen to be 30 µm, 1.5 cm and 3 mm, respectively. In our case the thickness $w_1 = w_2 = 480$ µm.

3.   **Measurements**

a.   *Stress measurement*

The stress in the beam is measured with two methods:

The mechanism described in section (2.a) allows measuring the amplified displacement in the beam and to calculate the corresponding stress. The amplification is found to be 53 from a simulation performed with COMSOL software.

Using a dedicated microscope (PolScope) that measures retardance levels, the stress is calculated using photoelasticity [5]:

$$\sigma_1 - \sigma_2 = \frac{R}{T(C_1 - C_2)} \qquad\qquad (4.5)$$

where C_1-C_2=C is the stress optic coefficient and is equal to 3.55×10^{-12} Pa^{-1} for fused silica at 546 nm. This coefficient is expressed by $C = (n^3/2) (\pi_{11} - \pi_{12})$ where π_{11} and π_{12} are the piezo-optic constants for fused silica [5] and n is the refractive index at 546 nm. T is the thickness of the sample and R is the measured retardance.

As we used an instrument operating at 546 nm wavelength, the retardance measurement is bounded between 0 and 273 nm. At higher retardance levels, higher orders consisting of fringes are observed (see an example in Fig. 51). To

calculate the final retardance R_f, taken into account the higher orders, we used the following equation:

$$R_f = R_m + k\lambda \qquad (4.6)$$

where R_f is the final retardance, R_m the retardance measured in the beam after the last order, k the number of order and λ the wavelength at which the Polscope operates. In Fig. 49, the graph shows the comparison between photoelastic measurements and measurements from the mechanisms lever.
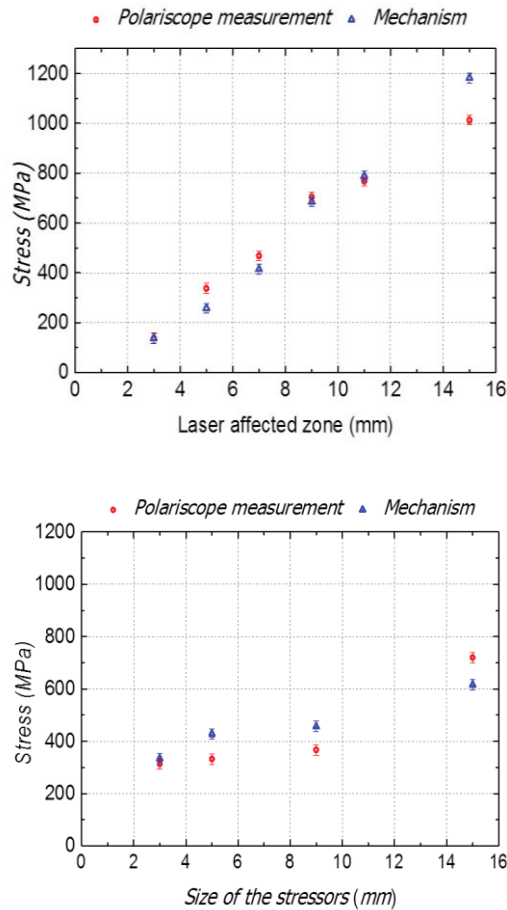
Fig. 49. Top: Comparison between photoelastic measurement and the mechanism lever in the compressive case. Bottom: Same comparison in the tensile case.

Although some minor (max 20 or 15 %) differences between the results of both methods exist, overall the results are consistent.

b. *Etching rate measurements: first method*

To see if the etching rate is enhanced by the stress in the beams described above we measure the topography along the beams (in Y direction in Fig. 50 top), for 6 different compressive stresses and 4 different tensile stresses and after 30 min etching. The topographic profiles are measured using a digital holographic microscope (DHM) equipped with a 10 x objective in reflection. In Fig. 50 bottom-left an example of topography profiles for beam under tensile stress (704 MPa) at 0 min etching duration and after 30 min etching is shown. In the bottom-right of the figure, the same profiles are plotted for compressive stress (334 MPa).

We clearly see a difference in height profile between two consecutive measurements that is attributed to an etching rate enhancement since all the measured area has been exposed to the HF (beams were entire immersed in the bath). Indeed if only the natural etching rate (1 µm/h) was involved, we would not be able to see any differences between the profiles.

Otherwise bulge and shrink effects are clearly visible for compressive stress and tensile stress respectively. Indeed when a beam is subjected to a compressive stress applied at its extremities, bulge and shrink forms. They are proportional to the pressure σ, to the Poisson ratio of the material ν and to the thickness of the beam (L). It can be expressed as follows:

$$B = \frac{\nu \sigma L}{2E} \qquad (4.7)$$

where, E is the Young modulus for fused silica. We divided by a factor 2 the formula because we measure the bulge only on the top of the beam. In this case it is equal to 422 nm for the highest stress. The pressure in the beam slightly varies (a few MPa), between two consecutive measurements and the corresponding bulge or shrink variation is a few nanometers, we added this effect to our topography measurement.
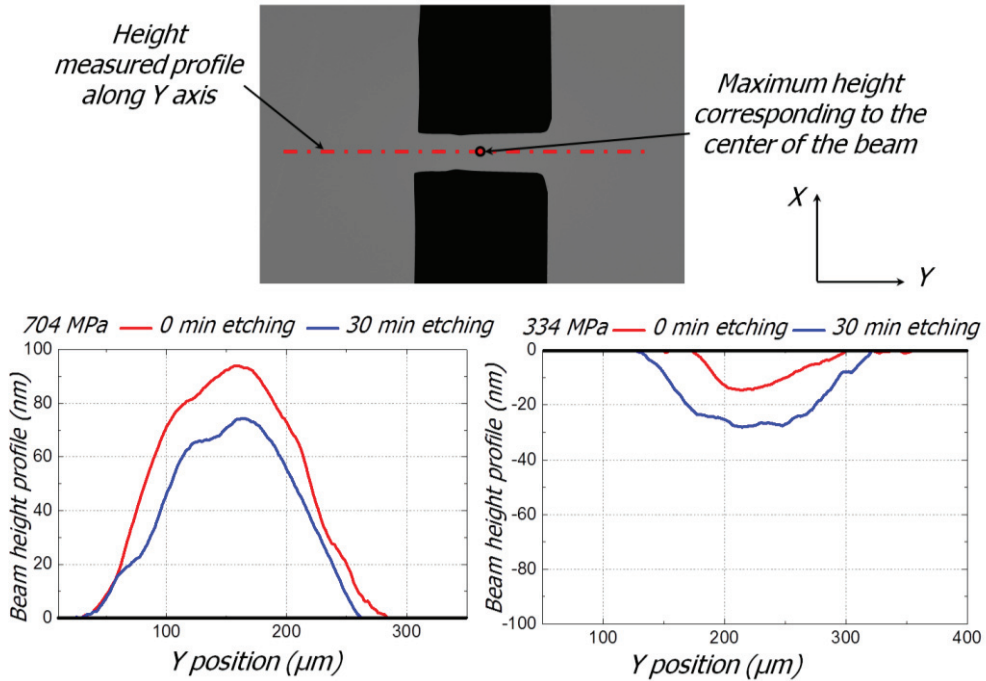
Fig. 50. Top: DHM image of a beam and topographic profile along the beam (*Y* axis). Bottom-left: Height profile image for 0 min and 30 min etching in the beam where 704 MPa is applied. Bottom-right: Height profile image for 0 min and 30 min etching in the beam where 334 MPa is applied

The maximum stress is measured for every beam in its center and the maximum removed material is extracted from the maximum height profile (represented in Fig. 50) before and after etching. From the differences of the height and etching duration, we obtain a variation of the etching rate between two consecutive measurements since the entire measured area was in the HF bath. Therefore to obtain the etching rate we need to add the natural etching rate which is 1 µm/h.

An example of a stress map is shown in Fig. 51 left. We notice that the stress never reaches 0 Pa along the profile in *Y* direction. Therefore, since the etching rate increase with the stress level, the minimum measured heights in the profiles above (Fig. 50) do not correspond to the height of the non-stressed part. Therefore, if we use only this profile, we underestimate the etching rate. As a result we need to measure height in the non-stressed part.

The maximum height measurement in the beam is performed in two steps from gray level pictures of the topography of the beam. At first a height profile is measured along *X* axis, as shown in Fig. 51 right, where zero stress level is

reached (see the map stress level in Fig. 51 left). Then a second height profile is taken along the *Y* axis in Fig. 51 right, where stress reaches the maximum stress in the beam (see the point 1 in the left figure). The difference M1 of the height between the points 1 and point 2 is measured. Point 1 corresponds to the height where the stress is the highest, in the middle of the beam. Point 2 corresponds to the height at the intersection of both profiles (red and blue in Fig. 51). Then the difference M2 of height between the points 2 and 3 is measured as well. Point 3 corresponds to the height where the stress equals zero.

The total height corresponding to the difference of the maximum height in the center of the beam and the minimum height in non-stressed area is obtained in adding M1 and M2.

We measure these heights before and after etching to calculate the etching rate (as described above) for every beams and plot the etching rate according to the maximum measured stress in the center of the corresponding beams. The graph is displayed in Fig. 53.

Measured height profile and retardance after 30 min etching
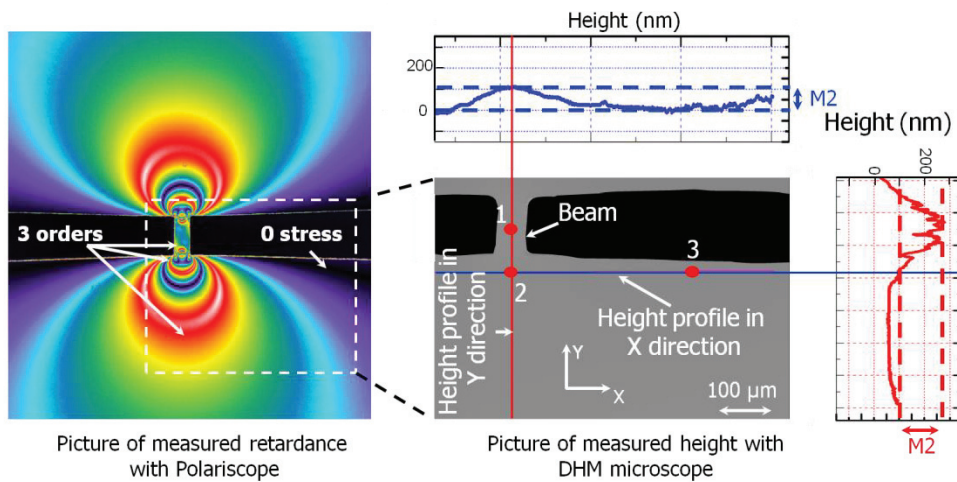
Fig. 51. Left: Stress measurement using photoelasticity (Polscope instrument). Left: Digital Holographic Microscope measurement of the beam surface and extracted height profile.

This first method based on Digital Holographic Microscopy requires one beam per measurement which is not convenient. We propose a second method to measure various etching rates using a stress gradient. This method is faster and allows verifying the results from the first method.

c. *Etching rate measurements: second method*

We use white light interferometry (Sensofar instrument) to accurately extract the topography of the beam after etching. The specimen tilt can be adjusted so that single interference orders are visible.

From one of the previous beams where the maximum pressure was 745 MPa in the middle (the beam where the highest stress was measured was broken), we take three images in gray levels as shown in Fig. 52 (bottom). The first one is the simulated profile (without etching), the second one is the actual measured profile after 109 min etching and finally, the third one is the pressure profile measured using photoleasticity.

In Fig. 52, on the top-left, a three-dimensional view of the simulated topography of the beam is shown.

After etching, we measure the topography of the beam. A three-dimensional view is shown in the top-right of the Fig. 52. Note that the loading is uniform.
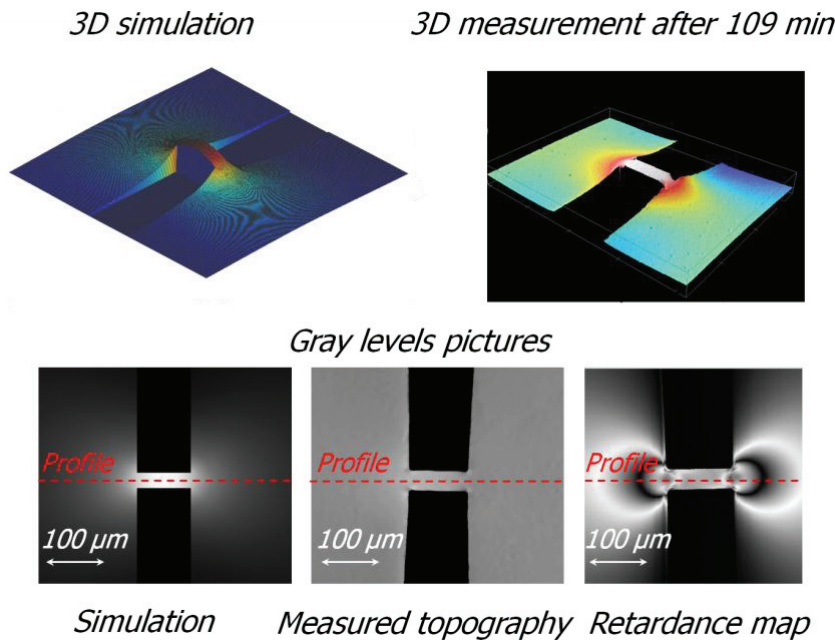
Fig. 52. Measurement steps for etching rate. Top-Left: Simulated beam. Top-Right measured beam after etiching. Bottom-Left: Gray level image of the simulated topography without etching. Middle: Gray level image of the measured topography after 109 min etching. Bottom-Right: Gray level image of the measured retardance of the beam after 109 min etching.

From each grey level image, we extract a profile exactly in the middle of the beam, as shown in Fig. 52. We subtract the simulated profile (which corresponds to the topography before etching) with the measured profile (after 109 min etching) to obtain the removed height along the beam. Then the etching rate is calculated all along the profile. The corresponding stress profile (right in the Fig. 52) is used to plot in Fig. 53 the graph of the etching rate according to the gradient of the pressure along the beam. In the Fig. 52 bottom, the three profiles are shown. With this method the etching rate can be measured for various pressures with a single beam, since a stress gradient appears from the center of the beam to its extremity.

4.   **Results and discussion**

In Fig. 53, etching rate according to the measured stresses in the beam is plotted for both methods and both types of stress. We clearly see that the etching rate increases with the pressure. The stress increase is thought to be correlated with Si-O-Si bond angle decrease when fused silica is subjected to stress [6]. In the case of an amorphous material, the bond angle decrease should not depend on the direction of the stress. Since the stress increases, the etching rate increases in a non-negligible way (almost 2 times the natural etching rate for the maximum that we were able to measure). The type of stress does not change the average enhanced etching rate. However, the stress levels tested here are not sufficient to explain the etching rate enhancement factor after laser exposure which is an order of magnitude higher (typically a factor above 60).
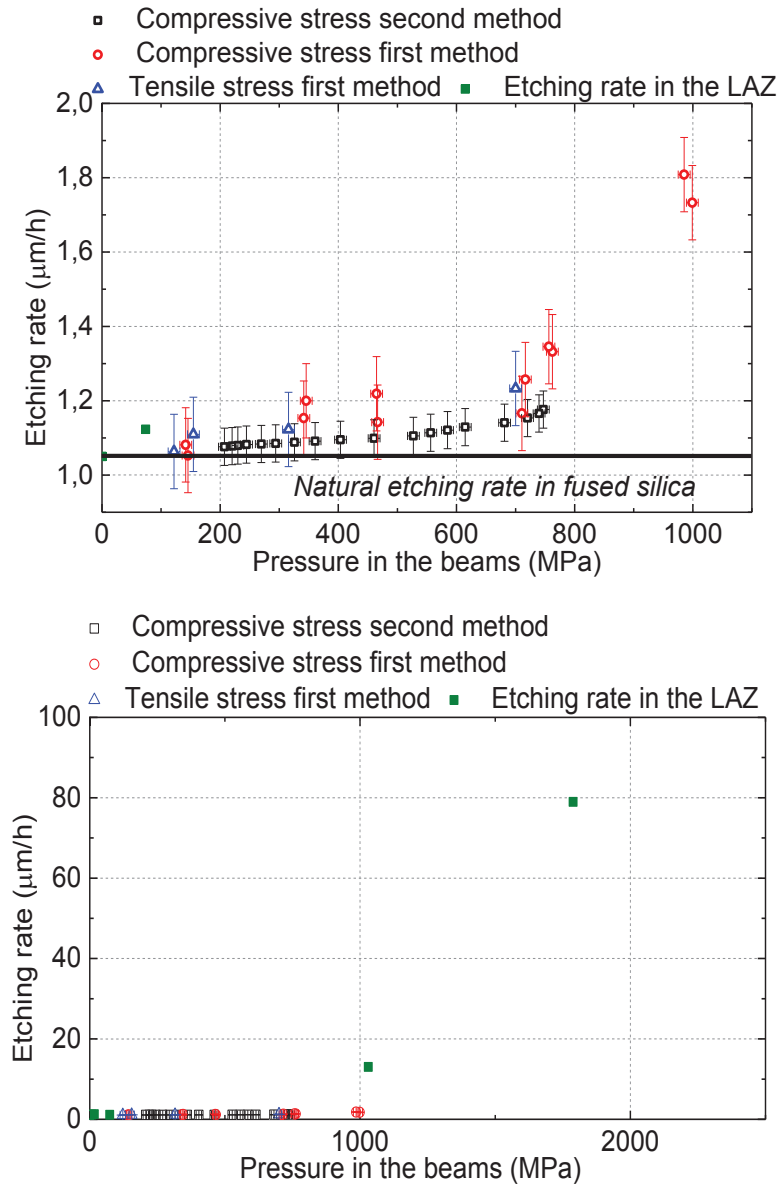
Fig. 53. Etching rate vs pressure along a beam subjected to 745 MPa. In the upper graph a zoom of the graph at the bottom is shown. The trend seems to be exponential which suggests that the etching rate is mainly driven by stress.

Thanks to the nanogratings model in [7] we calculated an equivalent stress between nanogratings lamellas (see chapter III) for different laser parameters and plot the corresponding etching rate in the laser-affected zones (green points in the

graph). The etching rate in the laser-affected zones (represented in green in the graphs) is higher than the etching rate in the beams. For technical reasons, the range of stress that we could test in this etching experiment is unfortunately smaller than the one that we predicted between nanogratings lamellae [7] (about 1.2 for the lower stress and 2 GPa for the highest). As a result it is difficult to conclude whether the stress is the only cause of the accelerated etching observed after laser exposure. However, if we extrapolate the experimental curves in Fig. 53 to higher stress level, we obtained an etching rate close to the measured one.

5.   Conclusion

Our experiments demonstrate the etching rate enhancement resulting from the presence of stress whether it is tensile or compressive. The isotropic nature of the material could explain why the etchant is equally sensitive to both types of stress.

Although the enhancement of the etching rate due to stress has been demonstrated, we were not able to measure it for sufficiently high stress level to fully conclude about the ratio between stress and photo-chemical effects in the etching rate enhancements. However, an extrapolation of our experimental results to higher stress levels suggest that stress is the dominant factor in the etching rate enhancement.

Up to now, in our thesis we have investigated only femtosecond pulses. The next and final chapter is dedicated to a comparison between picosecond laser and femtosecond laser for the micromachining of fused silica, in combination with an etching process. The objective is to investigate the influence of the pulse duration on the machining quality, in particular in the regime of a few picoseconds where the laser-matter interaction dynamics (excitons dynamics in particular) shows a transition [8].

6.   References

1. Y. Bellouard, A. Said, M. Dugan, and P. Bado, "Fabrication of high-aspect ratio, micro-fluidic channels and tunnels using femtosecond laser pulses and chemical etching," Opt. Express **12**, 2120–2129 (2004).
2. F. Madani-Grasset and Y. Bellouard, "Femtosecond laser micromachining of fused silica molds," Opt. Express **18**, 21826–21840 (2010).
3. A. Agarwal and M. Tomozawa, "Correlation of silica glass properties with the infrared spectra," J. Non-Cryst. Solids **209**, 166–174 (1997).
4. A. Champion and Y. Bellouard, "Direct volume variation measurements in fused silica specimens exposed to femtosecond laser," Opt. Mater. Express **2**, 789-798 (2012).
5. T. N. Vasudevan and R. S. Krishnan, "Dispersion of the stress-optic coefficient in glasses," J. Phys. D: Appl. Phys. **5**, 2283 (1972).
6. Y. Bellouard , E. Barthel, A. A. Said, M. Dugan, and P. Bado, "Scanning thermal microscopy and Raman analysis of bulk fused silica exposed to low energy femtosecond laser pulses," Opt. Express **16**, 19520-19534 (2008).

7. A. Champion, M. Beresna, P. Kazansky, and Y. Bellouard, "Stress distribution around femtosecond laser affected zones: effect of nanogratings orientation," Opt Express **21**, 24942–24951 (2013).
8. B. C. Stuart, M. D. Feit, S. Herman, A. M. Rubenchik, B. W. Shore, and M. D. Perry, "Nanosecond-to-femtosecond laser-induced breakdown in dielectrics," Phys. Rev. B **53**, 1749-1761 (1996).

Chapter V. A comparison between femtosecond and picosecond lasers for micromachining of silica

This chapter investigates the influence of pulse duration, comparing picosecond and femtosecond pulses effects on laser micromachining. The objective is to compare the pulse duration influence on the machining quality, in particular in the regime of a few picoseconds where the laser-matter interaction dynamics shows a transition between two different regimes. The motivation for this comparison is also technological. Picosecond lasers offer cutting-edge advantages over femtosecond laser in terms of cost, simplicity and average power available. However, it is unclear if such lasers are able to provide the same process ability than femtosecond lasers.

The main part of this chapter has been reported in: C. Corbari, A. Champion, M. Gecevicius, M. Beresna, Y. Bellouard, and P. G. Kazansky, "Femtosecond versus picosecond laser machining of nano-gratings and micro-channels in silica glass," Opt. Express **21**, 3946–3958 (2013).

1. Introduction

Since one of the major aspects of this thesis involves micromachining control and quality as determined by laser parameters, the goal of this chapter is to investigate the importance of the pulse duration and in particular, to critically compare picosecond versus femtosecond regimes. This comparison is motivated by the industrial attractiveness of picosecond lasers that may offer a cheaper and higher throughput solution than femtosecond lasers. As seen in the previous chapters, the dynamics of energy transfer from excited electrons to the lattice leads to modifications when fused silica is exposed to intense laser pulses [1–3]. According to the pulse duration three modification regimes have been observed depending on the time required by the hot electrons to transfer their energy to the lattice via electron-phonon scattering. In the case of fused silica this relaxation time is about 1 ps [1].

For a pulse duration smaller than the electron relaxation time, thermal diffusion does not take place since the electrons in the conduction band are heated much faster than they can cool by phonon scattering. In this case, their energy is used to seed an avalanche mechanism and the energy is transferred to the lattice after the pulse has ended on a time scale much shorter than the heat diffusion time, which produces a permanent modification in the material with essentially no collateral damage. From the machining point of view, the resulting patterns are smooth and much smaller than with longer pulses, leading to precise machining.

A theoretical framework for the case in which the pulse durations are equal to the electron relaxation time is not available due to the intrinsic complexity. It is known, however, that the fluence damage threshold for silica glass deviates in the 1-20 ps pulse range from the thermally driven square root of pulse duration dependence associated with longer pulses [1]. For single pulse bulk modification of silica glass, Burakov et al. showed that long exposure times were correlated to the material expansion leading to a negative refractive index change in the irradiated zones [4]. The generation of pressure waves - resulting in stress accumulation and positive index change in the region surrounding the focal volume - occurs as a consequence of the material expansion.

Although picosecond lasers are not widely used for micromachining in dielectrics, it has been demonstrated that this intermediate regime presents advantages regarding specific applications. Indeed, Juodkazis and Misawa highlighted how thermally induced stress in borosilicate glass irradiated by 12 ps pulses could be exploited for crack-free in-bulk recording [5]. Optical waveguides were fabricated by laser writing with a wide 50-fs to 5-ps range of pulse duration and showed the lowest loss of 0.2 dB/cm for 1 ps pulses [6,7].The etching rate of fused silica is accelerated due to stress accumulation and glass densification. For instance the relationship between laser exposure and etching rate is shown in [8,9]. For the pulse durations in the ps-range, evidence of nanogratings formation has never been demonstrated [10]. Nanogratings are thought to favor the etchant

penetration [11]. They are also associated with form-birefringence that is exploited for the realization of spatially variant phase plates [12].

In this chapter, we investigate the hypothesis that nanogratings and faster etching rate can be achieved by pulses of duration comparable to the electro-phonon scattering time. The ability of these ps-pulses to generate self-assembled nanogratings and to promote selective chemical etching in the laser exposed regions is demonstrated. The suitability of ps-pulses for the fabrication of polarization sensitive elements or for a two-step machining approach is discussed in terms of retardance, etching rate and morphology of the etched regions by comparison with fs-pulses of the same pulse energy and fluence.

2.   **Experimental set-up and methods**

For laser inscription in the picosecond regime, a neodymium-doped yttrium vanadate (Nd:YVO$_4$) laser emitting trains of 8 ps pulses at the wavelength of 1064 nm (Super-Rapid, Lumera Laser GmbH) was employed. In the femtosecond regime, laser writing was performed using a mode-locked regenerative amplified Yb:KGW (ytterbium-doped potassium gadolinium tungstate) laser (PHAROS by Light Conversion Ltd.) operating at λ = 1030 nm. The initial laser pulse duration of 300 fs was stretched to 600 fs measured with the internal pulse stretcher. The pulse duration was monitored with a single-shot autocorrelator. The pulse duration was chosen to match the optimum condition for the fabrication of spatially variant wave-plates and polarization mode converters [12].

For these experiments, a 25 x 25 x 1 mm^3 silica plate (SPECTROSIL 2000 by UQG ltd.) was used. The laser beam was focused in the bulk of the sample by a 20X aspheric lens with a numerical aperture of 0.5 (New focus 5720).

Two sets of lines were written with both femtosecond and picosecond laser systems using identical parameters except for the pulse duration. The lines were written 100 µm below the surface by translating the sample transversely to the beam propagation direction. In order to prevent changes in the material modifications by reversal of the writing direction, all lines were written in the same direction [13]. Laser inscription was carried out aligning the direction of the light polarization both orthogonal and parallel to the writing direction using a half-wave plate placed immediately before the focusing lens. The writing speed ranged from 25 µm/s to 6400 µm/s and the laser repetition rate was varied from 12.5 kHz to 400 kHz. As the sample is translated, the effective number of pulses, N_{eff}, is given by:

$$N_{\text{eff}} = \frac{wf}{v} \qquad (5.1)$$

with f being the laser repletion rate, v the sample translation speed and w the focal spot diameter. Correspondingly, the net fluence or deposited energy is calculated from eq (5.1):

$$F = \frac{4E_{\mathrm{p}}}{\pi w^2} N_{\mathrm{eff}} = \frac{4E_{\mathrm{p}} f}{\pi w v} \qquad\qquad (5.2)$$

where E_{p} is the pulse energy.

The threshold pulse fluence for multi-shot bulk damage – as inspected by bright light microscopy - in fused silica when focusing the 1064 nm radiation of the ps-laser was experimentally measured as 7.5 ± 0.2 J/cm^2 (E_{p} = 0.8 µJ, w = 3.68 µm). These parameters were used throughout the work. Therefore the same pulse fluence was used for both fs and ps laser inscription experiments.

The threshold for self-focusing for a collimated Gaussian beam is defined by the self-focusing critical power P_{cr} = 4.3 MW [14]. However, when the beam is focused by a lens, the occurrence of collapse always requires power above the critical level [15,16]. Our experimental conditions correspond to optical power P_{in} equal to 1.3 and 0.1 MW for the fs and ps pulses respectively and are therefore well below the threshold for self-focusing.

Nanogratings were characterized by quantitative birefringence measurements (Cri Abrio imaging system). This system allows accurate measurements of the direction of the slow axis of birefringence as well as the strength of the retardance.

After the laser irradiation, the sample was side-lapped and polished to reveal the cross-sections of the laser written lines and remove the layer of glass that could have been affected by surface/edge effect such as beam clipping. Micro-channels were formed by etching the sample with 2.5% hydrofluoric acid (HF) for 80 minutes. The length of the etched channels was measured under bright illumination optical microscopy with a resolution of ± 1 µm.

3.   Results and Discussion

a.   *Assessment of ps-lasers for the fabrication of spatially-variant phase-plates*

In our experiment, exposure of silica glass to picosecond pulses produces a negative refractive index change, as checked by digital holographic microscopy. Although it is not a sufficient proof in itself, this negative refractive index change suggests the presence of nanogratings, so far only observed in laser tracks produced by fs-laser irradiation [10]. Nanogratings are characterized by a succession of nano-layers (~20 nm) separated by apparently unmodified silica with a periodicity in the order of 150-450 nm depending on pulse energy and wavelength [17,18]. The orientation of the nano-planes follows the direction of the laser polarization. Another periodicity, this time along the head-to-tail direction of the laser damage cross-section, may be present with a period of ~ λ/n where λ is the laser wavelength and n the refractive index of silica [17,19].

Quantitative birefringence measurements performed on the radial structure shown in Fig. 54 (a-c) demonstrate that silica irradiated by picosecond pulses displays both the form-birefringence and the dependence on the orientation of laser polarization expected from nanogratings. The polarization was kept parallel to the writing direction. Fig. 54 (b) shows that the direction of the slow axis of birefringence, represented by pseudo-colors (see legend in the top-right corner) is perpendicular to the orientation of the laser polarization. The evidence of nanograting formation with 8 ps pulses was obtained by imaging the cross section of a laser track by Scanning Electron Microscopy (SEM) (Fig. 55). The SEM image shows the top of the cross-section of the laser damage with the nano-planes responsible for the form birefringence aligned perpendicular to the direction of the laser polarization (vertical in Fig. 55). The periodicity is $\Lambda \sim 250$ nm which is comparable to nanogratings formed by fs-laser at similar pulse energies [17]. A second periodicity, $\Lambda/n \sim 733$ nm, apparently increasing as we move away from the tip of the structure is observed along the horizontal direction. Note that on this SEM image of the cleaved laser track, the irradiated zone seems to protrude out of the plane which is consistent with the volume expansion in the nanogratings zones [4,20,21].
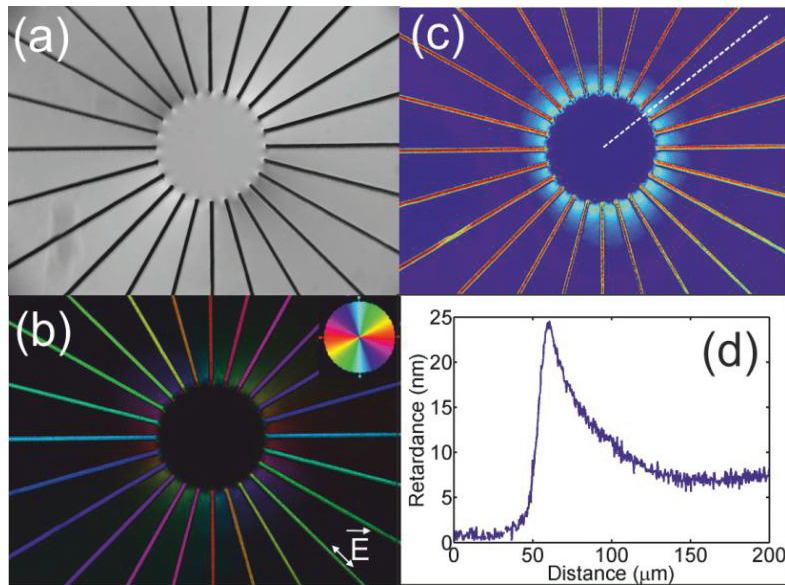
Fig. 54. Optical image of a set of laser tracks radiating out from a virtual circle ($\varnothing$ = 100 µm). The angle between the lines is 15 deg. The laser polarization is parallel to the writing direction. λ = 1064 nm, NA = 0.65, τ = 8 ps, E_{p} = 2 µJ, f = 200 kHz, v = 200 µm/s. (b) and (c) Quantitative birefringence measurements of the laser tracks in (a). (b) Pseudo-colours represent the angle of the slow axis of birefringence as indicated by the legend in the top right corner. (c) Pseudo-colours represent the strength of the retardance. (d) Retardance vs. position along the dashed line in (c). The retardance measured between two laser tracks is indicative of stress-induced birefringence.
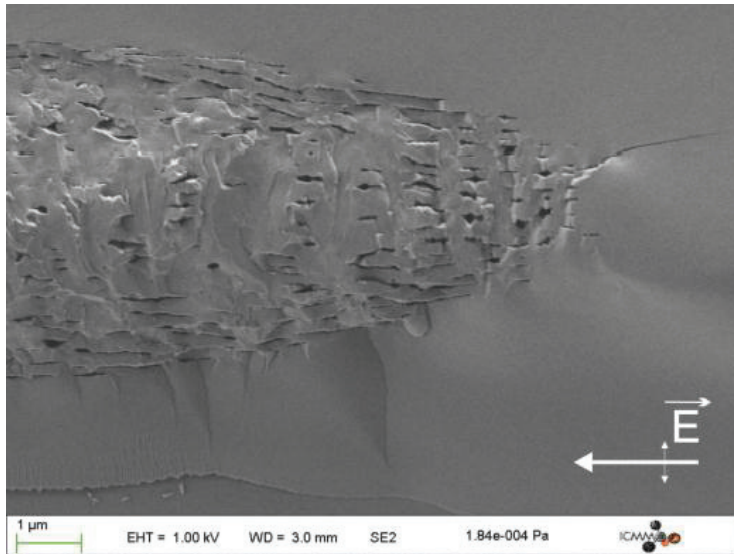
Fig. 55. Field Emission Gun scanning electron microscope (FEG-SEM) image of a cleaved laser track in fused silica. The formation of nano-gratings by ps-pulses is shown. Experimental conditions: λ = 1064 nm, NA = 0.65, τ = 8 ps, E_{p} = 1 µJ, f = 200 kHz, v = 200 µm/s. The laser radiation was shining from the right end of the picture. Polarization oriented perpendicular to the writing direction.

The form-birefringence associated with nanogratings implies that the fabrication of polarization mode converters and spatially variant phase plates are possible even in this long pulse regime [12]. Laser writing by fs- and ps-pulses was compared by measuring the strength of the retardance. The retardance is defined as the product $R \equiv \Delta n \times L$ where Δn is the overall birefringence and L the optical path length. The retardance increases with the net fluence reaching its maximum value at R = 113 $\pm$ 10 nm (Fig. 56). The measured value enables writing quarter-wave plates for operation in the visible. Further improvement is possible by using lower NA lens, achieving larger L through the increased Rayleigh range.
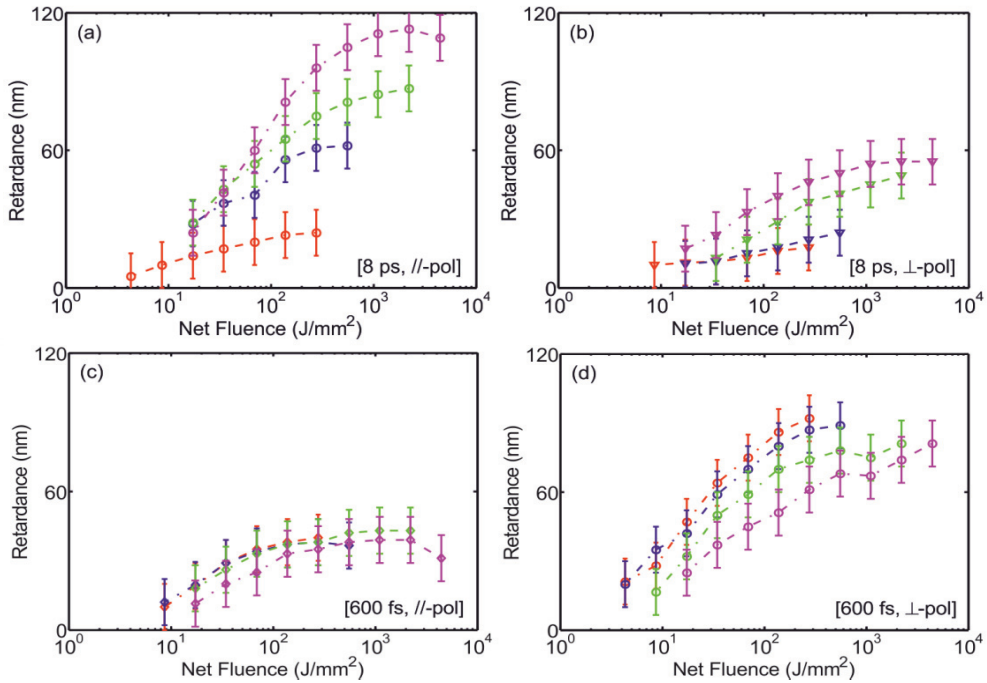
Fig. 56. Measurements of the retardance vs. net laser fluence in tracks processed by (a) 8 ps longitudinal polarisation and (b) 8 ps transverse polarisation, (c) 600 fs longitudinal polarisation and (d) 600 fs transverse polarisation. Line colors correspond to: (red) 25 kHz, (blue) 50 kHz, (green), 200 kHz, and (magenta) 400 kHz.

The laser induced retardance presents a marked dependence on the laser repetition rate (Fig. 56). It is an indication that the rate at which the energy is deposited into the glass affects the development of nanogratings. Shimotsuma et al. observed a reduction of the laser induced birefringence with increasing repetition rate when irradiating silica glass with 70 fs [22]. Our experiments with 600 fs pulses follow the same trend [Fig. 57 (a)]. The drop in the strength of the retardance with reduced intra-pulse is interpreted as evidence of the detrimental effect on a microsecond timescale caused by the heat accumulation on the formation of the naogratings. In contrast for picoseconds pulses the retardance is consistently higher the shorter is the intra-pulse duration [Fig. 57 (b)]. We suppose that for long pulse the process of glass modification leading to the formation of nanogratings is facilitated by the presence of defect states with a life time comparable to the inter-pulse intervals in our experiment. A plausible candidate is the 2.0 eV absorption (1.9 eV emission) band associated to the excited state of non-bridging oxygen hole center (NBOHC) that decays with a life time of about 10-20 μs [23-25]. The presence of defects creates energy levels within the bandgap of

silica and facilitates the production of free electrons that seed the avalanche ionization. It is the strong intensity dependence of the generation of seed electrons by multi-photon ionization that makes damage formation by longer pulses more susceptible to the presence of the defect state. The peak intensity of the 8- ps pulses used in our experiment is 1 TW/cm^2; that is more than 10 times lower than the intensity of the 600 fs pulses (12.5 TW/cm^2) and over 100 times lower than the intensity used by Shimotsuma et al.. The estimates on the intensity are given as an upper limit which does not take into account the clamping effect.

It is worth noting here that the process of relaxation of the NBOHC excited state may be responsible for the opposite dependence observed in the fs-regime in place of the temperature effects advocated earlier. For example, the much larger number of defects created by fs-pulses may cause stronger absorption of the incoming pulses or defect saturation may occur.
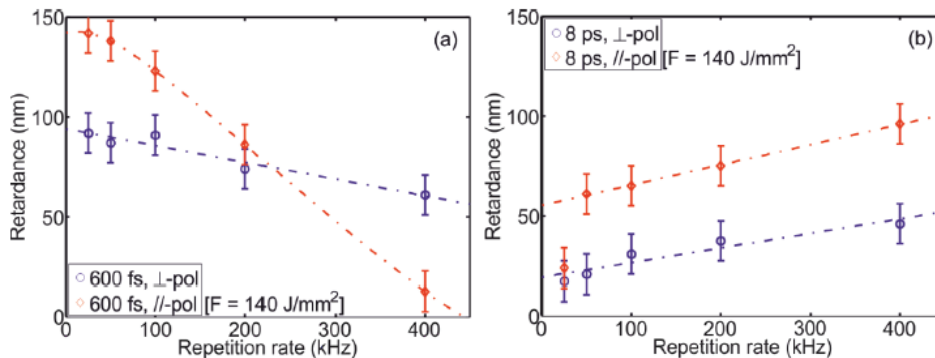
Fig. 57. Dependence of the retardance with the laser repetition rate for (a) 600 fs (b) 8 ps pulses at fixed net fluence. Dotted-dashed lines are guides for the eye.

Despite the fact that the value of the induced retardance is comparable to what is obtained with fs-lasers, the biggest hurdle to overcome for ps-laser fabricated wave-plates is posed by scattering and by the development of a stress regions surrounding the laser tracks resulting in rupture of the glass at high fluences as more and more lines are packed together to raster scan an area of interest. Such a stress build-up is visible in Fig. 54 (c) by observing the regions in between lines. A light shade of blue indicates the areas of higher retardance. A model of the laser induced stress distribution allows us to confidently attribute the retardance measured in between lines to stress-induced birefringence. The line-scan in Fig. 54 (d) provides evidence that the stress increases as the lines converges.

Finally, we report the observation in laser machining by ps-pulses of the so-called "quill effect" whereby laser-matter interaction is shown to be sensitive to the direction of movement of the laser beam [13,26]. A marked sensitivity of the

material modification from the direction of writing is observed when 8 ps pulses of 2 µJ pulse energy are focused with a 0.65 NA objective 150 µm below the surface of a silica plate (Fig. 58). Despite that we do not have instruments capable of measuring directly the pulse front tilt (PFT) for ps-pulses, our findings are consistent with the mechanism originally proposed for fs-pulses. We consider PFT as given by the product of temporal and spatial chirp of the pulse: PFT = AD + GDD × SC where AD is the angular dispersion, GDD is the group-delay dispersion and SC the spatial chirp. The contribution of angular dispersion to the PFT was considered to be negligible due to the absence of astigmatic focal spots in the laser-affected zones. The pulses from the picosecond laser were found to be temporally chirped. The spectral bandwidth was measured as 0.26 nm, hence much larger than the transform limited bandwidth of 0.17 nm, giving GDD = 1.1 × 10^7 fs^2. Such a large value of GDD implies that even a small SC at the resolution limit of our optical spectrum analyzer (0.05 nm) would produce PFT of about 900 fs/mm for a 1 mm diameter collimated beam. For comparison, in fs-laser irradiation of glass writing anisotropy is observed with PFT of the order of 1.8 fs/mm before the focusing lens.
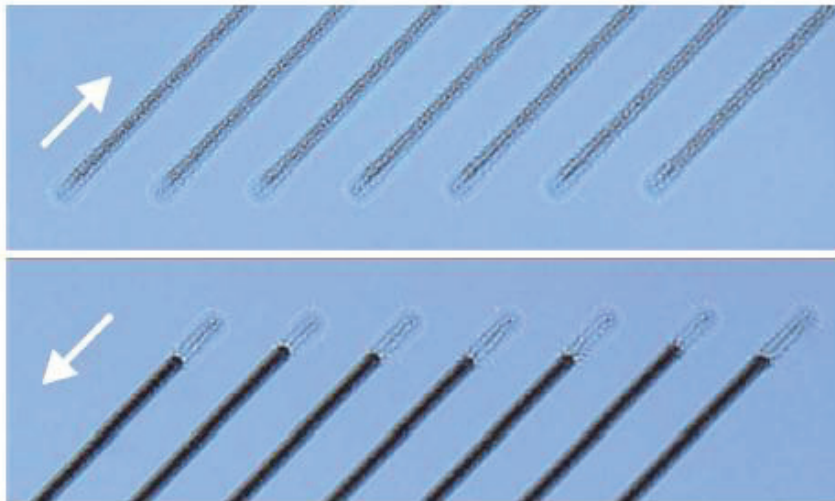
Fig. 58. Microscope bright field images of line structures written in opposite directions using 8 ps pulses. The arrows indicate the direction of writing. The separation between lines is 50 µm. In the top image the damage is uniform along the whole length of the structure. In the bottom image we observe nano-gratings formation (dark lines). Experimental conditions: λ = 1064 nm, NA = 0.65, τ = 8 ps, E_p = 2 µJ, f = 200 kHz, v = 200 µm/s.

b. *Assessment of ps-lasers for micro-machining by chemical etching of laser exposed areas*

The etching rate of fs-laser irradiated regions has been shown to depend upon the stress and densification in the glass in the low fluence regime and by the orientation of the nanogratings in the high fluence regime [9,27]. Hence, the formation of nanogratings by 8 ps-pulses and the concurrent build-up of stress in the regions surrounding the laser tracks will have an impact on the two-step machining by laser irradiation and chemical etching. We looked at aspects that concern the quality of the etched surface, the correlation between etched regions and the light intensity distribution, and finally the etching rate.

The quality of the etched surface is assessed by the SEM imaging of the micro-channel openings (Fig. 59). Although this method cannot provide quantitative information about the wall roughness, it is evident that the channels irradiated by 8 ps laser pulses present an irregular surface. In the irradiated channels etchant penetration produces deep trenches extending beyond the laser-affected zones as a result of the formation of either micro-cracks or regions of stress concentration. The lack of correlation between laser intensity profile and etched contour in the picosecond laser two-step machining is a general feature which bears as a consequence our inability to predict the outcome of the etching process from the known applied intensity distribution, ultimately preventing precision micro-machining (Fig. 59). In contrast, femtosecond laser two-steps machining benefits from a very reproducible and reliable process which is known to be primarily driven by the deposited net fluence [28]. This is noticeable in Fig. 60 where each column refers to channels fabricated with the same net fluence but at different laser repetition rate and writing speed. In each column the shape of the aperture of the femtosecond written micro-channels is remarkably similar. This is true even for the lowest fluences where the nanogratings are not fully formed as the number of pulses is below 100. The same cannot be said for two-step machining with 8 ps pulses for which the rate at which the energy is deposited into the silica matrix is shown to play a role (Fig. 59). In fact, the size of the micro-channel also grows as the repetition is increased indicating the detrimental effect of heat accumulation and/or pressure build up.
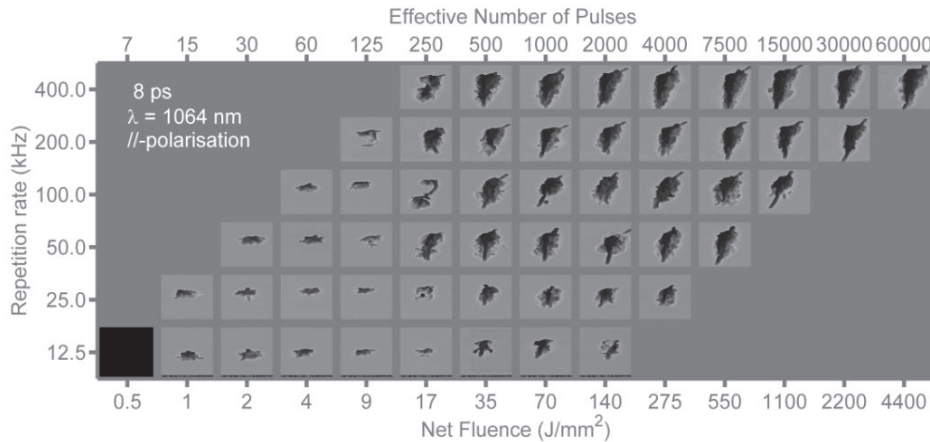
Fig. 59. SEM images of the opening of the etched micro-channels produced by 8-ps laser irradiation followed by 2.5% HF etching for 80 min. E_p = 0.8 μJ, NA = 0.5. Each SEM image is 18.6 μm wide. The writing speed ranged from 25 μm/s to 6400 μm/s.
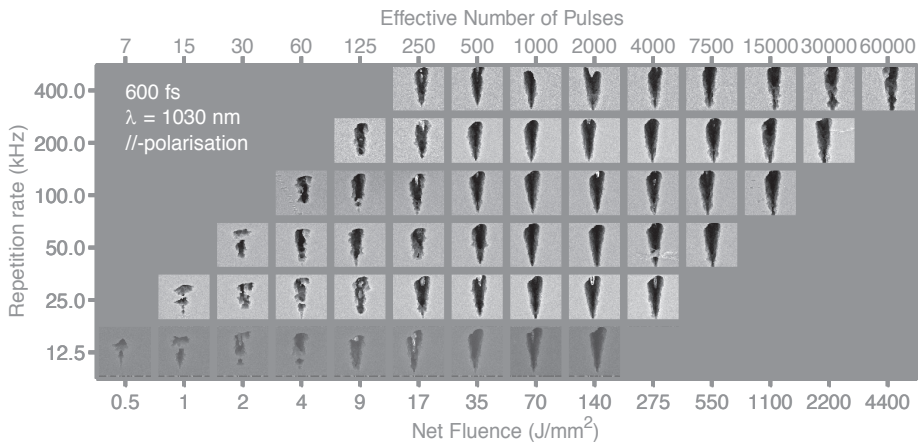
Fig. 60. SEM images of the opening of the etched micro-channels produced by 600-fs laser irradiation followed by 2.5% HF etching for 80 min. E_p = 0.8 μJ, NA = 0.5. Each SEM image is 18.6 μm wide. The writing speed ranged from 25 μm/s to 6400 μm/s.

Ultimately, it is the etching rate that defines the aspect -ratio of the structures that can be fabricated by the two-step laser machining (i.e. the higher is the etching rate contrast between pristine and laser-affected zones, the higher is the aspect ratio). Despite the stress region surrounding the laser tracks and the presence of nanogratings, picosecond pulses do not give significant advantage for two-step machining over shorter pulses as the etching rate attains the same maximum value of 2 ± 0.5 μm/min in both ps- and fs- laser irradiated tracks (Fig.

61). However, the dependence of the length of the micro-channel on the net fluence after 80 minutes etching reveals a very different behavior for 8 ps and 600 fs (Fig. 61). In the ps-regime, etched lengths of about 120-150 µm are obtained in the whole range of fluences explored in this study (0.5-4500 J/mm²), irrespective of the polarization direction of the writing beam. The same behavior and etched length are obtained also for the etching of laser tracks written at 532 nm. Conversely the etching of channels fabricated by fs-laser pulses presents a far richer dynamic as the fluence is increased with the fastest etching occurring in the low net fluence regime at ~10 J/mm² and in the high net fluence regime (~103 J/mm²).

The faster etching rate observed in ultra-short pulse laser irradiated silica glass as compared to pristine glass has been ascribed to the structural modification of the material [8], to densification [9] or to the presence of nano-cracks within nanogratings [29]. To distinguish the contributions of nanogratings to the etching process at different fluence regimes, we looked at correlations between the laser induced birefringence (Fig. 56) and the corresponding length of the etched channels (Fig. 61).

In the picosecond regime, the etching rate appears to be constant with the net fluence (Fig. 61). No obvious correlation between birefringence and etching rate is noted by comparison with the retardance measured in Fig. 3.

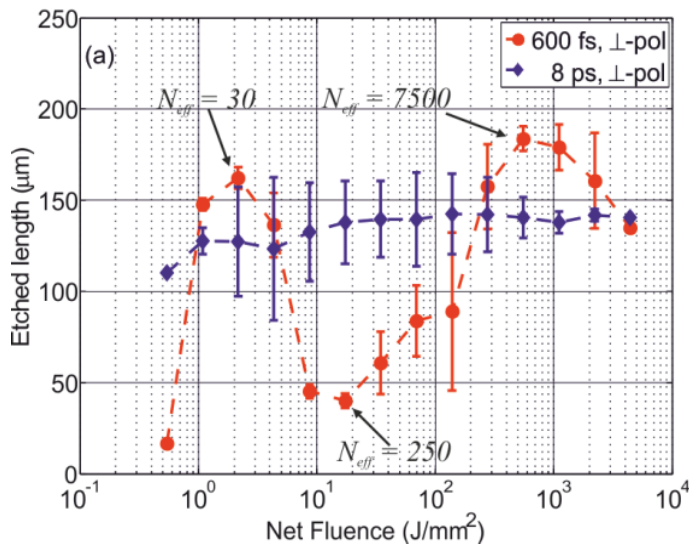**Fig. 61.** Comparison of the length of the micro-channel obtained in silica processed by fs- and ps-laser after 80 min in 2.5% HF bath. Each data point in the plot is the average of the etched length of channels exposed at the same net fluence and the error bars give the corresponding standard deviation. Hence, a small error bar indicates that the etched length has little dependence on laser frequency and scanning speed.

In the fs-regime the etching rate presents two maxima, one in the low net fluence regime (~10 J/mm^2) and the second in the high net fluence regime (~103 J/mm^2). The trend observed at low fluence was first reported in a previous work carried out at lower pulse energy (0.3 µJ) and in a limited net fluence range [28]. Based on this trend we recognize four separate net-fluence regimes:

1) For N_{eff} < 30 nanogratings are not formed. However, this is not a type I modification owing to the relatively long pulse duration (600 fs). We confirmed it by measuring a negative average refractive index change by digital holographic microscopy. This regime corresponds to the initial phases prior to the formation of nanogratings. An illustration of this regime is provided by Richter et al. and it consists of a chaotic structure with damages randomly positioned in the focal volume [18]. We suppose that in such regime densification occurs within each damage point with consequent onset of a tensile stress. As more and more pulses are accumulated the stress increases explaining the initial rise in the etching rate. Finally, since the damage areas are randomly positioned within the focal volume no effect of the polarization orientation is to be expected in this region.

2) For 30 < N_{eff} < 250, nanogratings are still not completely formed as evidenced from the birefringence measurements showing that the retardance has not reached its plateau yet. The work by Richter highlights that as the number of pulses increases the glass may start to rupture. The consequence is relaxation of the tensile stress and reduction of the etching rate.

3) As the effective pulse number reaches values 200 < N_{eff} < 7500 the nanogratings are organized in a well-defined periodic structure. As the net fluence increases, compressive stress develops in the regions surrounding the laser track favoring the etching process.

4) Eventually, for N_{eff} > 7500 the glass cannot cope with the increasing pressure and cracks releasing the accumulated stress.

4.   **Conclusions**

In this chapter, the observation of self-assembled nanogratings and of the change of material modification with the direction of writing by ps-pulses is reported for the first time. The orientation and the period of the nanoplanes are as obtained with fs-pulses. However, the retardance associated with the laser-induced form-birefringence is observed to increase with the laser repetition rate in contrast to femtosecond pulses of the same energy. Picosecond pulses having 10-100 times lower peak intensity than femtosecond pulses are more susceptible to the presence of defect states for the creation of seed electrons. It is suggested that the formation of nanogratings is mediated by defects such as the 2.0 eV excited state of the NBOHCs whose concentration decays on a time scale comparable to the inter-pulse intervals.

We have tested the relevancy of the picosecond laser for two main applications: the fabrication of embedded waveplates and micro-machining by

laser irradiation in combination with chemical etching. Although pulses at 10 ps are far from the limit for strong collateral damage in fused silica, a strong stress area was found surrounding the laser-affected zones. Such a stress makes waveplates or micro-fluidic/opto-mechatronic devices impossible to achieve with the required quality. Indeed crack formation and strong scattering occur almost systematically when lines are written next to each other. As a result, the light passing trough waveplates or other optical components fabricated under these conditions is reduced and diffracted, and devices cannot be used. On the other hand the quality after etching is not sufficient to fabricate accurate devices, as shown in Fig. 6. Therefore the ps class of lasers can be used for ablation, but not for precision micromachining in glass.

5.   Reference

1. B. C. Stuart, M. D. Feit, S. Herman, A. M. Rubenchik, B. W. Shore, and M. D. Perry, "Nanosecond-to-femtosecond laser-induced breakdown in dielectrics," Phys. Rev. B Condens. Matter **53**(4), 1749–1761 (1996).

2. S. S. Mao, F. Quere, S. Guizard, X. Mao, R. E. Russo, G. Petite, and P. Martin, "Dynamics of femtosecond laser interactions with dielectrics," Appl. Phys 79, 1695–1709 (2004).

3. C. B. Schaffer, A. Brodeur, and E. Mazur, "Laser-induced breakdown and damage in bulk transparent materials induced by tightly focused femtosecond laser pulses," Meas. Sci. Technol. **12**(11), 1784–1794 (2001).

4. I. M. Burakov, N. M. Bulgakova, R. Stoian, A. Mermillod-Blondin, E. Audouard, A. Rosenfeld, A. Husakou, and I. V. Hertel, "Spatial distribution of refractive index variations induced in bulk fused silica by single ultrashort and short laser pulses," J. Appl. Phys. **101**(4), 043506 (2007).

5. S. Juodkazis, H. Misawa, and I. Maksimov, "Thermal accumulation effect in three-dimensional recording by picosecond pulses," Appl. Phys. Lett. **85**(22), 5239–5241 (2004).

6. H. Zhang, S. M. Eaton, and P. R. Herman, "Low-loss Type II waveguide writing in fused silica with single picosecond laser pulses," Opt. Express **14**(11), 4826–4834 (2006), http://www.opticsinfobase.org/oe/abstract.cfm?URI=oe-14-11-4826.

7. B. McMillen, B. T. Zhang, K. P. Chen, A. Benayas, and D. Jaque, "Ultrafast laser fabrication of low-loss waveguides in chalcogenide glass with 0.65 dB/cm loss," Opt. Lett. **37**(9), 1418–1420 (2012).

8. A. Marcinkevičius, S. Juodkazis, M. Watanabe, M. Miwa, S. Matsuo, H. Misawa, and J. Nishii "Femtosecond laser-assisted three-dimensional microfabrication in silica," Opt. Lett. **26**(5), 277–279 (2001).

9. Y. Bellouard, T. Colomb, C. Depeursinge, M. Dugan, A. A. Said, and P. Bado, "Nanoindentation and birefringence measurements on fused silica specimen exposed to low-energy femtosecond pulses," Opt. Express **14**(18), 8360–8366 (2006), http://www.opticsinfobase.org/oe/abstract.cfm?URI=oe-14-18-8360.

10. Y. Shimotsuma, P. G. Kazansky, J. R. Qiu, and K. Hirao, "Self-organized nanogratings in glass irradiated by ultrashort light pulses," Phys. Rev. Lett. **91**(24), 247405 (2003).

11. C. Hnatovsky, R. S. Taylor, E. Simova, V. R. Bhardwaj, D. M. Rayner, and P. B. Corkum, "Polarization-selective etching in femtosecond laser-assisted microfluidic channel fabrication in fused silica," Opt. Lett. **30**(14), 1867–1869 (2005).

12. M. Beresna, M. Gecevicius, and P. G. Kazansky, "Polarization sensitive elements fabricated by femtosecond laser nanostructuring of glass Invited," Opt. Mater. Express **1**(4), 783–795 (2011).

13. W. Yang, P. G. Kazansky, Y. Shimotsuma, M. Sakakura, K. Miura, and K. Hirao, "Ultrashort-pulse laser calligraphy," Appl. Phys. Lett. **93**(17), 171109 (2008).

14. A. Couairon and A. Mysyrowicz, "Femtosecond filamentation in transparent media," Phys. Rep. **441**(2-4), 47–189 (2007).

15. A. Couairon and L. Berge, "Modeling the filamentation of ultra-short pulses in ionizing media," Phys. Plasmas **7**(1), 193–209 (2000).

16. A. Couairon and P. G. Kazansky, (Personal Communication 2010).

17. W. J. Yang, E. Bricchi, P. G. Kazansky, J. Bovatsek, and A. Y. Arai, "Self-assembled periodic sub-wavelength structures by femtosecond laser direct writing," Opt. Express **14**(21), 10117–10124 (2006).

18. S. Richter, M. Heinrich, S. Doring, A. Tunnermann, and S. Nolte, "Formation of femtosecond laser-induced nanogratings at high repetition rates," Appl. Phys, Adv. Mater. **104**, 503–507 (2011).

19. C. Hnatovsky, R. S. Taylor, P. P. Rajeev, E. Simova, V. R. Bhardwaj, D. M. Rayner, and P. B. Corkum, "Pulse duration dependence of femtosecond-laser-fabricated nanogratings in fused silica," Appl. Phys. Lett. **87**(1), 014104 (2005).

20. A. Champion and Y. Bellouard, "Direct volume variation measurements in fused silica specimens exposed to femtosecond laser," Opt. Mater. Express **2**(6), 789–798 (2012), http://www.opticsinfobase.org/ome/abstract.cfm?URI=ome-2-6-789.

21. J. Canning, M. Lancry, K. Cook, A. Weickman, F. Brisset, and B. Poumellec, "Anatomy of a femtosecond laser processed silica waveguide, Invited," Opt. Mater. Express **1**(5), 998–1008 (2011).

22. Y. Shimotsuma, M. Sakakura, P. G. Kazansky, M. Beresna, J. R. Qiu, K. Miura, and K. Hirao, "Ultrafast manipulation of self-assembled form birefringence in glass," Adv. Mater. (Deerfield Beach Fla.) **22**(36), 4039–4043 (2010).

23. L. Skuja, K. Kajihara, M. Hirano, and H. Hosono, "Oxygen-excess-related point defects in glassy/amorphous SiO2 and related materials," Nucl. Instrum. Meth. B **286**, 159–168 (2012).

24. Y. M. Cannas, V. Lavinia, and B. Roberto, "Time resolved photoluminescence associated with non-bridging oxygen hole centers in irradiated silica," Nucl. Instrum. Meth. B **266**(12-13), 2945–2948 (2008).

25. S. Richter, F. Jia, M. Heinrich, S. Döring, U. Peschel, A. Tünnermann, and S. Nolte, "The role of self-trapped excitons and defects in the formation of nanogratings in fused silica," Opt. Lett. **37**(4), 482–484 (2012).

26. D. N. Vitek, E. Block, Y. Bellouard, D. E. Adams, S. Backus, D. Kleinfeld, C. G. Durfee, and J. A. Squier, "Spatio-temporally focused femtosecond laser pulses for nonreciprocal writing in optically transparent materials," Opt. Express **18**(24), 24673–24678 (2010), http://www.opticsinfobase.org/oe/abstract.cfm?URI=oe-18-24-24673.

27. Y. Bellouard, E. Barthel, A. A. Said, M. Dugan, and P. Bado, "Scanning thermal microscopy and Raman analysis of bulk fused silica exposed to low-energy femtosecond laser pulses," Opt. Express **16**(24), 19520–19534 (2008), http://www.opticsinfobase.org/oe/abstract.cfm?URI=oe-16-24-19520.

28. S. Rajesh and Y. Bellouard, "Towards fast femtosecond laser micromachining of fused silica: The effect of deposited energy," Opt. Express **18**(20), 21490–21497 (2010), http://www.opticsinfobase.org/oe/abstract.cfm?URI=oe-18-20-21490.

29. C. Hnatovsky, R. S. Taylor, E. Simova, P. P. Rajeev, D. M. Rayner, V. R. Bhardwaj, and P. B. Corkum, "Fabrication of microchannels in glass using focused femtosecond laser radiation and selective chemical etching," Appl. Phys, Adv. Mater. **84**, 47–61 (2006).

Chapter VI. Conclusion and outlook

1. **Conclusion**

Femtosecond laser are investigated for micromachining, owing to, a direct three dimensional writing, high quality and small size of the written patterns in transparent material. For instance, combined with chemical etching, MEMS, or microfluidic channels can be fabricated. Without etching, waveguides or optical components can be achieved. Laser parameters were up to now, selected by trial-and-error approaches. In particular, the relation between laser parameters and local structural changes, more specifically volume variation leading to stress surrounding laser written patterns, were not well understood. Up to now, the role of the stress in the process etching rate efficiency was unknown.

To fill this gap of knowledge, the goal of this thesis was primarily to investigate localized density variations after the laser exposure. These density variations are *de facto* essential for linking stress and laser-induced nanostructures as well as for gaining more insights about the reported anisotropy of laser modified zones.

In chapter II, we introduced a method based on cantilevers deflection to quantify volume variations in laser-affected zones. In addition to measuring the stress in laser-affected zones according to the deposited energy, this method gave us the opportunity to observe different laser-exposure regimes that lead to different microstructures. For the first time, we effectively observe the switching between densification and expansion, leading to a stress-state inversion. This transition between localized densification and volume expansion suggests a possible scenario to explain the laser-matter interaction with fused silica in terms of microstructural changes. At low energy per pulse and short pulse duration, the laser-affected zones densify, whereas at longer pulse duration and higher pulse energies micro-pores start forming as well as nanogratings. Interestingly, we observe that a volume expansion is not an unambiguous signature of the presence of nanogratings since volume expansions were also observed under certain exposure conditions where no nanogratings were found. The formation of nanopores causes the stress to increase and could lead to crack formation. This built up of stress was highlighted with the cantilever experiment. For low energy deposition well-organized nanogratings form, whereas at higher energies nanogratings start to collapse. When cracks form, stress relaxation occurs. This was correlated with the etching rate dependence on net fluence. This correlation suggests that the etching rate is possibly mainly driven by stress and less by possible photo-induced structural changes. Another important result was found regarding the pulse duration and the regimes types. For instance, at 380 fs, the first exposure regime that consists of homogeneous structure was not observed. With shorter pulses (150 fs), the first regime of microstructural changes is attained at low energy deposition and low energy per pulse. At higher energy, expansion starts. As observed with longer pulse the etching rate and the stress are correlated. For instance, in the regime of densification a maximum stress corresponding to a maximum etching rate is observed. At higher energies when

expansion regime is found, we observed the same phenomenon. We propose the following explanation: at low laser intensity, and short pulses (i.e. < 200 fs), when the plasma density is weak, the SiO_2 matrix breaks to form smaller rings, causing densification in the laser-affected volumes. When the plasma density increases at higher energy per pulse but still in the short pulse regime, nano-porous material is created (bubble oxygen) and the laser-affected zones stop to densify and then expand. At even higher energy the porosities start to organize to form nanogratings. Finally, as the energy per pulse or energy deposition increase built-up of stress creates cracks and the structures relax. For longer pulse, porosities and nanogratings seem to be always there.

In chapter III, we presented a method based on birefringence measurement to quantify the stress *around* laser-affected zones. Sets of lines through the entire sample thickness (but not on the surfaces) are written radially around a circle so that stress gradient is created between the sets. From simulation, retardance measurements and analytical model, the stress around a single set is quantified from the profile between two consecutive sets. This method allows to rapidly quantify the stress. In the nanogratings regime, we were able to measure the influence of nanogratings orientations on the stress surrounding laser-affected zones. A stress level difference of about 25 % was measured between both polarizations (when nanogratings are oriented perpendicular to the writing direction and then oriented parallel to the writing direction). This stress-polarization dependence can be used for accurately tune the stress in laser exposed volumes. In addition, according to our model that assumes a nanogratings expansion (due to nano-porosity), the stress at the interface between laser-affected zones and pristine glass is estimated to be around a few GPa.

In chapter IV, we investigated the influence of the stress on the etching rate. To do so, a mechanism was designed to load (using the laser-induced volume expansions) micro-beams in tensile and compressive stress. These mechanisms did not only allow us to generate stress in a beam but also provide a means for measuring the displacement of the loaded beams. These measurements showed in both cases, tensile and compressive stresses, an increase of the etching rate when the stress increases. Although we were not able to measure at sufficiently high stress, the etching rate dependence, the exponential growth in the data suggests that the etching rate enhancement occurring after laser exposure could be mainly driven by stress and to a lesser extent by photo-induced modifications in the material.

In chapter V, femtosecond laser and picoseconds laser were compared. The objective was to investigate the influence of the pulse duration on the machining quality, in particular in the regime of a few picoseconds where the laser-matter interaction dynamics (excitons dynamics in particular) shows a transition. Thanks to form birefringence measurement and scanning electron microscope observations, we found that nanogratings also form with picoseconds-long pulses. However, the micromachining quality in general is not satisfying due to presence of numerous cracks.

From a theoretical point of view, the outcome of these experiments allow us to propose a mechanism to explain the origin of the etching rate enhancement, and to show why and how this localized enhancement effects may depend preferentially on certain laser exposure parameters.

From a technology development perspective, the results of this thesis provide a tool for optimizing the micromachining of fused silica with respect to the optimal dosage of laser energy deposited in the material to achieve a given micro-machined patterns aspect ratio and conformity. It also provides guidelines for preventing the occurrence of cracks in integrated optical devices.

2.   Outlook

Femtosecond laser interaction with glass is still far from being fully comprehended, especially in term of structural changes after exposure and the role of the stress in chemical etching. Although our thesis has allowed to better understand the type of volume variation according to the laser parameters (we demonstrated state stress inversion) and highlighted the enhancement of the etching when fused silica is subjected to a tensile or compressive stress, questions remain.

First, the graph presented in chapter IV (etching rate as a function of stress in non-laser-affected zones) seems to have an exponential trend which would mean that the stress mainly drives the etching process. However, we cannot confirm this hypothesis since we were not able to test higher experimental stress. Further work should be done to fully conclude on the etching rate enhancement and the effective importance of stress.

Nanogratings formation is not fully understood. We demonstrated that they expand and lead to high stress concentration around them. To explain the transition between densification and expansion, we proposed a scenario in which homogeneous densification occurs at low energy and short pulse duration. When the energy increases, nanopores start forming eventually leading to self-organized nanogratings. However, we do not know when and how they start to form and organize. It has been proposed that porous material and bubbles result from the SiO_2 matrix decomposition when the material cannot be densified anymore. The formation of pores stops the overall densification and at higher energy leads to state stress inversion, due to the switching between a volume reduction to a net expansion. But we do not know how and when the porosities self-organize to form nanogratings. It would be interesting to perform refined experiments with cantilevers combined with SEM observations to see at which energy deposition and energy per pulse expansion start and at which energy per pulse and energy deposition the nanogratings form. Indeed as the energy increases, the plasma becomes more and more dense and absorbent and could trigger the self organization of defects. Based on the Kazansky model, the laser light interferes with the plasma, as a result electrons are accelerated in high localized and organized electric field due to the interference. In this case we could know at

which plasma density (and therefore laser parameters) nanogratings appear in the laser-affected zones.

The work of this thesis gives tools to investigate in depth the volume variation according to the laser and the consequences on micromachining and structural changes. It allows further investigations to answer the remaining questions.

List of publications

1. Refereed journal publications

A. Champion and Y. Bellouard, "Direct volume variation measurements in fused silica specimens exposed to femtosecond laser," Opt. Mater. Express **2**, 789-798 (2012).

Y. Bellouard, A. Champion, B. Lenssen, M. Matteucci, A. Schaap, M. Beresna, C. Corbari, M. Gecevicius, P. Kazansky, O. Chappuis, M. Kral, R. Clavel, F. Barrot, J.-M. Breguet, Y. Mabillard, S. Bottinelli, M. Hopper, C. Hoenninger, E. Mottay, and J. Lopez, "The Femtoprint Project (Invited)," JLMN **7**, 1–10 (2012).

A. Champion, M. Beresna, P. Kazansky, and Y. Bellouard, "Stress distribution around femtosecond laser affected zones: effect of nanogratings orientation," Opt. Express **21**, 24942–24951 (2013).

C. Corbari, A. Champion, M. Gecevinius, M. Beresna, Y. Bellouard, and P. G. Kazansky, "Femtosecond versus picosecond laser machining of nano-gratings and micro-channels in silica glass," Opt. Express **21**, 3946–3958 (2013).

Y. van de Burgt, A. Champion, and Y. Bellouard, "In-situ localized carbon nanotube growth inside partially sealed enclosures," AIP Advances **3**, 092119 (2013).

2. Conference publications

A. Champion, Y. Bellouard, G. Mindaugas, M. Beresna, and P. G. Kazansky, "Role of stress in the chemical etching of fused silica exposed to low-energy femtosecond laser pulses," Proc. SPIE 7925 Photonic West, Frontiers in Ultrafast Optics: Biomedical, Scientific, and Industrial Applications XI, 79250Z (2011); doi:10.1117/12.886307, San Fransisco, (Oral presentation).

A. Champion, Y. Bellouard, "Analysis of stress generated inside nanogratings," International Symposium on Optomechatronics Technologies 2011, Symposium on Ultra fast Laser Modifications of Materials, Hong Kong (poster).

A. Champion, M. Beresna, P. G. Kazansky, and Y. Bellouard, "Nanograting Orientation Influence on Stress Induced by Femtosecond Laser in Fused Silica," MATEC Web of Conferences **8**, 04008 (2013). Cargèse, Corsica (poster).

110

A. Champion, Y. Bellouard, "Density variation in fused silica exposed to femtosecond laser," Proc. SPIE. 8247, Photonic West, Frontiers in Ultrafast Optics: Biomedical, Scientific, and Industrial Applications XII, 82470R (2012). doi: 10.1117/12.907007, San Fransisco, (Oral presentation).

A. Champion, Y. Bellouard, P. Kazansky, and M. Beresna, "Nanograting Orientation Influence on Stress Induced by Femtosecond Laser in Fused Silica," in CLEO: 2013, OSA Technical Digest (online) (Optical Society of America, 2013), p. CF2G.2. San Jose, (Oral presentation).

A. Champion, B. W. McMillen, and Y. Bellouard, "Evidence of stress-state inversion induced by non-ablative femtosecond laser pulses in fused silica," OSA, in Advanced Photonics, BGPP conference, Spain 2014 (poster).

Societal summary

Microsystems are ubiquitous in our daily life. Smart phones, cars, computers, but also innovative medical devices are just a few examples among many products and devices that have benefited from the progress made in miniaturizing devices and from microsystems in general. Femtosecond laser machining is a powerful microfabrication approach that can be used for 3D micro-fabrication of microsystems in transparent materials. It is a direct writing method that could efficiently replace common micro-fabrication techniques such as lithography, which requires larger infrastructure and complex experimental processes. By focusing the laser beam in the sample, we can locally change the properties of glass. In combining the laser exposure with a subsequent etching process using an acid, the parts exposed to the laser are dissolved so that a microstructure is formed. The goal of the Femtoprint project, of which the work reported in this thesis was part, was to build a printer, based on femtosecond laser machining, to perform micromachining in transparent materials. Using this process, it is possible to create various microsystems with feature sizes down to the nano-scale. In our group, this has been demonstrated with components such as algae biochips, transparent actuators, novel polarization converters to create optical vortices, accurate 3-D moulds for soft polymer shaping, and the demonstration of 5D optical memory. These components cannot be made monolithically with other fabrication techniques such as lithography since these are 2D processes. The Femtoprint project aims to provide his printer to numerous users from industry, research labs and universities who will be able to produce their own micro-systems quickly and without the need for expensive infrastructures and specific expertise. The potential economical impact and therefore the impact on the society is large and varied.

The main objective of this thesis was to study and understand fundamental aspects of the femtosecond laser micromachining process, which would enable a more efficient and optimal use of the method. The particular focus was on the relation between laser exposure parameters, the induced volume change and structure modifications, and the etching rate. The obtained insight makes it possible to optimize the etching process and volume variations according to the laser parameters and therefore to optimize the micromachining process in transparent materials. Indeed the control of the etching rate allows fabricating accurate shapes in glass, and the control of the volume variation allows optical and mechanical component fabrication. Furthermore accurate positioning of components, integrated in the systems, can be achieved creating displacements in glass induced by volume variations). On conclusion, this thesis contributes to the further development of micromachining by femtosecond laser processing in transparent materials, which finds its way more and more involved in micro-

fabrication since it is not only very precise and versatile, but also the cost of femtosecond lasers is decreasing while their power increases.

Samenvatting

De toepassing van een innovatieve micro-fabricage methode voor de fabricage van drie dimensionale micro-onderdelen in kwartsglas wordt in dit werk besproken. De methode maakt gebruik van femtoseconde laser pulsen gevolgd door een ets stap, welke respectivelijk lokaal materiaal non ablatief modificeren en verwijderen. Dit proces wordt gebruikt in een toenemend aantal applicaties, variërend van optomechanica tot optofluidica.

Tot op heden zijn de parameters die gebruikt worden in het proces met name gebaseerd op een trial-and-error aanpak. Dit zorgt ervoor dat het micro-fabricage proces niet efficiënt en optimaal wordt gebruikt, vanwege het gebrek aan het begrip van de relatie tussen de laser belichting-parameters en lokale ets mechanismen. Noemenswaardig hierbij is dat de invloed van spanningen buiten beschouwing wordt gelaten.

Dit poefschrift poogt de keuze van procesparameters te verduidelijken door het specifiek onderzoeken van lokale dichtheidsveranderingen die optreden ten gevolge van laser modificatie. Deze zijn essentieel voor het correleren van de in het materiaal geïnduceerde spanning met laser-geïntroduceerde nanostructuren, als ook voor het verkrijgen van meer inzicht in het anisotrope gedrag van lokaal laser gemodificeerde gebieden.

Twee karakterisatie methoden worden gebruikt; de ene is gebaseerd op het meten van de vervormingen van balk-structuren; de andere is gebaseerd op het karakteriseren van spanning-geïntroduceerde dubbelbrekendheid van het materiaal ten gevolge van laser modificatie. De meetmethoden geven inzicht in volume veranderingen, de grootte van de spanning rondom het lokaal gemodificeerde materiaal en de invloed van de polarisatie van het laser licht.

Daarnaast wordt de specifieke invloed van spanning op het etsgedrag van het materiaal onderzocht, waarbij rekening wordt gehouden met het feit dat mogelijke fotochemische effecten door laser modificatie niet mogen worden meegenomen. Dit wordt gerealiseerd middels een femtoseconde laser gefabriceerd micro-mechanisme in kwartsglas dat nauwkeurig onder hoge, homogene en goed gedefinieerde spanning kan worden gezet. Middels het observeren van de lokale etssnelheid-toename in onder spanning geplaatste gebieden, kan het verband tussen spanning en etssnelheid gevonden worden welke onafhankelijk is van de gebruikte laser parameters.

Gebruik makende van de bovenstaande drie technieken zijn we in staat om: allereerst, de transitie tussen lokale dichtheidstoename en volume expansie te onderzoeken als functie van laser-parameters; ten tweede, de invloed van de

spanning op het ets-proces te begrijpen; en tot slot, te demonstreren en kwantificeren wat de invloed is van de polarisatie van het licht.

Vanuit een theoretisch standpunt, stellen de uitkomsten van deze experimenten ons in staat een mechanisme te introduceren dat verklaart waarom de etssnelheid toeneemt en waarom of hoe de lokale effecten hieraan bijdragen en afhangen van de gebruikte laser parameters.

Vanuit een standpunt van technologie-ontwikkeling, geven de resultaten van dit proefschrift een basis voor de optimalisatie van de femtoseconde laser microfabricage procedure in kwartsglas. De resultaten geven inzicht in de optimale benodigde energie depositie voor de fabricage van micro-patronen met gewenste precisie en aspectverhouding. Daarnaast geeft het werk richtlijnen waarmee scheurvorming in geïntegreerde optische componenten kunnen worden voorkomen.

Acknowledgements

During the four years of my PhD, I met and worked with interesting and helpful people, with whom I could not have succeeded. I would like to take this opportunity to thank all of them.

First, I would like to express my heartfelt gratitude to Yves Bellouard, who was my daily supervisor. Thank you for giving me the opportunity to start a PhD in your group and for your encouragement and your patience during the entire PhD. You were always there to support and orient my work and give impressive ideas and useful advices. I learnt a lot in working with you and I really appreciate you. Futhermore, thanks to you, I attended very interesting conferences in various places around the world where I met great persons. I was involved in the Femtoprint project which gave me further opportunities to travel and work with people from seven differents entities. I would like to thank you particularly for your help and time you spent when I wrote the thesis as it was the most difficult part for me.

Second, I would like to express my sincere appreciation to Marc van Maris, Paulin Schmit, Jo Laven and Marco Hendrix who spent time to train and advise me for the use of laboratory equipements.

Thank you Marc for your help in using the SEM microscope as well as for the Sensofar which were both crucial equipments for the results presented in this dissertation. I would like to thank you for your advices and for granting me the permission to use polishing machines and the polariscope.

I would like to thank Pauline who gave me access to the sputter-coater and who showed me how to use it.

Thank you Jo and Marco for spending the time to explain and show me how to use the Raman spectroscope who was also a very important tool for the results in the PhD work.

I would like to thank my entire thesis committee for attending my defence and for providing useful comments to the dissertation. I would like to express my sincere appreciation to the external committee members, namely Peter Kazansky from Univ. of Southampton in the UK, Javier Solis, from CSIC in Spain, and Davide Iannuzzi from the Vrij Universiteit in Amsterdam, who accepted to travel, sometimes far, in order to attend my PhD defence. I would like to thank the entire Microsystems' group (Yuri, Stijn, Allison, Chuan, Tao, Christos, Ben, Nathaniel, Hossein, Giuseppe, Tamour, Allwyn, Erik, Regina, Dirk, David and Victor) and all others that I worked with. I would like to thank in particular, the group for the nice ambience, interesting discussions and advices that I received.

Finally, I would like to thank all friends and family who supported me during the four years of the PhD.

Audrey Champion.

Curriculum vitae

Audrey Champion was born in Dijon in France on February 1984. After finishing her high school, she received a higher national diploma in Optics/Photonics at Lycée Jean-Mermoz in Saint Louis (France) in 2005. In 2009, she received a Master's degree in Telecommunication Engineering from Telecom Saint-Etienne at University Jean Monet (France).

In 2010, she started a PhD in Micro- and Nano-scale Engineering under the supervision of dr. Yves Bellouard in the group of prof. Andreas Dietzel, which became the Microsystem group in 2013, headed by prof. Jaap den Toonder. The PhD project was on micromachining optimization in transparent material. This project was financially supported by the European Commission through the Seventh Framework program through "The femtoprint project" (NMP, Factories of the Future).

118